



HAL
open science

Numerical simulation and experimental investigations of two-phase flow in singularities

Chengsi Zhou

► **To cite this version:**

Chengsi Zhou. Numerical simulation and experimental investigations of two-phase flow in singularities. Fluids mechanics [physics.class-ph]. INSA de Lyon, 2017. English. NNT: . tel-02136718

HAL Id: tel-02136718

<https://hal.science/tel-02136718>

Submitted on 22 May 2019

HAL is a multi-disciplinary open access archive for the deposit and dissemination of scientific research documents, whether they are published or not. The documents may come from teaching and research institutions in France or abroad, or from public or private research centers.

L'archive ouverte pluridisciplinaire **HAL**, est destinée au dépôt et à la diffusion de documents scientifiques de niveau recherche, publiés ou non, émanant des établissements d'enseignement et de recherche français ou étrangers, des laboratoires publics ou privés.



N°d'ordre NNT : 2017LYSEI065

THESE de DOCTORAT DE L'UNIVERSITE DE LYON

opérée au sein de

L'institut national de sciences appliquées de Lyon

Ecole Doctorale N° EDA162

Mécanique, Energétique, Génie Civil, Acoustique

Spécialité/ discipline de doctorat :

Thermique et Energétique

Soutenue publiquement le 12/07/2017, par :

Chengsi Zhou

Numerical simulation and experimental investigations of two-phase flow in singularities

Devant le jury composé de :

JOSSERAND, Christophe	Directeur de Recherche	Ecole Polytechnique	Président
MAURO, William Associate	Professor	University of Naples Federico II	Rapporteur
ROIG, Véronique	Professeur des Universités	IMFT	Rapporteur
NASO, Aurore	Chargé de Recherche	École Centrale de Lyon	Examineur
REVELLIN, Rémi	Professeur des Universités	INSA-LYON	Directeur de thèse
KNIKKER, Ronnie	Maître de conférences	INSA-LYON	Co Directeur de thèse

Département FEDORA – INSA Lyon - Ecoles Doctorales – Quinquennal 2016-2020

SIGLE	ECOLE DOCTORALE	NOM ET COORDONNEES DU RESPONSABLE
CHIMIE	<p>CHIMIE DE LYON http://www.edchimie-lyon.fr</p> <p>Sec : Renée EL MELHEM Bat Blaise Pascal 3^e etage secretariat@edchimie-lyon.fr Insa : R. GOURDON</p>	<p>M. Stéphane DANIELE Institut de Recherches sur la Catalyse et l'Environnement de Lyon IRCELYON-UMR 5256 Equipe CDFA 2 avenue Albert Einstein 69626 Villeurbanne cedex directeur@edchimie-lyon.fr</p>
E.E.A.	<p>ELECTRONIQUE, ELECTROTECHNIQUE, AUTOMATIQUE http://edeea.ec-lyon.fr</p> <p>Sec : M.C. HAVGOUDOUKIAN Ecole-Doctorale.eea@ec-lyon.fr</p>	<p>M. Gérard SCORLETTI Ecole Centrale de Lyon 36 avenue Guy de Collongue 69134 ECULLY Tél : 04.72.18 60.97 Fax : 04 78 43 37 17 Gerard.scorletti@ec-lyon.fr</p>
E2M2	<p>EVOLUTION, ECOSYSTEME, MICROBIOLOGIE, MODELISATION http://e2m2.universite-lyon.fr</p> <p>Sec : Sylvie ROBERJOT Bât Atrium - UCB Lyon 1 04.72.44.83.62 Insa : H. CHARLES secretariat.e2m2@univ-lyon1.fr</p>	<p>M. Fabrice CORDEVY CNRS UMR 5276 Lab. de géologie de Lyon Université Claude Bernard Lyon 1 Bât Géode 2 rue Raphaël Dubois 69622 VILLEURBANNE Cédex Tél : 06.07.53.89.13 cordev@univ-lyon1.fr</p>
EDISS	<p>INTERDISCIPLINAIRE SCIENCES- SANTE http://www.ediss-lyon.fr</p> <p>Sec : Sylvie ROBERJOT Bât Atrium - UCB Lyon 1 04.72.44.83.62 Insa : M. LAGARDE secretariat.ediss@univ-lyon1.fr</p>	<p>Mme Emmanuelle CANET-SOULAS INSERM U1060, CarMeN lab, Univ. Lyon 1 Bâtiment IMBL 11 avenue Jean Capelle INSA de Lyon 696621 Villeurbanne Tél : 04.72.68.49.09 Fax :04 72 68 49 16 Emmanuelle.canet@univ-lyon1.fr</p>
INFOMATHS	<p>INFORMATIQUE ET MATHEMATIQUES http://infomaths.univ-lyon1.fr</p> <p>Sec :Renée EL MELHEM Bat Blaise Pascal, 3^e étage Tél : 04.72. 43. 80. 46 Fax : 04.72.43.16.87 infomaths@univ-lyon1.fr</p>	<p>M. Luca ZAMBONI Bâtiment Braconnier 43 Boulevard du 11 novembre 1918 69622 VILLEURBANNE Cedex Tél :04 26 23 45 52 zamboni@maths.univ-lyon1.fr</p>
Matériaux	<p>MATERIAUX DE LYON http://ed34.universite-lyon.fr</p> <p>Sec : Marion COMBE Tél:04-72-43-71-70 –Fax : 87.12 Bat. Direction ed.materiaux@insa-lyon.fr</p>	<p>M. Jean-Yves BUFFIERE INSA de Lyon MATEIS Bâtiment Saint Exupéry 7 avenue Jean Capelle 69621 VILLEURBANNE Cedex Tél : 04.72.43 71.70 Fax 04 72 43 85 28 Ed.materiaux@insa-lyon.fr</p>
MEGA	<p>MECANIQUE,ENERGETIQUE,GENIE CIVIL,ACOUSTIQUE http://mega.universite-lyon.fr</p> <p>Sec : Marion COMBE Tél:04-72-43-71-70 –Fax : 87.12 Bat. Direction mega@insa-lyon.fr</p>	<p>M. Philippe BOISSE INSA de Lyon Laboratoire LAMCOS Bâtiment Jacquard 25 bis avenue Jean Capelle 69621 VILLEURBANNE Cedex Tél : 04.72 .43.71.70 Fax : 04 72 43 72 37 Philippe.boisse@insa-lyon.fr</p>
ScSo	<p>ScSo* http://recherche.univ-lyon2.fr/scso/ Sec : Viviane POLSINELLI Brigitte DUBOIS Insa : J.Y. TOUSSAINT Tél : 04 78 69 72 76 viviane.polsinelli@univ-lyon2.fr</p>	<p>M. Christian MONTES Université Lyon 2 86 rue Pasteur 69365 LYON Cedex 07 Christian.montes@univ-lyon2.fr</p>

*ScSo : Histoire, Géographie, Aménagement, Urbanisme, Archéologie, Science politique, Sociologie, Anthropologie

THÈSE

**Numerical simulation and experimental
investigations of two-phase flow in
singularities**

présentée devant

L'INSTITUT NATIONAL DE SCIENCES APPLIQUÉES DE LYON

pour obtenir le grade le

Docteur

École Doctorale MEGA

(Mécanique, Énergétique, Génie Civil, Acoustique)

Spécialité : THERMIQUE ET ÉNERGÉTIQUE

par

Chengsi Zhou

Acknowledgements

This study has been carried out at the Centre d'Énergie et de Thermique de Lyon (CETHIL UMR-5008), National Institute of Applied Sciences (INSA de Lyon), under the direction of Prof. Rémi Revellin and Ronnie Knikker. This PhD Thesis has been supported by the China Scholarship Council (CSC), which are gratefully acknowledged.

I would like to thank Prof. Rémi Revellin and Ronnie Knikker for giving me the opportunity and encouragement to undertake this work. They are always patient and helpful in every occasion that I need their help. Their insightful suggestions were the key factors that always help me on the right track in my study and research. I am very lucky and happy that I worked with them for more than 3 years.

I thank Prof. Josseland Christophe of Ecole Polytechnique, Prof Mauro William of Federico II University of Naples, Prof. Roig Véronique of IMFT and Prof. Naso Aurore of Ecole Centrale de Lyon for being the examiners of this thesis.

I would like to thank other professors in our lab. Their wisdom suggestions help me a lot in the academia. Special thanks to my colleagues for their help and friendship. I also acknowledge our technicians Nicolas, Antoine and Christophe who help construct the experimental test bench.

Last, thanks to my family for their support. Even though they are not by my side, I can feel the spiritual encouragement.

Numerical simulation and experimental investigations of two-phase flow in singularities

Abstract

Numerical simulations and experimental investigations of a rising individual Taylor bubble through a vertical sudden expansion and contraction in stagnant Newtonian liquid are presented. The CFD procedure is based on the open source package Gerris which adopts the volume-of-fluid (VOF) method to represent the gas/liquid interface. The numerical method is verified using the existing results of single Taylor bubbles rising in straight columns. The experiments investigate a nitrogen bubble rising in a water-glycerol mixture for different concentrations. The pipe diameter ratio ranges from 0.69 to 1.72. The images of the bubble rising through the singularities are captured by a high-speed camera. Our investigations focus on the transient process of the bubbles passing the singularity. The variations of the bubble velocity and the liquid film thickness are investigated. The results show that the greater expansion ratios yield more perturbations on the bubbles and have strong effects on the tail of the bubble. The unstable bubble tails are cut off into smaller bubbles in some of the test cases and a bubble break-up regime map obtained by simulations has been proposed. The bubble shape variations depend also on the length of the bubbles. For a bubble passing through a contraction, the blocking phenomenon has been observed and a map has been proposed. Finally, this study, based on a large range of Eötvös numbers and expansion/contraction ratios, provides new insights to better understand the effect of singularities on rising Taylor bubbles.

Key words: Two-phase flow, Taylor bubble, contraction, expansion, VOF, experiment

Etudes expérimentales et numérique du écoulement diphasique en singularités

Résumé

Une étude numérique et des investigations expérimentales sont menées sur une bulle de Taylor ascendante au passage d'une contraction ou d'un élargissement brusque dans un liquide Newtonien stagnant. Le code CFD est issu du logiciel libre Gerris utilisant la méthode VOF (Volume Of Fluid) pour représenter l'interface liquide-gaz. La méthode numérique est vérifiée en utilisant les résultats existants sur des bulles de Taylor ascendantes dans des colonnes droites. L'étude expérimentale permet d'étudier une bulle d'azote dans un mélange eau-glycérol pour différentes concentrations. Le rapport des diamètres de la conduite varie de 0,69 à 1,72. Les images de la bulle montante dans les singularités sont capturées par une caméra haute vitesse. Les variations de vitesse de la bulle et de l'épaisseur du film liquide sont étudiées. Les résultats montrent que l'élargissement brusque avec un rapport de diamètres plus élevé entraîne plus de perturbations sur la bulle avec de forts effets sur sa queue. Les queues de bulles instables sont coupées en petites bulles dans certains cas et une carte d'écoulement permet de le prédire. En outre, il a été observé que les variations de la forme de la bulle dépendent de la longueur des bulles. En ce qui concerne la bulle passant par une contraction, le phénomène de blocage a été observé et une carte de prédiction a été proposée. Finalement, cette étude, basée sur un intervalle assez large du nombre d'Eötvös et du rapport de diamètres, propose de nouvelles connaissances pour mieux comprendre l'ascension d'une bulle de Taylor dans les singularités.

Mots clés: écoulement diphasique, bulle de Taylor, contraction, élargissement, VOF, expérience

Contents

Acknowledgements	iii
Abstract	v
1 Introduction	1
1.1 Background	1
1.2 Objectives of the study	1
1.3 Methodology	2
1.4 Layout of the thesis	2
2 Taylor bubble: a state of the art review	5
2.1 Bubble dynamics	5
2.2 Numerical simulation of two-phase flows	8
2.2.1 Two-phase flow equations	8
2.2.2 Interface tracking and capturing methods	9
Level-Set method	9
Front tracking method	11
Volume of fluid method	12
2.3 Bubble motion in channels	15
2.3.1 Rising bubbles in vertical channels	16
Terminal velocity	18
Falling film	21
Bubble nose	23
Numerical simulations	24
Experimental studies	25
2.4 Bubble motion through expansions and contractions	26
2.4.1 Expansions	26
2.4.2 Contractions	27
2.4.3 Applications	28
Photobioreactors	28
Volcanology	28
2.5 Chapter conclusion	29
3 Numerical model and validations	33
3.1 Introduction of the numerical solver	33
3.1.1 Governing equations	33

3.1.2	Numerical method for solving the incompressible Navier-Stokes equations	34
	Basics of the projection method	34
	Projection method in the present study	35
	Adaptive Mesh Refinement	35
	Volume-of-Fluid (VOF)	37
	Surface tension calculation	37
	Height function	38
	Parallelization	38
3.2	Basic test cases	39
3.2.1	Error quantification	39
3.2.2	Lid-driven cavity	39
3.2.3	Bubble rising in stagnant liquid	40
	Benchmark test cases	40
	Results of the test case 1	43
	Results of the test case 2	43
	Adaptive mesh tests	45
	Tests in Cylindrical coordinates	46
	3D tests	51
3.2.4	Parallelisation tests	51
3.3	Chapter conclusion	52
4	Description of the experiments	55
4.1	Description of the experimental test facility	55
4.1.1	Bubble generator chamber	55
4.1.2	Visualization section	57
4.2	Experimental procedure	58
4.3	Measurements and data acquisition	59
4.3.1	Uncertainty calculation	59
4.3.2	Tube diameter	60
4.3.3	Temperature	60
4.3.4	Water-glycerol solutions	60
4.3.5	Viscosity measurement	61
4.3.6	Density measurement	61
4.3.7	Fluid properties	61
4.3.8	Image processing	62
4.3.9	Optical correction	63
4.3.10	Calculation of the bubble volume	65
4.3.11	Calculation of the bubble velocity	66
4.4	Summary of experimental data range	67
4.5	Chapter conclusion	68

5	Bubble rising in straight tube	69
5.1	Model description	69
5.2	Sensitivity analysis	70
5.2.1	Mesh independency analysis	70
5.2.2	Effects of initial bubble lengths	71
5.2.3	Effects of density ratios	72
5.2.4	Effects of viscosity ratios	74
5.2.5	Effects of Eo number	74
5.2.6	Summary	75
5.3	Comparison with experiments	76
5.3.1	Shape comparison	76
5.3.2	Terminal velocity comparison	77
5.3.3	Liquid film comparison	77
5.3.4	Velocity field comparison	85
5.4	Chapter conclusion	86
6	Bubble rising through the expansion	89
6.1	Model description	89
6.1.1	Simulations	89
6.1.2	Experiments	89
6.1.3	Illustration of the bubble features	90
6.2	Results	91
6.2.1	Bubble without break-up in the expansion	91
	Comparison of experiments and simulations	91
	Velocity variation	94
	Bubble length variation	97
	Transition time of the bubble in the expansion	98
	Necking	100
6.2.2	Bubble with break-up in the expansion	100
	Break-up patterns	100
	Break-up pattern map	102
6.3	Chapter conclusion	103
7	Bubble rising through contractions	105
7.1	Model description	105
7.1.1	Simulations	105
7.1.2	Experiments	105
7.2	Result analysis	106
7.2.1	Comparison of experiments and simulations	106
7.2.2	Velocity variation	108
7.2.3	Bubble length variation	111
7.2.4	Transition time of the bubble in the contraction	111
7.2.5	Bubble blocking	112

7.3 Chapter conclusion	114
8 Conclusions and perspectives	117
8.1 Synthesis	117
8.2 Concluding remarks	118
8.3 Perspectives	118
A Comparison of the bubble rising test cases	121
A.1 Results	121
A.2 Comparison	123
B Nomenclature	125
Bibliography	127

List of Figures

2.1	Shape regime map for bubbles in liquids. (Replot based on [18]).	7
2.2	Iso-level curves from a level-set formulation. The circular bubble initialized at $(x = 0.5, y = 0.5)$ with 1.0 radius.	10
2.3	An example of the front of Front-tracking method and its background grid. [109]	12
2.4	Calculating volume fraction column-wise and row-wise to estimate the line slope.	15
2.5	Flow pattern map for Taylor bubble rising in stagnant liquid. (Replot based on White and Beardmore [118]).	18
2.6	Bubble column and air lift bioreactors. (Replot based on [96]).	29
2.7	Diagram of the Taylor bubble in a lava conduit and its rising towards the lava lake. (Replot based on [21]).	30
3.1	Example of quadtree mesh (left) and the corresponding tree-structure representation (right). [83]	36
3.2	Geometrical flux computation on a quadtree mesh. [82]	37
3.3	Boundary conditions of the lid-driven cavity problem.	40
3.4	Velocity (u and v) comparison with the results in [43]. (a) $Re=100$, (b) $Re=1000$.	41
3.5	Convergence rates of (a) u -velocity and (b) v -velocity along the center of cavity.	41
3.6	Pressure field along the center of cavity and its convergence rate.	42
3.7	Initial configuration and boundary conditions for the test cases.	42
3.8	Time evolution of the interface for test case 1 on the finest grid.	44
3.9	Test case 1 bubble shapes at $t = 3$. The shapes are computed on different grid resolutions.	45
3.10	Time evolution of the interface for test case 2 on the finest grid.	46
3.11	Test case 2 bubble shapes at time=3. The shapes are computed on different grid resolutions.	47
3.12	Center of mass for test case 1 (A) and 2 (B).	47
3.13	Circularity for test case 1 (A) and 2 (B).	48
3.14	Rise velocity for test 1 (A) and 2 (B).	48
3.15	Adaptive mesh and interface of the bubble at $t = 3$ for test case 1. (A) The finest level of mesh equals to $1/32$. (B) Finest level of mesh equals to $1/256$	49
3.16	Relative errors of adaptive mesh with their corresponding results in uniform mesh for test case 1. (A) Relative error of the center of mass. (B) Relative error of the velocity.	49
3.17	CPU times consume in uniform mesh and adaptive mesh for test case 2	50

3.18	Sensitive analysis on the calculation domain width. ($Re = 35, Bo = 125$) (A) Bubble velocity. (B) Bubble shape at $t = 5$.	50
3.19	Bubble shape evolution with the time. ($Re = 200, Bo = 200$)	51
3.20	Real time spent with different number of CPU cores.	52
3.21	The maximum, minimum and average number elements on different CPU cores. Total number of the CPU cores is 16. Finest meshes are (A) $h = 1/64$, (B) $h = 1 / 512$.	53
4.1	Configuration of the experimental test bench.	56
4.2	Illustration of the bubble generator chamber.	56
4.3	Illustration of the visualization section.	57
4.4	Sketch of the connection plate.	58
4.5	(A) Shear rate vs. shear stress of different water-glycerol solutions. (B) Measured viscosity of the water-glycerol solution as a function of the measured volume percentage of glycerol.	61
4.6	(A) Detecting the tube. (B) Rotating the image. (C) Removing the noises on the image. (D) Select the main bubble.	63
4.7	Illustration of the light refraction across tube wall.	64
4.8	The optical correction along the radius.	65
4.9	(A) The points indicate the surface. (B) Rearrangement and connection of the points.	66
4.10	(A) The two halves of the bubble. (B) The results of the bubble volume in each frame.	67
5.1	Initial configuration for the simulation.	70
5.2	(A) Bubble tail shapes for different meshes. (B) Velocity profile in different meshes.	71
5.3	Tail velocities with different initial bubble lengths.	72
5.4	(A) Effect of density ratios on bubble tail shapes. (B) Effect of density ratios on the bubble terminal velocities.	73
5.5	(A) Effect of density ratios on bubble nose velocities. (B) Effect of density ratios on bubble tail velocities.	73
5.6	(A) Effect of viscosity ratios on bubble tail shapes. (B) Effect of viscosity ratios on the bubble terminal velocities.	74
5.7	(A) Effect of viscosity ratios on bubble tail shapes. (B) Effect of viscosity ratios on the bubble terminal velocities.	75
5.8	Comparison of the bubble shape. (W-G 95%, $Eo = 49.7, \log(Mo) = 0.37$)	80
5.9	Comparison of the bubble shape. (W-G 90%, $Eo = 49.1, \log(Mo) = -0.68$)	80
5.10	Comparison of the bubble shape. (W-G 80%, $Eo = 47.6, \log(Mo) = -2.62$)	81
5.11	Comparison of the bubble shape. (W-G 70%, $Eo = 41.9, \log(Mo) = -3.65$)	81
5.12	Comparison of the bubble shape. ((W-G 60%, $Eo = 40.55, \log(Mo) = -4.63$)	82
5.13	Comparison of the bubble nose and tail shape.	82

5.14	Numerical results (filled symbols) of the Froude number plotted as a function of the Eötvös number and for different values of the Morton number. The dashed and solid lines correspond to the correlations of Wallis [116], Hayashi, Kurimoto, and Tomiyama [44], and Viana et al. [115]. Experimental data (open symbols) from White and Beardmore [118] are also added for comparison. . . .	83
5.15	Comparison of the terminal velocity. (A) Experiments vs. correlations (B) Experiments vs. simulation.	83
5.16	Comparison of film thickness for different D_s/D and water-glycerol solutions.	84
5.17	Numerical velocity fields and streamlines for a case with $Mo = 4.31 \times 10^{-2}$ and $N_f = 111$	85
5.18	Comparison of numerical dimensionless velocity profiles (u_z/U^*) at bubble head with numerical and experimental results from [10].	86
5.19	Comparison of numerical dimensionless velocity profiles (u_z/U^*) at bubble tail with numerical and experimental results from [10].	86
6.1	Initial configuration for the simulation.	90
6.2	Illustration of the bubble features described in this study.	91
6.3	Experimental and numerical results of the bubble rising through the expansion. (W-G 95%, $Eo = 49.7$, $\log(Mo) = 0.37$, $\epsilon = 1.24$)	92
6.4	Experimental and numerical results of the bubble rising through the expansion. (W-G 90%, $Eo = 49.2$, $\log(Mo) = -0.68$, $\epsilon = 1.24$)	92
6.5	Experimental and numerical results of the bubble rising through the expansion. (W-G 80%, $Eo = 47.5$, $\log(Mo) = -2.62$, $\epsilon = 1.24$)	93
6.6	Experimental and numerical results of the bubble rising through the expansion. (W-G 70%, $Eo = 41.9$, $\log(Mo) = -3.65$, $\epsilon = 1.24$)	93
6.7	Experimental and numerical results of the bubble rising through the expansion. (W-G 60%, $Eo = 40.6$, $\log(Mo) = -4.63$, $\epsilon = 1.24$)	94
6.8	Numerical results of steady state of bubble ($U = V_T$) before and after the expansion (symbols) and the correlations of Wallis [116] and Viana et al. [115] (line). ($Mo = 1 \times 10^{-2}$)	95
6.9	Evolution of the dimensionless bubble velocity as a function of the bubble head position at four locations of the bubble. The vertical dashed lines mark the location of the bubble entering and leaving the expansion. The horizontal dashed line indicates the bubble terminal velocity before entering the expansion. ($Mo=1 \times 10^{-2}$, $Eo=100$, expansion ratio=1.2)	96
6.10	Evolution of the mass center velocity for different values of the initial bubble length. The dashed lines mark the locations of the bubble entering and leaving the expansion. ($Mo = 1 \times 10^{-2}$, $Eo = 100$, $\epsilon = 1.1$)	97
6.11	Maximum value of the bubble mass center velocity as a function of the Eo number for different expansion ratios ($Mo=1 \times 10^{-2}$).	98

6.12	Evolution of the bubble length for different expansion ratios as a function of the bubble head position. The dash lines mark the locations of the bubble entering and leaving the expansion. ($Mo = 1 \times 10^{-2}$, $Eo = 100$)	99
6.13	Illustration of the transition time of the bubble in the expansion.	100
6.14	Time shift of the bubble in different expansion ratios. ($Mo=1 \times 10^{-2}$)	101
6.15	Evolution of the bubble neck radius for different expansion ratios as a function of the bubble head position. The snapshots show the bubble shape when it reaches the minimum bubble neck radius. ($Mo=1 \times 10^{-2}$, $Eo=100$)	101
6.16	Bubble break-up in the expansion (W-G 95%, $\epsilon = 1.72$)	102
6.17	Bubble break-up in the expansion (W-G 80%, $\epsilon = 1.72$)	102
6.18	Bubble break-up in the expansion (W-G 70%, $\epsilon = 1.72$)	103
6.19	Bubble break-up regime map obtained by simulations.	104
7.1	Initial configuration for the simulation.	106
7.2	Experimental and numerical results of the bubble rising through a contraction (W-G 70%, $Eo = 41.9$, $\log(Mo) = -3.65$, $\epsilon = 0.93$)	107
7.3	Experimental and numerical results of the bubble rising through a contraction (W-G 70%, $Eo = 41.9$, $\log(Mo) = -3.65$, $\epsilon = 0.81$)	107
7.4	Experimental and numerical results of the bubble rising through the contraction (W-G 70%, $Eo = 41.9$, $\log(Mo) = -3.65$, $\epsilon = 0.69$)	108
7.5	Experimental and numerical results of the bubble rising through the contraction (W-G 60%, $Eo = 40.6$, $\log(Mo) = -4.63$, $\epsilon = 0.81$)	109
7.6	Experimental and numerical results of the bubble rising through the contraction (W-G 80%, $Eo = 47.5$, $\log(Mo) = -2.62$, $\epsilon = 0.81$)	109
7.7	Evolution of the dimensionless bubble velocity from simulation as a function of the bubble head position at four locations of the bubble. The vertical dash lines mark the location of the bubble entering and leaving the contraction. The horizontal dash line indicates the bubble terminal velocity before entering the contraction. ($Mo = 1 \times 10^{-2}$, $Eo = 100$, contraction ratio = 0.9)	110
7.8	Evolution of the bubble head and tail velocity for different values of the initial bubble length. ($Mo = 1 \times 10^{-2}$, $Eo = 100$, contraction ratio = 0.9)	111
7.9	Evolution of the bubble length in different contraction ratio. ($Mo = 1$, $Eo = 100$)	112
7.10	(A) Illustration of the transition time of the bubble in the contraction. (B) Illustration of the bubble interface trajectory.	113
7.11	Time shift due to the effects of the contractions. ($Mo = 1 \times 10^{-2}$)	113
7.12	Bubble interface trajectory passing through the contraction. ($Mo = 1 \times 10^{-3}$, Contraction ratio = 0.7)	115
7.13	Bubble interface trajectory passing through the contraction. ($Mo = 1 \times 10^{-3}$, $Eo = 50$)	115
7.14	Bubble blocking regime map.	116
A.1	Comparison of the minimum circularity. (A) case 1. (B) case 2.	123
A.2	Comparison of the maximum rise velocity. (A) case 1. (B) case 2.	123

A.3 Comparison of the final center of mass. (A) case 1. (B) case 2. 124

List of Tables

2.1	Summary of the models for liquid film of the Taylor bubble presented in literature. [61]	22
2.2	Summary of simulations of the Taylor bubble in straight tube presented in literature.	25
2.3	Summary of the experimental studies of the Taylor bubble rising in vertical tube.	31
2.4	Summary of the experimental studies of the Taylor bubble rising in vertical tube.	32
3.1	Physical parameters of the test cases	41
3.2	Prediction of the bubble shapes	51
4.1	Camera related parameters.	58
4.2	Diameter of the upper tubes.	60
4.3	Summary of the properties of the water-glycerol solutions.	62
4.4	The refraction index of glass and glycerol solution.	65
4.5	Summary of parameters in the experiments.	67
5.1	Mesh parameters.	71
5.2	Dimensionless numbers of the Taylor bubble in the tube with $D_{in} = 16.40$ mm.	76
5.3	Film thickness data points in different water-glycerol solutions compared to correlations from literature.	79
6.1	Diameters of the tubes.	90
7.1	Diameters of the tubes.	105
A.1	Relative error norms and convergence orders for test case 1	121
A.2	Relative error norms and convergence orders for Test Case 2	122
A.3	Minimum circularity and maximum rise velocity, with corresponding incidence times and final position of the center of mass for test case 1	122
A.4	Minimum circularity and maximum rise velocity, with corresponding incidence times and final position of the center of mass for test case 2	122

Chapter 1

Introduction

1.1 Background

The Taylor bubble flow is one of the liquid-gas flow patterns consisting of elongated bubbles separated by liquid slugs. The details of the flow patterns will be discussed in Chapter 2. Taylor bubbles are encountered in research and industry, which exist from micro-fluids to a much larger scale. In industrial processes, Taylor bubbles are often found in buoyancy driven fermenters, the transportation of hydrocarbons in oil and gas industry, the boiling and condensing process in the thermal power plants. Large scale Taylor bubbles also exist in the natural world. The eruption of Strombolian volcanoes is considered to be caused by the rise and burst of large Taylor bubbles. The photobioreactor is another application of the rising bubble. More details of these two examples will be proposed in Chapter 2.

Due to its great importance, the Taylor bubble has been thoroughly investigated in past decades. But, a large volume of research investigated the rising of Taylor bubbles in straight tubes. There is little work that reports the rising of Taylor bubbles through expansions or contractions. The expansion or contractions are often called singularities, which are widely seen in the industrial applications. The design of the oil pipe line or the heat exchanger often use expansions or contractions in pipe connections. In the example of volcanoes, the bubble rises from the great depth through the lava conduit. The cross-sectional shapes changes while the bubble rises. It is not reasonable to apply the research of the Taylor bubbles rising in straight tubes in such conditions. The Taylor bubble rising through expansion and contraction should be investigated.

Therefore, the lack of understanding of the mechanisms of the Taylor bubble rising through the singularities motivates the present research. Based on the research of the Taylor bubble in straight pipes, we carried out the study on the Taylor bubble rising through singularities.

1.2 Objectives of the study

The primary objective is modeling the Taylor bubbles rising through expansions and contractions. The aim is to understand the bubble behavior in flow conditions which have not been studied yet. To achieve this, the work has been divided in the following tasks:

- Visualize the bubble behaviors in the straight pipe and through the expansions and contractions thanks to experimental investigations.

- Use CFD (Computational Fluid Dynamics) to model the single rising Taylor bubbles.
- Validated the numerical model thanks to experimental data.
- Characterize the flow disturbances caused by the expansions or contractions using the CFD model.

1.3 Methodology

An incompressible two-phase flow solver is used for establishing the model to investigate the Taylor bubble in this research work. The solver is an open source flow solver called *Gerris*.

The CFD solver will be validated before carrying out further investigation. We perform several benchmark cases to test the performance of the solver on simulating the two-phase flow. A comprehensive test on the single bubble rising is carried out.

On the other hand, the experimental methods are also used to investigate the bubble behavior. The bubble rising in different water-glycerol solutions has been recorded by a high speed camera. The bubble shape variation will be further investigated by analyzing the images. The numerical model will then be validated by the experimental data.

The investigation on the Taylor bubble rising through singularities can be done by analyzing the reliable data from the experiment and simulation.

1.4 Layout of the thesis

The thesis is divided into eight chapters with several appendices. It is organized as follows:

- *Chapter 1* provides a background to the study and the research objectives.
- *Chapter 2* gives an overview of the two-phase flow phenomena and the methods of modeling the two phase flow in particular, the single bubble rising and Taylor bubble rising in the tube.
- *Chapter 3* describes the numerical model used in the present study and the numerical benchmark tests have been performed to validate the numerical model.
- *Chapter 4* describes the experimental test facility. The experimental methodology and the data reduction procedure are also described.
- *Chapter 5* presents the experimental and simulation results of the Taylor bubble rising in a straight tube. A sensitivity analysis has been carried out to test the accuracy of the bubble in the straight tube. The simulations have been validated with our experimental data and data from the literature.
- *Chapter 6* presents the experimental and simulation results of the Taylor bubble rising through the expansions. A detailed analysis on the bubble behavior is shown. The bubble break up behaviors are also presented.

- *Chapter 7* presents the experimental and the simulation results of the Taylor bubble rising through the contractions. A detailed analysis on the bubble behavior in the contraction is shown. The bubble blocking phenomenon will be discussed.
- *Chapter 8* presents the general conclusions of this study and the perspectives.

Chapter 2

Taylor bubble: a state of the art review

In the context of multiphase flow, *two-phase flow* refers to the flow of any two fluids mixed together, whereas those fluids do not mix on the molecular level. In another word, the liquids are not miscible. An interface between two liquids can be observed from a macroscopic view. Even though we excluded some special circumstances, it still leaves a diverse spectrum of two-phase flows.

In this chapter, we first present a brief introduction about the bubble dynamics. It will introduce the basic physical mechanism of the gas bubble in the liquid and clarify the region of our study. Secondly, we will discuss the widely used numerical methods on interface capture. Various numerical models are applicable to gas-liquid two-phase flow. We will discuss most of them. Finally, we focus on the bubble dynamics. A detailed review will be presented on the Taylor bubble. Both experimental and simulation studies will be reviewed.

2.1 Bubble dynamics

Bubbles can often be observed in various industrial processes, such as boiler, steam generator in the power plant and chemical reactors. The bubble characteristics depend on the property of fluids, the quantity of each phase. Bubble dynamics investigates the formation, movement and collapse of bubbles. In this brief introduction, we mainly introduce the previous study about the bubble movement, especially the freely rising bubble in stagnant liquid.

The freely rising bubble is a fundamental problem of two-phase flow. This simple problem eliminates many effects and just focused on the liquid, gas and their interface. Therefore, the problem is a good test case for the numerical methods. The accurate prediction of the interface is crucial for aforementioned interface tracking methods. On the other hand, the bubble rising problem does physically exist. Understanding the bubble behavior has a great importance of evaluating the force acting on a bubble and mass transfer coefficient.

From a physical point of view, the bubble motion is determined by the forces acting on it, such as buoyancy, inertial, viscous and interfacial forces. The combination of these forces can be regrouped into dimensionless numbers. The studies of the freely rising bubbles focus on the bubble dynamics and eliminate other factors, such as containing the vessel. Bhaga and Weber [18] presented the results of their experiments in terms of the following dimensionless groups:

- Reynolds number:

$$\text{Re} = \frac{\rho DU}{\mu} \quad (2.1)$$

- Eötvös or Bond number:

$$\text{Eo} = \frac{gD^2\rho}{\sigma} \quad (2.2)$$

- Morton number:

$$\text{Mo} = \frac{g\mu^4}{\rho\sigma^3} \quad (2.3)$$

- Weber number:

$$\text{We} = \frac{\rho U^2 D}{\sigma} \quad (2.4)$$

where, the characteristic length, $D = (6V/\pi)^{1/3}$, is the volume-equivalent diameter of a bubble of volume V . U is the bubble terminal rise velocity, and ρ , μ and σ are the density, viscosity and surface tension of the liquid. g is the acceleration of gravity. The experimental data in [18] covers a wide range of $\text{Eo} = [8.67, 641]$ and $\text{Mo} = [8.4 \times 10^{-4}, 711]$. And, they presented a bubble shape regime map. They also classify the bubbles into 7 groups based on the shape: s, spherical; oe, oblate ellipsoid; oed, oblate ellipsoidal; oec, oblate ellipsoidal cap; scc, spherical cap with closed steady wake; sco, spherical cap with open unsteady wake; sks, skirted with smooth skirt; skw, skirted with wavy unsteady skirt. Those 7 regions are shown in Fig. 2.1.

Here, we review works have been done by numerical simulation about the bubble rising. The development of the numerical methods helps us understand the bubble motion. On the other hand, the experimental studies help to improve and validate the numerical methods.

Tomiya et al. [107] has done the pioneering work on rising bubbles by the VOF method. The simulation affirmed that the sinuous motion of the bubble is induced by the Karman vortex shedding from the tail of the bubble. The bubble trajectories agreed well with the available experimental data.

Sussman [100] adopted a coupled level set/volume-of-fluid method to compute growth and collapse of vapor bubbles. The study focused on the numerical method. They proved that the overall convergence rate of the coupled method is second order.

Ohta et al. [76] simulated 2D-axisymmetric bubble rising in viscous Newtonian liquids using the CLSVOF method and compared results with experimental data. The main objective is to verify the influence of the numerical initial conditions on the bubble rising. They found that the bubble will break up eventually if the initial bubble is spherical for $\text{Eo} = 464$ and $\text{Mo} = 6.5 \times 10^{-2}$. If the bubbles are at low Mo number, the bubble motion is not depending on the initial bubble shape.

Olsson and Kreiss [77] tested a conservative level set method on an air bubble rising in water for $\text{Re} = 500$, $\text{Fr} = 0.45$ and $\text{We} = 0.68$.

Sankaranarayanan et al. [88] computed the bubble rising in periodic boxes by the lattice Boltzmann method. Many test cases have been performed and covered the range of Morton number from 10^{-6} to 10^{-4} . The results are compared to empirical correlations.

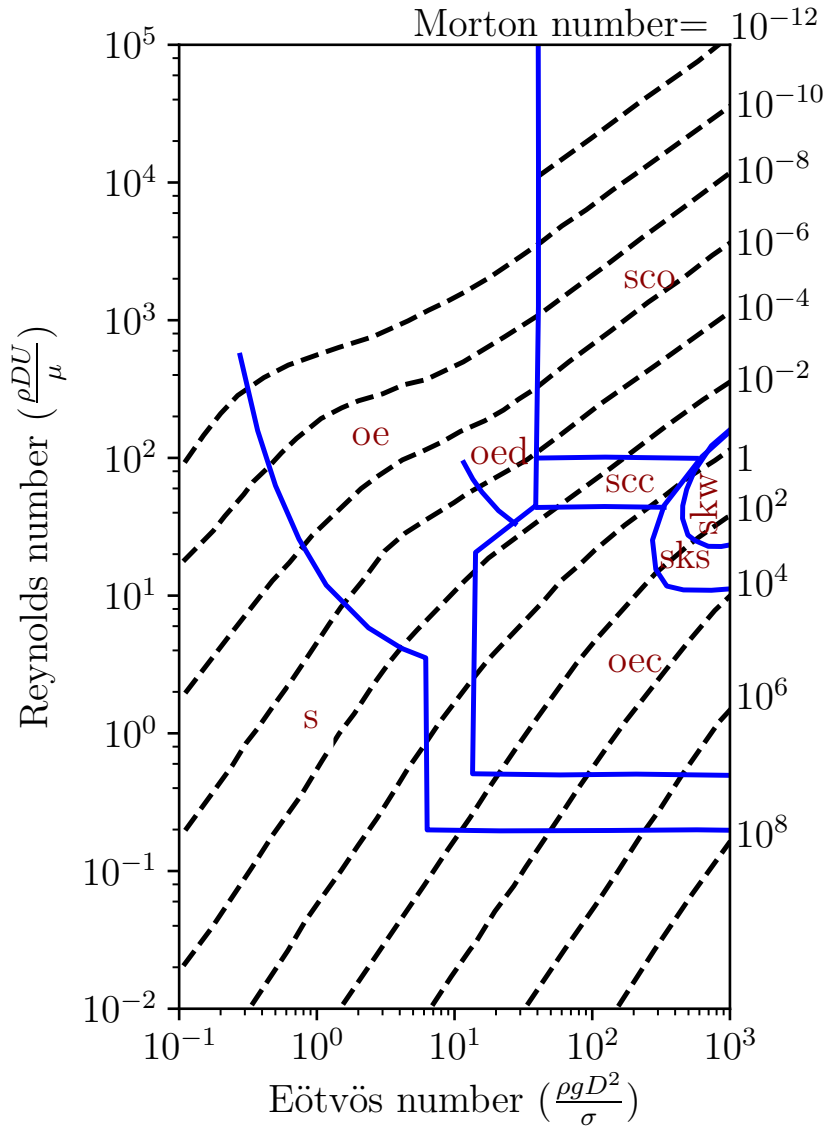


FIGURE 2.1: Shape regime map for bubbles in liquids. (Replot based on [18]).

Ohta et al. [76] showed that the bubbles with breaking-up could be numerically simulated starting from the spherical bubble. They also found that at low Mo number condition the bubble motion is not subject to the initial bubble conditions.

Wang et al. [117] investigated the viscosity effects on the bubble shape. The VOF method is adopted. Their simulations ignored the surface tension, $Eo = \infty$. They found two critical Re numbers Re_1 and Re_2 . Re_1 is in between 30 and 50. If the Re larger than Re_1 , the bubble will break into toroidal form. Re_2 is in between 10 and 20. If $Re < Re_2$, the splitting will not happen. According to Fig. 2.1, the bubble with large Re number and lower surface tension, the final shape will be spherical-cap with an unsteady wake. The bubble breakup may not be a physical truth. This conclusion agrees with Ohta et al. [76].

The study of Aoyama et al. [7] focuses on the ellipsoidal bubble. The experiment measured the bubble aspect ratio from a wide range of fluid properties. They provide a correlation to predict aspect ratio (E) as a function of Eo and Re numbers:

$$E = \frac{1}{(1 + 0.016Eo^{1.12}Re)^{0.388}} \quad (2.5)$$

This equation covers the range $-11 \leq \log(Mo) \leq 0.63$, $3.2 \times 10^{-3} \leq Re \leq 1.3 \times 10^3$ and $4.2 \times 10^{-2} \leq Eo \leq 2.9 \times 10^1$.

Other studies relate to the rising bubble. But, they include other effects or constraints. Some of them are worth mentioning. The migration of small bubbles toward the pipe wall due to the shear-induced lift force. Tomiyama et al. [108] and Rabha and Buwa [84] investigated this phenomenon by experiment and simulation. Zun et al. [124] studied the bubble rising in the stratified water layer. The purpose is to provide further insights on bubble-induced agitation of heated bulk liquid. The bubble is a 6 mm equivalent sphere diameter air bubble across a stratified thermal layer. The simulation shows that the bubble wake carries cold water in the vertical direction and causes a strong longitudinal mixing.

2.2 Numerical simulation of two-phase flows

2.2.1 Two-phase flow equations

One-Fluid Formulations are widely used for modeling of two-phase flow. Instead of solving each phase separately, only one group of governing equations is solved throughout the flow domain. The fluid properties, defined on the entire calculation domain, change abruptly at the phases boundary. The presence of the liquid-gas interface is modeled using a source term for the surface tension force [22]. The transport equations take the following form:

$$\rho \left[\frac{\partial \mathbf{u}}{\partial t} + (\mathbf{u} \cdot \nabla) \mathbf{u} \right] = \nabla \cdot [\mu (\nabla \mathbf{u} + (\nabla \mathbf{u})^T)] - \nabla p + \rho \mathbf{g} + \mathbf{f}_\sigma \quad (2.6)$$

$$\nabla \cdot \mathbf{u} = 0 \quad (2.7)$$

Here, \mathbf{u} is the fluid velocity field, ρ and μ are the fluid density and dynamic viscosity, respectively, p is the pressure, \mathbf{g} is the gravity acceleration, and \mathbf{f}_σ is the interface tension force which appears at the location of the interface. A multidimensional delta function is needed, which is non-zero where the interface is located. It can be written as:

$$\mathbf{f}_\sigma = \delta(\mathbf{F}_\sigma) = \int_{\Delta_s} \sigma \kappa \mathbf{n} ds \quad (2.8)$$

where Δ_s is a surface element, \mathbf{n} is the unit normal to the interface, σ is the surface tension coefficient, κ is the curvature of the interface. Since the formulation is the same as for the single-phase flows, the boundary conditions and the solution method are similar to that for the single phase flow. The additional requirement is finding the interface. In the next section, a brief review of interface tracking and capturing methods will be given.

2.2.2 Interface tracking and capturing methods

Finding the interface can be done in an explicit way or in an implicit way. If the interface is represented by marker points, the surface front can be moved accurately in a Lagrangian way. The interface is always known while it's moving. This kind of method is often called *Interface Tracking Method*. The Front tracking method is one of such methods.

On the contrary, the interface may be described implicitly using a field function. The implicit scalar is advected with the liquid using a transport equation. This method often called *Interface Capture Method*. Since the interface is implicit, a reconstruction procedure is needed for this method. The Level-Set method and Volume-of-fluid method are both interface capture methods. The following section will introduce these three methods.

Level-Set method

The Level-Set method was introduced by Fedkiw [40]. The main idea is to define a smooth function $\phi(\mathbf{x}, t)$, which is the signed minimum distance of \mathbf{x} to the interface. Here $\mathbf{x} = (x_1, x_2, x_3) \in \mathbf{R}^3$. For example, if the level set function ϕ is positive, the \mathbf{x} locates in the liquid. If it is negative, the \mathbf{x} is in the gas phase. Therefore, the liquid-gas interface is the zero level set of ϕ . Note that we also have $|\nabla\phi| = 1$. For example in Fig. (2.2), the bubble interface is the circle where the level-set is $\phi = 0$. The level set function evolves with time (t). The interface moves with the fluid velocity \mathbf{u} . This can be obtained by solving the transport equation:

$$\frac{\partial\phi}{\partial t} + \mathbf{u} \cdot \nabla\phi = 0 \quad (2.9)$$

Special care must be taken when resolving the property discontinuity at the interface. The solution will yield numerical instabilities due to large density and viscosity changes at the interface. A smoothing method is proposed by Sussman et al. [103]. The density and viscosity on the interface can be written as:

$$\begin{aligned} \rho(\phi) &= \rho_g + (\rho_l - \rho_g)H(\phi) \\ \mu(\phi) &= \mu_g + (\mu_l - \mu_g)H(\phi) \end{aligned}$$

where ρ_g, ρ_l are the density of the gas and liquid phase, μ_g and μ_l are the viscosity of the gas and liquid. $H(\phi)$ is the Heaviside function given by

$$H(\phi) = \begin{cases} 0 & \text{if } \phi < 0 \\ 1/2 & \text{if } \phi = 0 \\ 1 & \text{if } \phi > 0 \end{cases} \quad (2.10)$$

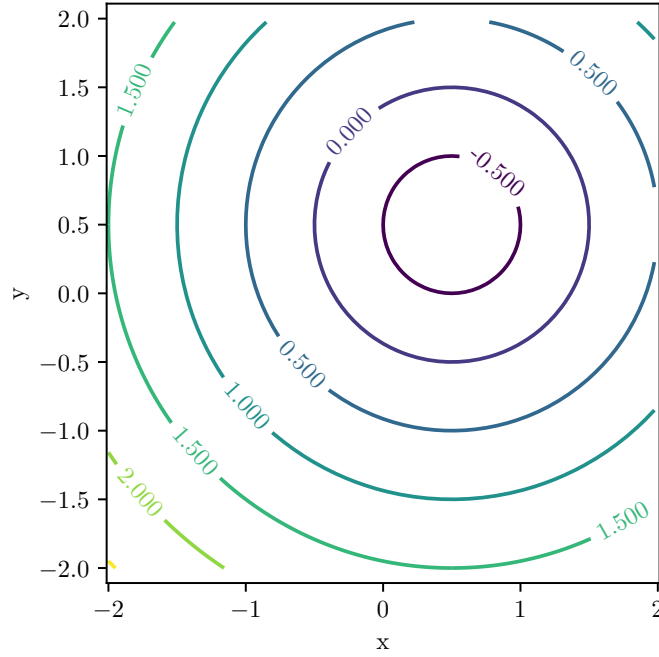


FIGURE 2.2: Iso-level curves from a level-set formulation. The circular bubble initialized at $(x = 0.5, y = 0.5)$ with 1.0 radius.

A smoothed Heaviside function $H_\epsilon(\phi)$ can be constructed to obtain the smeared fluid properties on the interface:

$$H_\epsilon(\phi) = \begin{cases} 0 & \text{if } \phi < -\epsilon \\ (\phi + \epsilon)/(2\epsilon) + \sin(\pi\phi/\epsilon)/(2\pi) & \text{if } |\phi| \leq \epsilon \\ 1 & \text{if } \phi > \epsilon \end{cases} \quad (2.11)$$

where ϵ is the thickness of the smoothed interface, generally taken as $\epsilon = 3\Delta x/2$. When the level-set function advects with the equation (2.9), one of the major difficulties of the level-set method is that the fluid mass is not conserved. Another problem is that the signed distance property ($|\nabla\phi| = 1$) will be lost and the field function can become highly irregular. These problems can be remedied by multiple ways. First, we can choose high-order schemes to discretize the equation (2.9). Second, we can add a reinitialization procedure which is proposed by Sussman, Smereka, and Osher [102]. This procedure ensures the condition $|\nabla\phi| = 1$ by solving the following equation:

$$\frac{\partial\phi}{\partial\tau} + \text{sgn}(\phi_0)(|\nabla\phi| - 1) = 0 \quad (2.12)$$

where $\text{sgn}(\phi)$ is a sign function, τ is an artificial time, ϕ_0 is the un-initialized field. This equation can be solved to steady state. But, in practice, Sussman et al. [103] found only two or three iterations are sufficient.

Compared to the Front tracking method, the level-set method avoids adding and removing markers to represent the moving interface. Level-set methods can deal with the merging

and breaking of the interface easily. Furthermore, the generalization to three dimensions is rather straight forward [102].

Front tracking method

The front tracking method is an interface tracking method for two-phase flows developed by Unverdi and Tryggvason [113]. The basic idea of this method is defining the interface by markers moving with the fluid velocity, see Fig. 2.3. While governing equations for the one-fluid formation are solved on a fixed mesh, the interface is represented by an array of points. These points are connected to each other often through a linked lists which contains pointers to the previous and the next object in the list. The three-dimensional front is built in the same way, but the front is represented by triangles. The front points move in a Lagrangian way,

$$\frac{d\mathbf{x}_s}{dt} \cdot \mathbf{n} = \mathbf{u}_s \cdot \mathbf{n} \quad (2.13)$$

where \mathbf{x}_s is the front points coordinate, \mathbf{u}_s is the velocity of the front points. When the front moves, it deforms and stretches along with the flow field. The resolution may become inadequate at some locations. To keep the method accurate, new points are added to the original front. Also, it is desirable to remove small elements, especially those containing "wiggles" which are smaller than the grid size.

Information needs to be transferred between the two grids. For example, the \mathbf{u}_s is obtained by interpolating from grid values to the front locations. In two-phase flows, the surface tension is calculated at the interface, but the Navier-Stokes equations are solved on a fixed grid. The transfer operation can be done in many ways, but it is necessary that the transferred quantity is conserved. The interface quantity, ϕ_f , is a surface average, whereas the grid value, ϕ_g , is a volume average. The conservation requires:

$$\int_{\Delta_s} \phi_f ds = \int_{\Delta_v} \phi_g dv \quad (2.14)$$

After advecting the front, the fluid properties, such as the density and the viscosity, need to be redefined. This can be done by taking the numerical divergence of the grid-density gradient results in a numerical approximation to the Laplacian:

$$\Delta\rho = \nabla_h \cdot \nabla_h \rho_{i,j} \quad (2.15)$$

where ∇_h is gradient operator on the grid with an uniform mesh space h .

The advantage of this method is that interface advection and properties, such as surface tension, can be computed very accurately. The interface resolution is independent of the mesh resolution. The drawbacks are a cumbersome implementation, especially in three dimensions. It is not easy to handle the interface breakup and coalescence problems.

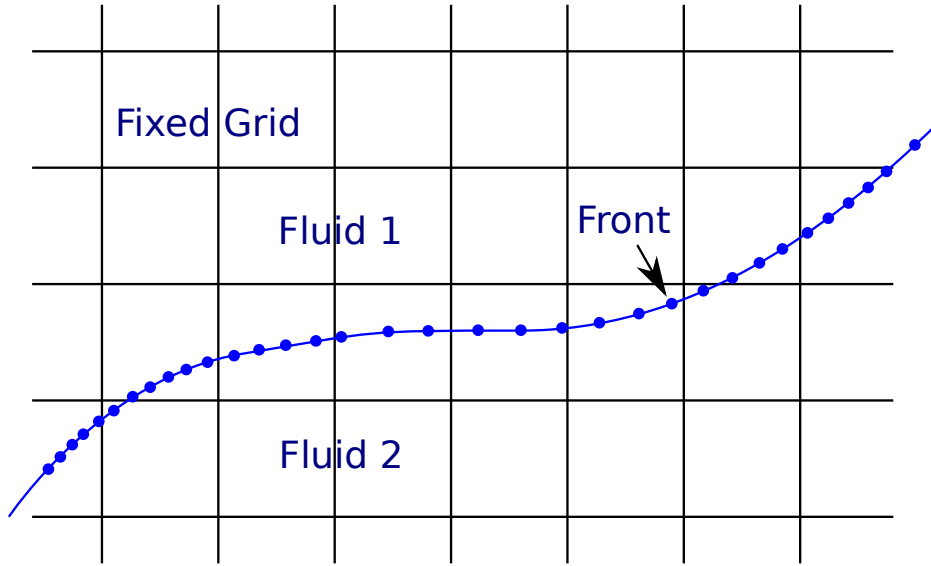


FIGURE 2.3: An example of the front of Front-tracking method and its background grid. [109]

Volume of fluid method

The volume of fluid method tracks a phase indicator function defined in each control volume. The method was first proposed by Hirt and Nichols [46]. The phase indicator function c (also known as volume fraction or color function) is defined as:

- $c = 0$ if the control volume is filled with phase 1
- $c = 1$ if the control volume is filled with phase 2
- $0 < c < 1$ for mixed control volumes containing the interface

In order to obtain the fluid property in each phase, a generic fluid property ϕ (e.g. density, viscosity) can be computed from:

$$\phi = c\phi_1 + (1 - c)\phi_2 \quad (2.16)$$

The volume fraction c is governed by the simple advection equation:

$$\frac{\partial c}{\partial t} + \nabla \cdot (\mathbf{u}c) = 0 \quad (2.17)$$

One of the critical issues with the VOF method is finding a proper way to discrete equation (2.17). Lower-order schemes smear the interface due to numerical diffusion, while high-order schemes are unstable and result in numerical oscillations. Thus, several volume advection techniques have been proposed to avoid undesirable numerical effects and keep the interface sharp.

A widely used technique is to compute the geometry of the interface in the control volume and then calculate the flux across the adjacent control volumes. The procedure to compute the actual geometry of the interface is called *interface reconstruction*. The simplest way to

represent the interface is using vertical or horizontal lines. Noh and Woodward [74] proposed the *Simple Line Interface Calculation* (SLIC) algorithm. The interface control volume is split by vertical and horizontal lines. If the advection is in the horizontal direction, the vertical line is an approximation of the interface, *vice versa* in the other direction. Therefore, there are two lines (or three lines) to approximate the interface depending on the advection direction. Hirt and Nichols [46] modified this method by only using one straight line to approximate the interface. The line is still parallel to the coordinate axis. The c in neighbor cells are used to selected the orientation of the straight line. Youngs [120] developed the *Piecewise Linear Interface Calculation* (PLIC) algorithm, using an arbitrarily oriented line to approximate the interfaces. This method has a better approximation to the interface. The equation of the interface segment can be written as

$$\mathbf{m} \cdot \mathbf{x} = \alpha \quad (2.18)$$

where, \mathbf{m} is the normal vector to the interface and α is the distance to the origin of \mathbf{x} . Many studies show that the key to improving advection scheme is finding a better way to reconstruct the interface. Base on the PLIC method, we should know the orientation of line segments, i.e. obtain the normal vector of the interface. It can be obtained from the gradient of c , equation (2.19). If the normal \mathbf{m} has been calculated, the α is obtained from area conservation. The α can be obtained from a pure geometrical calculation [91].

$$\mathbf{m} = -\nabla c \quad (2.19)$$

Youngs [120] estimates the ∇c by means of finite-difference schemes in a 3×3 in 2D or a $3 \times 3 \times 3$ block stencil in 3D. The ∇c in the center cell (i, j) is computed as the average of the cell-corner values.

$$\begin{aligned} \mathbf{m}_{i,j} &= (m_{x:i,j}, m_{y:i,j}) \\ &= \frac{1}{4} (\mathbf{m}_{i+\frac{1}{2},j+\frac{1}{2}} + \mathbf{m}_{i+\frac{1}{2},j-\frac{1}{2}} + \mathbf{m}_{i-\frac{1}{2},j+\frac{1}{2}} + \mathbf{m}_{i-\frac{1}{2},j-\frac{1}{2}}) \end{aligned} \quad (2.20)$$

where,

$$\begin{aligned} \mathbf{m}_{x:i+\frac{1}{2},j+\frac{1}{2}} &= -\frac{1}{2} \left(\frac{c_{i+1,j+1} - c_{i,j+1}}{\Delta x} + \frac{c_{i+1,j} - c_{i,j}}{\Delta x} \right) \\ \mathbf{m}_{x:i-\frac{1}{2},j+\frac{1}{2}} &= -\frac{1}{2} \left(\frac{c_{i,j+1} - c_{i-1,j+1}}{\Delta x} + \frac{c_{i,j} - c_{i-1,j}}{\Delta x} \right) \\ \mathbf{m}_{x:i+\frac{1}{2},j-\frac{1}{2}} &= -\frac{1}{2} \left(\frac{c_{i+1,j} - c_{i,j}}{\Delta x} + \frac{c_{i+1,j-1} - c_{i,j-1}}{\Delta x} \right) \\ \mathbf{m}_{x:i-\frac{1}{2},j-\frac{1}{2}} &= -\frac{1}{2} \left(\frac{c_{i,j} - c_{i-1,j}}{\Delta x} + \frac{c_{i,j-1} - c_{i-1,j-1}}{\Delta x} \right) \end{aligned}$$

We can obtain m_y in a similar way. Numerical tests have showed the weakness of this method which can not represent linear interfaces accurately. Other methods have been proposed. The block cells are always 3×3 . The volume fractions can be added along the vertical direction and horizontal direction, which can be defined as a height function $y = f(x)$ and a width function $x = g(y)$ as shown in Fig. 2.4. For example, the height y_{i-1} is given by the expression

$y_{i-1} = \Delta x \sum_{k=-1}^1 C_{i-1,j+k}$. We approximate the height function $y = f(x)$ in the central cell of the block with the equation

$$\text{sgn}(m_y)y = -m_{xc}x + \alpha' \quad (2.21)$$

Here, the slope of the straight line, equal to m_{xc} is calculated by a central difference scheme.

$$m_{xc} = -\frac{1}{2\Delta x}(y_{i+1} - y_{i-1}) \quad (2.22)$$

We can also describe the line slope by m_{yc} . The similar equation obtained:

$$\text{sgn}(m_x)x = -m_{yc}y + \alpha'' \quad (2.23)$$

And,

$$m_{yc} = -\frac{1}{2\Delta y}(x_{i+1} - x_{i-1}) \quad (2.24)$$

It is evident that a given line just has one correct slope. The strategy is to choose a proper slope for the interface. If the real interface orients as shown in Fig. 2.4(A), we take m_{yc} as the real slope. Otherwise, we take m_{xc} as the real slope (Fig. 2.4(B)). A simple expression can be used to select slope

$$|m^*| = \min(|m_{xc}|, |m_{yc}|) \quad (2.25)$$

Similarly, we can consider obtaining the slope by using forward and backward finite-difference method. Six slopes can be obtained in each 3×3 block. The more sophisticated method is needed to obtain the best slope of the line. Pilliod Jr. and Puckett [79] proposed the ELVIRA (efficient least-squares VOF interface reconstruction algorithm) method. For each of the six slope, the corresponding new line cuts the 8 neighbor cells and obtains the new volume fraction c' in each cell. The area error in L_2 is

$$\|e\|_2 = \sum \sum (c'_{i,j} - c_{i,j})^2 \quad (2.26)$$

The final slope selection is the one that has the minimum error. The calculation blocks can be changed, and even take more blocks. However, considering the accuracy and calculation load, a 3×3 block is a common choice in most studies. One drawback of the ELVIRA is the required computation time, especially in three dimensions. A 3D version of ELVIRA has been implemented by Miller and Colella [68].

Scardovelli and Zaleski [92] proposed a new least-squares fit method. This method is based on aforementioned methods. Firstly, we obtained the line segments in each interface cell as the preliminary interface. Then, selecting few points on the segments (e.g. two end points and mid point). Finally, new slope can be obtained by the least-squares fit method. This method shows a better representation at high curvature regions.

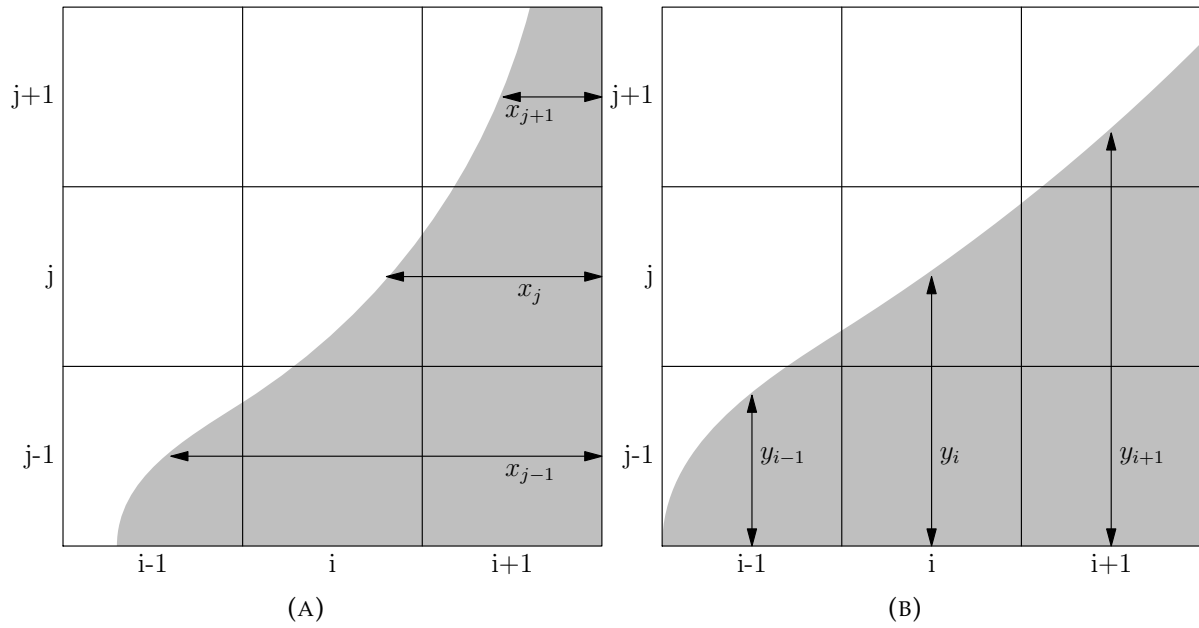


FIGURE 2.4: Calculating volume fraction column-wise and row-wise to estimate the line slope.

2.3 Bubble motion in channels

The bubble motion in channels is often classified as the bubble or slug flow regime. If the bubbles are small enough compared to the size of the containing channel, this flow regime is often referred to bubbly flow. If the bubble is large enough to occupy most of the cross-sectional area of the channel, this flow regime is often referred to slug flow.

It is known that slug flow allows great heat and mass transfer between the two phases. Therefore, the slug flow regime has drawn much attention. A large quantity of research has been done in the past decades. For clarity, the slug flow regime is influenced by many different environmental conditions which can be classified into different subgroups.

- The channels have different cross-sectional shapes. In common conditions, the bubble flows in a circular channel. Whereas, the bubble flowing in non-circular channels exists in porous materials and blood vessels. For example, Taha and Cui [106] simulated slug flow in square micro-channels. The liquid film thickness does not distribute around the bubble evenly. Therefore, the heat transfer coefficients are different on the circular direction of the tube. Roig et al. [87] investigated the bubble rising in a vertical Hele-Shaw cell and reported a detailed analysis of path and shape oscillations of an air bubble.
- The movement of the bubbles is due to different driving forces. The gravitational force drives the bubble moving upwards. The pressure pushes both the liquid and the bubble moving forward. Different driving forces have different effects on the bubbles. If the bubble is only driven by gravitational force in the vertical channel, the bubble head will be a bullet shape, the liquid moving downward around the bubble. And, the liquid film becomes thinner from the top to the bottom of the bubble. If the gravitational force balance the viscosity force, the liquid film thickness will remain constant. And, the

bubble rises at a constant velocity. If the bubble is only driven by pressure, the bubble behaves differently. For example, the bubble moves in a horizontal tube and is pushed by the liquid flow. Some of the capillary waves can be observed at proximity to the rear of the bubble. The liquid film thickness decreases from the nose to the rear of the bubble. Depending on the operating conditions, the film thickness may even equal to 0 (dry out).

- The orientation of the channels has great effects on the bubble motion. For the vertical channels, the bubble moving upward driven by the buoyancy forces. And, the pressure difference may also exist. As pointed out by Nicklin [70], the velocity of the bubble in upward flow consists of two parts, the mean liquid velocity (U^*) and the bubble velocity in quiescent liquid (V_T). The overall bubble velocity can be expressed as:

$$V^* = C_0 U^* + V_T \quad (2.27)$$

where C_0 is the distribution parameter which accounts for the relative velocity between the two fluids. It is assumed that U^* is independent of V_T [85]. Therefore, the bubble velocity prediction can be investigated separately. While the real fluid mechanics are non-linear, the linear assumption for the bubble velocity has proven to be successful in the literature. For the bubble moving in horizontal channels, if both pressure and buoyancy cannot be ignored, the film thickness above the bubble becomes thinner. Wall dry out may occur at the top of the tube under some operation conditions.

In the next section, the discussion focuses on the rising bubble in the vertical circular channel. We do not intend to provide a comprehensive review covering all aspects of slug flow. Instead, we summarized the works which we considered as the milestone for Taylor bubble rising in the vertical circular channel. These studies have close relation and provide fundamental knowledge for the present thesis. Other reviews about slug flow can be found in [6].

2.3.1 Rising bubbles in vertical channels

Gas bubbles rising in the vertical channels often appear as bullet shapes. The motion of bubbles is affected by the shape of channels. These bubbles are often called Taylor bubbles [33]. The pioneer investigation about the Taylor bubble is presented by Dumitrescu [38]. The following sections will review the major studies on Taylor bubbles. The methods used to investigate this phenomenon is the analytical model, experiments and numerical simulation. First of all, the analytical model will be introduced. It describes the forces acting on the bubbles. Then, three major study objective about the Taylor bubble will be presented: the bubble terminal velocity, the falling film, and the bubble nose shape. Finally, a brief review of both experimental and simulation studies will be shown.

Firstly, we consider a single bubble rising in a stagnant liquid. If the pressure in the gas is constant, the drift velocity V_T of the bubble is also constant. The value of V_T depends on various forces in the two-phase flow system. A general scaling analysis of the Taylor bubble

or drop motion is presented by Hayashi, Kurimoto, and Tomiyama [44]. Here, we consider that the liquid is the continuous phase (C) and the gas is disperse phase (D). There are six different forces governing the dynamics of a Taylor bubble, i.e., inertial (F_{iC} and F_{iD}), viscous ($F_{\mu C}$ and $F_{\mu D}$), surface tension (F_s) and buoyant (F_b) forces. These forces can be regrouped in the following dimensionless numbers:

$$\begin{aligned}
\text{Froude number: } Fr &= \sqrt{\frac{F_{iC}}{F_b}} = \frac{V_T}{\sqrt{\Delta\rho g D / \rho_c}} \\
\text{inverse viscosity number: } N_f &= \sqrt{\frac{F_{iC} F_b}{F_{\mu C}^2}} = \frac{\sqrt{\Delta\rho g D^3}}{\mu_C} \\
\text{Eötvös number: } Eo &= \frac{F_b}{F_s} = \frac{\Delta\rho g D^2}{\sigma} \\
\text{Reynolds number: } Re_D &= \frac{F_{iC}}{F_{\mu C}} = \frac{\rho_C V_T D}{\mu_C} \\
\text{Morton number: } Mo &= \frac{F_{\mu C}^4 F_b}{F_s^3 F_{iC}^2} = \frac{g \mu_C^4 \Delta\rho}{\rho_C^2 \sigma^3} \\
\text{density ratio: } r_\rho &= \frac{F_{iD}}{F_{iC}} = \frac{\rho_D}{\rho_C} \\
\text{viscosity ratio: } r_\mu &= \frac{F_{\mu D}}{F_{\mu C}} = \frac{\mu_D}{\mu_C}
\end{aligned} \tag{2.28}$$

Only four dimensionless groups are independent, i.e. N_f , Eo , r_ρ and r_μ . The Morton number can be derived by Eo and N_f , $Mo = Eo^3 / N_f^4$. The Archimedes number is obtained from the manipulation of N_f ($Ar = N_f^2$) [10]. The Fr and Re_D can be obtained after knowing the V_T . The pipe inclination θ can be added to the dimensionless analysis. Zukoski [123] and Fabre and Liné [39] expressed this dependency through a general relationship.

$$V_T = C_T(N_f, Eo, \theta) \sqrt{\frac{g \Delta\rho D}{\rho_C}} \tag{2.29}$$

This relationship ignores the viscosity ratio μ^* . In fact, the density and viscosity ratios are often ignored in the studies of Taylor bubble. The density and viscosity of the gas are generally much less than those for the liquid ($\rho_C \gg \rho_D$, $\mu_C \gg \mu_D$). Therefore, the density and viscosity ratios are both equal to 0 [118, 116].

White and Beardmore [118] performed a wide range of experiments. The Eo number ranges from 3 to 400. And, The Mo number ranges from 10^{-12} to 10^3 . As mentioned before, White and Beardmore [118] have ignored the density and viscosity of the gas phase. The characteristic density and viscosity correspond to the liquid phase. They summarized the results to show the dependence of the terminal velocity on each effect. According to the Fig. 2.5, the following regime can be identified:

- $Eo < 4$: The bubble does not rise. Gravitational effects are negligible.
- $Eo > 70$: Capillary effects are negligible.
- $Fr < 0.05$: Inertial effects are negligible.

where

$$t = \log_{10}\left(\frac{\rho_C g D^2}{\sigma}\right) \quad (2.32)$$

The parameters a_i are seventh-degree polynomials:

$$a_i = \sum_{j=1}^8 c_{ij} x^{j-1} \quad (i = 1, \dots, 4)$$

$$x = \log_{10}(\text{Mo})$$

the coefficients c_{ij} are given by the matrix:

$$\begin{bmatrix} 3.5603852 \times 10^{-1} & 2.6717658 \times 10^{-3} & -2.7121907 \times 10^{-3} & -2.0001955 \times 10^{-3} \\ 1.5642441 \times 10^{-3} & 2.8532721 \times 10^{-4} & 4.7831508 \times 10^{-5} & 3.605927 \times 10^{-5} \\ 3.059819 & -5.2353564 \times 10^{-1} & 3.3906415 \times 10^{-2} & 2.1368428 \times 10^{-2} \\ 2.3221312 \times 10^{-2} & -1.809746 \times 10^{-3} & 9.3468732 \times 10^{-5} & -2.3440168 \times 10^{-4} \\ 8.622533 \times 10^{-5} & 5.7198751 \times 10^{-5} & -2.4316663 \times 10^{-6} & -6.7582431 \times 10^{-7} \\ 7.6382727 \times 10^{-6} & 1.1736259 \times 10^{-6} & -1.5186036 \times 10^{-7} & 1.9756221 \times 10^{-8} \\ -3.2676237 \times 10^{-3} & -7.302379 \times 10^{-4} & 7.2215493 \times 10^{-5} & 1.1273658 \times 10^{-5} \\ 5.9716008 \times 10^{-5} & 9.7852173 \times 10^{-6} & -1.3514105 \times 10^{-6} & -1.74642 \times 10^{-7} \end{bmatrix}$$

Wallis [116] proposed a more general equation based on experimental data. The C_T can be expressed as:

$$C_T = 0.345(1 - e^{-\frac{0.01N_f}{0.345}})(1 - e^{-\frac{3.37 - \text{Eo}}{m}}) \quad (2.33)$$

where,

$$m = \begin{cases} 25 & N_f < 18 \\ 69N_f^{-0.35} & 18 \leq N_f \leq 250 \\ 10 & N_f > 250 \end{cases} \quad (2.34)$$

This estimation also ignores the density difference between the liquid and gas. Therefore, $\Delta\rho \approx \rho_C$, and then, $\Delta\rho/\rho_C$ equals to 1. Tung and Parlange [111] studied the terminal state of the Taylor bubble in a long vertical pipe. They showed that the bubble velocity is reduced as surface tension effects are more pronounced. They proposed a correlation as follow:

$$V_T = (0.136 - 0.944 \frac{\sigma}{\rho_C g D^2})^{1/2} \sqrt{gD} \quad (2.35)$$

Bendiksen [17] proposed a correlation ignoring the viscous forces. This correlation is valid for the Taylor bubble with relatively small surface tension.

$$V_T = 0.486 \sqrt{1 + \frac{20}{\text{Eo}} \left(1 - \frac{6.8}{\text{Eo}}\right) \frac{1 - 0.96e^{-0.0165\text{Eo}}}{1 - 0.52e^{-0.0165\text{Eo}}}} \quad (2.36)$$

Viana et al. [115] summarized experimental data in the literatures and 7 new experiments.

A new correlation has been proposed. For a fixed Eötvös number, the Froude number depends on the buoyancy Reynolds number, $Re_D = (D^3 g \Delta \rho_C)^{1/2} / \mu$. Three separate equations are obtained in different Re_D range. For large Re_D (>200) they found

$$V_T = 0.34 / (1 + 3850 / Eo^{3.06})^{0.58} \sqrt{gD} \quad (2.37)$$

For small Re_D (<10) they found

$$V_T = \frac{9.494 \times 10^{-3}}{(1 + 6197 / Eo^{2.561})^{0.5793}} Re_D^{1.026} \sqrt{gD} \quad (2.38)$$

In the transition region ($10 < R_D < 200$), the equation becomes

$$V_T = L[R_D; A, B, C, G] = \frac{A}{(1 + (R/B)^C)^G} \sqrt{gD} \quad (2.39)$$

where

$$\begin{aligned} A &= L[Eo; a, b, c, d] \\ B &= L[Eo; e, f, g, h] \\ C &= L[Eo; i, j, k, l] \\ G &= m/C \end{aligned}$$

and the parameters (a, b, ..., l) are

$$\begin{aligned} a &= 0.34 & b &= 14.793 & c &= 3.06 & d &= 0.58 \\ e &= 31.08 & f &= 29.868 & g &= 1.96 & h &= 0.49 \\ i &= 1.45 & j &= 24.867 & k &= 9.93 & l &= 0.094 & m &= 1.0295 \end{aligned}$$

In our study, we find that the equation (2.39) can be applied to the region of large R_D (>200) and small R_D (<10).

Mandal, Das, and Das [64] proposed a semi-empirical equation based on the experiments of liquid-liquid bubble rising. Therefore, their correlation takes the density and viscosity of the dispersed phase into account.

$$V_T = 0.3507 \sqrt{\frac{\rho_C - \rho_D}{\rho_C} g D} \sqrt{1 - \frac{-1 + \sqrt{1 + 2ND}}{ND}} \quad (2.40)$$

where

$$N = [1.81 \frac{(\rho_C - \rho_D) \rho_C}{\mu_C^2} g]^{1/3} \quad (2.41)$$

For large buoyancy Reynolds number ($Re_D > 200$), they considered the effect of interfacial

tension using a correction as [116]. Equation (2.40) is corrected by multiplication with following term:

$$\frac{1}{\left(1 + \frac{3805}{\text{Eo}_D^{3.06}}\right)^{0.58}} \quad (2.42)$$

Hayashi, Kurimoto, and Tomiyama [44] proposed a more general correlation for the Taylor drop. This correlation covers wide range of conditions, i.e. $0.002 < \text{Re}_D < 4960$, $4.8 < \text{Eo}_D < 228$, $0 \leq \mu^* \leq 70$, $1 < N_f < 14700$, $-12 < \log \text{Mo} < 4$, and $d/D < 1.6$, where d is the sphere-volume equivalent drop diameter.

$$\text{Fr} = \sqrt{\frac{0.0089}{0.0725 + \frac{1}{\text{Re}_D}(1 - 0.11\text{Re}_D^{0.33})} \left(1 + \frac{41}{\text{Eo}_D^{1.96}}\right)^{-4.63}} \quad (2.43)$$

If we ignore the density and viscosity ratio, they equal to 0, the equation (2.43) simplifies to

$$\text{Fr} = \sqrt{\frac{0.01}{0.0816 + \text{Re}_D^{-1}} \left(1 + \frac{41}{\text{Eo}_D^{1.96}}\right)^{-4.63}} \quad (2.44)$$

The equation agrees with the experimental data of White and Beardmore [118] within a $\pm 10\%$ error.

A special region in Fig. 2.5 needs further investigation, which is the region $\text{Eo} < 4$. White and Beardmore [118] stated that the bubble will not rise when $\text{Eo} < 4$. Others have shown similar results. Bretherton [23] gave $\text{Eo} < 3.37$, Barr [14] $\text{Eo} < 5.8$, Bendiksen [17] $\text{Eo} < 4.7$. The correlations (2.39, 2.43) also show that the rise velocity decreases as the Eo number decreases. In fact, these bubbles are with large surface tensions but in small tubes. They may stick on the pipe preventing draining [42]. Another study could prove this theory. Bi and Zhao [19] studied the Taylor bubble in miniaturized circular and non-circular channels. They found that for the triangle and rectangular channels, elongated bubbles always rise upward even though the hydraulic diameter of the tube is 0.866 mm. Whereas, the bubble stopped in circular tubes when $D < 2.9$ mm. Funada et al. [42] pointed out that surface tension cannot close the sharp corners where drainage can occur.

Falling film

The studies on the falling film around a Taylor bubble follow previous work on general falling films. The most representative theoretical analysis on the falling film of viscous liquid is proposed by Nusselt [75]. He derives a solution for the film thickness.

$$\lambda = \left[\frac{3\mu_C^2}{4\rho_C^2 g} \text{Re}_f\right]^{1/3} \quad (2.45)$$

where λ is the film thickness, $\text{Re}_f = 4\rho_C \lambda V_f / \mu$ is the film Reynolds number. V_f is liquid velocity in the liquid film. This model is applicable for laminar film flow. If $\text{Re}_f > 1000$, the model under predicts film thickness due to the turbulent transition in the falling film.

For dealing with the falling film around a Taylor bubble, we define a dimensionless film thickness $\lambda' = \lambda/r$. The thin-film theory can be applied. When the film is thin ($\lambda' \rightarrow 0$), we

can assume that the bubble Reynolds number ($\text{Re}_b = \rho_C V_T D_b / \mu$) equals the film Reynolds number (Re_f). The equation (2.45) becomes:

$$\lambda' = \left[\frac{6\text{Re}_b}{N_f^2} \right]^{1/3} = \left[\frac{6\text{Fr}}{N_f} \right]^{1/3} \quad (2.46)$$

The film thickness λ' can be expressed as a function of N_f . The upper limit for N_f in equation (2.46) is 3000. Dukler and Bergelin [37] proposed a correlation for laminar-to-turbulent flow.

$$\text{Re}_b = 4\eta(3 + 2.5\ln\eta) - 256 \quad (2.47)$$

where η can be rewritten in terms of the inverse viscosity and the dimensionless film thickness (i.e., $\eta = N_f(0.5\lambda')^{1.5}$). Brown [25] proposed a more general quadratic solution based on the constant Froude number assumption.

$$\lambda' = 2 \frac{\sqrt{1 + 2.44N_f^{2/3}} - 1}{2.44N_f^{2/3}} \quad (2.48)$$

Llewellyn et al. [61] proposed a model that avoids both the thin-film and the constant Froude number assumption. They call it the 'Cubic Brown' model.

$$\lambda'^3 + a\lambda' - a = 0, \quad \text{where } a = 6\text{Fr}/N_f \quad (2.49)$$

This results is based upon the assumption of laminar flow and valid for $N_f < 3000$. There are a few empirical correlations proposed based on the experiments or simulations [54, 59, 53]. We summarized these equations in table (2.1)

TABLE 2.1: Summary of the models for liquid film of the Taylor bubble presented in literature. [61]

Source	Equation(s)	Validity
Nusselt [75]	Equation (2.45)	$N_f < 3000$
Dukler and Bergelin [37]	$\text{Re}_b = 4\eta(3 + 2.5 \ln \eta) - 256$ $\eta = N_f \left[\frac{\lambda'}{2} \right]^{3/2}$	$1500 < N_f < 9000$
Lel et al. [59]	$\lambda' = \frac{2 + 0.641\text{Re}_b^{0.47}}{N_f^{2/3}}$	$40 < N_f < 9000$
Karapantsios and Karabelas [54]	$\lambda' = \frac{0.451\text{Re}_b^{0.538}}{N_f^{2/3}}$	$9000 < N_f < 44000$
Brown [25]	Equation (2.48)	$120 < N_f$
Kang, Quan, and Lou [53]	$\lambda' = 0.64N_f^{-0.2}$	$10 < N_f < 450$
Llewellyn et al. [61]	Equation (2.49)	laminar

Another issue related to falling film is the length of the developing film (Z^*). If film developing length is greater than Z^* , the radial component of the film velocity approximately

reaches zero. The Z^* is estimated to be about $2.2D$ for stagnant liquid and about $3.6D$ for co-current flowing liquid [71]. A theoretical estimate of the length Z^* is reported by [28].

$$\frac{Z^*}{D} = \frac{[(g\rho_C\delta/2\mu_C) + V_T]^2}{2gD} \quad (2.50)$$

This equation was deduced supposing unidirectional flow in a liquid film and applying Bernoulli's equation along the free surface streamline. Araujo et al. [10] summarizes the simulation data and reports that Z^*/D depends only on the inverse viscosity number (N_f). The expression is as follows:

$$\frac{Z^*}{D} = 1.033 \quad \text{for } N_f < 90 \quad (2.51)$$

$$\frac{Z^*}{D} = 7.494^{-1} \ln N_f - 2.315 \quad \text{for } N_f > 90 \quad (2.52)$$

Bubble nose

The bullet-shape is the main characteristic of the Taylor bubble. The shape of the bubble nose is closely related to the liquid film and the bubble terminal velocity. Dumitrescu [38] provided the first analyses on bubble nose shape based on potential flow. The nose profile divides into two regions, the nose region and the film region:

$$\left(\frac{z}{D}\right) = 0.375\left[1 - \sqrt{1 - 7.112\left(\frac{r}{D}\right)^2}\right], \quad \frac{z}{D} \leq 0.25 \quad (2.53)$$

where z is the location starting from the tip of the bubble. D is the tube diameter.

$$\left(\frac{z}{D}\right) = \frac{0.0615}{(1 - 4(r/D)^2)^2}, \quad \frac{z}{D} > 0.25 \quad (2.54)$$

This equation shows where the bubble nose developed to a stable liquid film. The critical distance is $Z' = 0.25D$. The values may change base on different experimental operational conditions. Bugg and Saad [27] obtained $Z' = 0.3D$. Polonsky, Barnea, and Shemer [80] report that $Z' = 0.66D$. Whereas, $Z' = 0.55D$ from [114].

Araujo et al. [10] provide a correlation base on the simulation data:

- For lower N_f , the Z'/D are almost independent of Mo and N_f . $Z'/D = 0.483$
- For Mo between 1.64×10^{-2} and 104 , $Z'/D = 2.46 \times 10^{-2} \ln N_f + 0.393$. For $Mo = 4.72 \times 10^{-5}$, $Z'/D = 2.626 \times 10^{-2} \ln N_f + 0.373$.

For a better representation of the nose shape, the estimated nose curvature radius (R_f) was defined, which is also called frontal radius. Araujo et al. [10] report a simple correlation $R_f = 0.794(D/2 - \delta)$. This value almost independents of other parameters. Brown [25] reported a similar result, $R_f = 0.75(D/2 - \delta)$.

Numerical simulations

The main objective of the simulation research on rising Taylor bubble are similar with that of experimental research. The simulation intends to predict the bubble shapes and the velocity of the bubble and the liquid around it. The advantage the numerical simulation is that it can cover a wide range of liquid and gas properties. On the contrary, the experimental studies are limited by the choice of the fluids. Another advantage of simulation is that it provides detailed flow field information. The advanced experimental techniques such as PIV provides data only on the liquid phase around the bubbles. But, the simulations can provide the field information on both phases. And yet, the experiments provide data to validate the numerical simulations.

The incompressible and laminar flow model are good approximations to simulate the Taylor bubble. The observations in experiments have shown that the velocities of both liquid and gas phase are in the range of laminar flow.

The early simulation of the Taylor bubble is presented by Mao and Dukler [67]. The simulation is only performed on the liquid phase. The strategy is rather simple. Firstly, solve the flow field around the Taylor bubble with an initially assumed shape and terminal velocity. Secondly, adjust the bubble shape based on the obtained the velocity field. The new bubble shape also satisfies the balance of the normal stress at the interface of the bubble. Finally, a new bubble terminal velocity can be obtained. Repeat above steps, the final converged velocity field and bubble shape can be obtained.

Tomiyama et al. [107] simulated the Taylor bubble rising with the VOF method. The study shows that simulation could successfully predict the terminal shape of the bubble. The simulation could give appropriate predictions for the influence of the Mo and Eo numbers.

Bugg, Mack, and Rezkallah [26] presented 9 cases of the numerical simulation results which covered $10 \leq Eo \leq 100$ and $10^{-12} \leq Mo \leq 10$. The simulation uses in a finite difference framework with the VOF method to capture the interface. The results is obtained on a 25×400 uniform axisymmetrical mesh. The length of the calculation domain is $8D$. Grid independent test shows that 25 cells in the radial direction are enough to guarantee grid convergence. The gas volume was initially $\pi D^3/3$ which assure that the sure bubbles are at least $2D$ long. Two initial shapes had been tested. The results show that initial shape of the bubble affects only its temporal evolution and not the final shape.

Ndinisa, Wiley, and Fletcher [69] have chosen fluid properties and pipe diameter to yield the dimensionless numbers as follows: $Eo = 100$, $Mo = 0.015$ and $Re_D = 27$. The simulation is performed with the software CFX 5.6. The results agreed well with the experimental data. The study also showed that the need for extremely fine computational meshes for this type of flow, because the velocity gradients around the bubble nose and tail are very high. The simulation also shows that there are no significant oscillations in the wall shear stress at the wake regions. This does not agree with the results presented by Taha and Cui [104]. Lu and Prosperetti [63] studied the Taylor bubbles rising in the vertical tube filled with a quiescent and upward or downward flowing liquid. They also studied the bubble behavior when a sudden pressure drop occurs above the bubble. There is a strong effect on the rising velocity and the bubble volume during the transient. Taha and Cui [105] simulated the bubble motion

TABLE 2.2: Summary of simulations of the Taylor bubble in straight tube presented in literature.

Source	Mo	Eo	Method
Tomiyama et al. [107]	$1 \times 10^{-6} - 1 \times 10^1$	3.3-70	VOF
Bugg, Mack, and Rezkallah [26]	$1 \times 10^{-12} - 1 \times 10^1$	10 - 100	VOF
Son [97]	$2.5 \times 10^{-7}, 2.5 \times 10^{-11}$	84	Level-set
Taha and Cui [105]	$4.7 \times 10^{-5} - 8.0$	5 - 300	VOF
Zheng, He, and Che [122]	$1 \times 10^{-14} - 1 \times 10^{-2}$	158, 160.2, 63.5, 4.23	VOF
Feng [41]	$1.6^{-2} - 5.2$	339.43 - 5984	Boundary fit
Lu and Prosperetti [63]	$1.8 \times 10^{-8} - 1.6 \times 10^{-2}$	15 - 74.6	Front tracking
Kang, Quan, and Lou [53]	$2.09 \times 10^{-4} - 836$	122-203	Front tracking
Araujo et al. [10]	$4.72 \times 10^{-5} - 104$	6-900	VOF

in both stagnant and flowing liquids. The simulation is performed in 3D. The results show that small bubbles were sheered off from the tail due to the liquid jet coming down from the annular film. They found that the wake region depends on the N_f . When $N_f \leq 500$, the wake is composed of two closed toroidal vortices which are axi-symmetric. When $500 \leq N_f \leq 1500$, the bubble tail is nearly flat. The wake tends to lose symmetry around the tube axis. At $N_f \geq 1500$, the bubble wake opens and turbulent eddies are shed from the main bubble wake. Kang, Quan, and Lou [53] adopted the front tracking methodology to investigate the behavior of a Taylor bubble rising in stagnant liquids. They found that Eo and N_f number play a significant role in determining the elongation of the tail and the wake structures. Araujo et al. [10] simulated a wide-range of the Taylor bubble rising corresponding to experimental data [118]. They have investigated the bubble terminal velocity, the development of the liquid film and the wake region. The simulation is carried out by the Fluent software. Araujo, Miranda, and Campos [9, 8] simulated a pair of consecutive Taylor bubbles. The results reveal the process of two bubbles approaching.

Experimental studies

Mao and Dukler [67, 66] studied single Taylor bubbles in a vertical test column. The pipe diameter is 50.8 mm. The measuring section was located 6.68 m above the inlet air nozzle. The numerical method can reliably predict the flow surrounding the Taylor bubble. The numerical simulation also suggests that the rise velocity of a Taylor bubble is essentially independent of viscosity and surface tension for high Re_D ($Re_D > 1850$).

Polonsky, Shemer, and Barnea [81] using two experimental techniques to measured the Taylor bubble motion in a vertical transparent Perspex pipe. The diameter of the pipe is $D = 25$ mm and about 4 m ($170D$) long. Digital image processing is used for the bubble's propagation velocity and shape, while the particle image velocimetry technique is employed for measuring the flow field around the bubble. The results show that negative velocity is observed in front of the Taylor bubble tip. Polonsky, Barnea, and Shemer [80] used the same experimental setup and measured the flow field at the tail of the Taylor bubble. The bottom of the bubble has notable oscillations, which is strongly dependent on the bubble length.

Van Hout et al. [114] investigated the instantaneous velocity fluctuations around the bubble rising in the water. They found that the averaged velocities become negligible at $0.5D$ from the bubble nose and at $12D$ from the bubble tail. Whereas, the instantaneous velocity were found to exist up to $50D$ from the bubble tail.

Bugg and Saad [27] measured the velocity field around rising bubble by particle image velocimetry (PIV). The bubble is produced by injecting air into a tube containing stagnant olive oil. The tube diameter is 19 mm. The fluid properties and pipe diameter described in dimensionless numbers are $Eo = 100$, $Mo = 0.015$ and $Re_D = 27$. The terminal velocity agrees with the theoretical prediction by equation (2.33). The V_T was measured to be 131 mm/s which yielded a Froude number of 0.303. The results show that the influence of the bubble on the surrounding liquid is quite limited. The liquid velocity ahead of the bubble is reduced to 5 % of the bubble velocity at distance of $D/3$. The wake extends further with the velocity dropping to 10 % of the bubble speed at about $0.77D$ below the bubble.

Mandal, Das, and Das [64] investigated the elongated drops rising in vertical tubes. Unlike the study on Taylor bubbles, the density and viscosity play an important role on drop rising velocity. They have tested many liquid-liquid systems, such as the kerosene-water, kerosene-brine, benzene-water.

Santos and Coelho Pinheiro [89] investigated the Taylor bubble rising in a decompression condition. The experiments show that the bubble volume increases as it ascending close the free surface. Two reduced pressures (33.3, 20.0 kPa) and atmospheric pressure were maintained at the free liquid surface to provide a wide range of expansion rates. They reported that the bubble volume expansion rate modifies continuously during the Taylor bubble rising and a well-defined liquid velocity profile can never reach.

A summary of experiments in the literature are shown in Table 2.3 and 2.4. The table summarizes the operational conditions of each experiment. The fluid properties are shown in terms of non-dimensional numbers.

2.4 Bubble motion through expansions and contractions

The changing geometry is widely seen in industry applications. There is relatively few literature investigating this case. Here, we review the results in the literature for the bubble or slug flow in the vertical tube with singularities. And then we show its applications.

2.4.1 Expansions

We have reviewed a variety of topics about the rising Taylor bubble. Much research has been done on these topics. But, there are few of them investigating the Taylor bubbles encountering a change of pipe diameter.

James, Lane, and Chouet [49] reported an experimental investigation on the rising Taylor bubbles through expansions and contractions. The objective of their work was to compare the experimental pressure signals against the seismic data recorded at volcanic sites. The pressure oscillations observed in seismic data may be caused by a large bubble rising through

a sudden expansion. The data exhibited a similar behavior. The experiments investigated a variety of pipe expansions and contractions. The working fluids are the sugar syrup solutions at different concentrations. The pressure sensors are installed at the locations close to the expansion.

Kondo et al. [58] investigated the vertical co-current gas-liquid flow through expansion. The experiments include many cases of the Taylor bubble rising in quiescent liquid. The tube diameter changes from 0.02 m to 0.05 m. The experiment tests air-water two-phase flow at near atmospheric conditions.

Ambrose et al. [5] simulated the bubble rising through expansion. The results were validated with the experiments of [49]. They investigated the variation of the angle of the expansion. The expansion angle (θ) varies from 15° to 90° . The expansion ratio is 2.1. The initial bubble length is $4.4D$. They found that, as θ is decreased, larger volumes of bubble pass through the expansion before splitting into two. For a fixed θ , a critical bubble length can be defined. If the bubble length is less than the critical length, the bubble passes the expansion and remains intact. The study of the expansion ratio shows that the ratio is approximately 2.6, the upper pipe has no effect on the critical length of the bubble.

Rinne and Loth [86] measured bubbly flow in a pipe with sudden expansion (from 40 to 90 mm). A dead region can be found downstream where no bubbles are detected. The experiment shows that the flow downstream has a sudden disturbance and the bubbles redistribution along the pipe.

Other numerical simulations about the pipe flow with expansion or contraction in a horizontal configuration are presented in [112]. The flow was in a flat rectangular channel. The simulation found that the downstream flow pattern is bubble fragments when the gas superficial velocity is lower. In addition, increasing the gas injection, an annular-like flow pattern can be found.

2.4.2 Contractions

Chen et al. [29] investigated the pressure change and flow patterns subject to the influence of sudden contractions. The air and water flow from small rectangular channels into 2 mm round tube. They have revised Abdelall et al. [1]'s homogeneous correlation to predict the pressure drop. They introduced the Bond number and contraction ratio into the original correlation as correction factors. The mean error of the new correlation is reduced to 30 % for the entire database.

Padilla, Revellin, and Bonjour [78] visualized the two-phase flow in horizontal sudden contractions. The tubes' diameter varied from 5.3 to 10.85 mm. A new predicting method for the pressure drop in sudden contractions has been proposed. The correlation has great accuracy. The mean absolute error is around 12 % and the mean relative error is 0.7 %.

Ueda et al. [112] performed a simulation for contraction, the results seemed to be a similar nature against the experimental result.

Kaushik et al. [55] perform a numerical study on the core annular flow through sudden contraction and expansion. The study provides detailed information on the profiles of velocity, pressure and volume fraction over a wide range of oil and water velocities for an abrupt

expansion and contraction. The simulation results were compared to the experimental the results in [13]. Generally speaking, the simulation could enhance the physical insight into this phenomenon.

To our knowledge, there is no previous work about the Taylor bubble rising through the contraction. The bubble behavior in the contraction is still unclear. However, a few applications exist. A brief introduction will be carried out in the next section.

2.4.3 Applications

Photobioreactors

A photobioreactor can be described as an enclosed, illuminated culture vessel designed for controlled biomass production [96]. It is often made up as a transparent tube. The gas is injected at the bottom. The gas bubble rises in the tube, filled with algae. The photosynthesis produce O_2 from injected CO_2 . The objective of the reactor design is increasing the mass transfer rate and quickly remove the O_2 produced by the algae.

Tsoglin et al. [110] suggested a few points to be taken into consideration while designing the photobioreactor. Here, we restate the points related to two-phase bubble flow:

- High rates of mass transfer must be attained by means that neither damage the cultured cells nor suppress their growth.
- The reactor should work with intensive foaming.
- The mircoalgae are highly adhesive. The reactor must prevent or minimize the fouling of the reactor.

The photobioreactor has two sorts of design: bubble column and airlift photobioreactor. The design of the bubble column reactor has lower capital cost than airlift reactor. It consists of the cylindrical vessel with a height greater than twice the diameter. Airlift reactors have two interconnecting parts. One vessel is used for gas mixture and reaction. Another one is down-comer which has no gas. The residence time of gas in various zone affects the performances of the reactor. The reactor has been modified into many shapes in order to boost its efficiency, such as putting sparger into the tube, using a rectangular tube. The disadvantage is that its complexity increases in scale-up [52]. In the study of Yoon, Choi, and Park [119], they investigated the effect of bubble shapes on the growth of cyanobactetria cells in a photobioreactor. The growth rate of cells under slug flow was higher than that under bubbly flow after the cell entered the deceleration phase. They also concluded that the bubble shape in the slug flow was advantageous with regard to the radial circulation of cells. Therefore, larger bubble slug in the airlift reactors may improve their efficiency. The investigation on the slug behavior has great importance for better designing the reactors.

Volcanology

Seismic signals are obtained from low-viscosity magmas flow. Those signal sources are often attributed to dynamic fluid processes [49]. The instigation of acoustic sources applicable

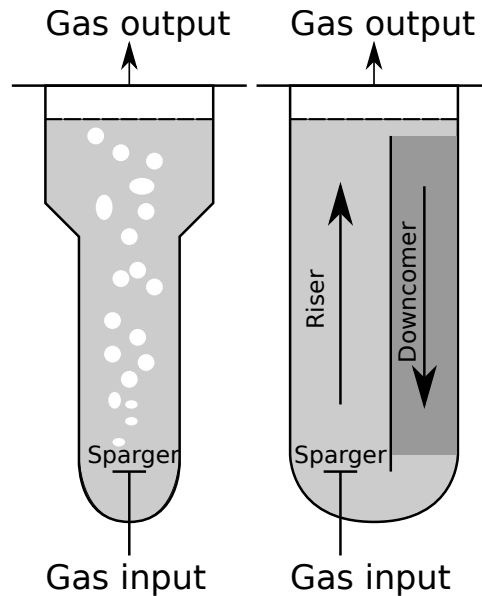


FIGURE 2.6: Bubble column and air lift bioreactors. (Replot based on [96]).

to low-viscosity magmas can be studied by laboratory experiments. James et al. [51] investigated the bursting of gas slugs in liquid-filled vertical and inclined conduits. The experiments were carried out in a vertical straight tube. At the greater depth of magmas, the magma pathways are more likely to be an individual or array of dikes. This suggests that changes in conduit size, shape and angle are likely to be better the representation of the real situation in the experimental investigation.

An example of the slug flow linked with the volcano eruptions behavior is Strombolian volcanoes. It is a relatively small-scale explosive eruption. This phenomenon is widely accepted to be caused by bubble coalescence leading to the formation of Taylor bubbles. The Taylor bubble forms in the great depth of the conduit. When it approaches the lava lake, it undergoes a large expansion to the reservoir. The diagram is shown in Fig. 2.7. Bouche et al. [21] pointed out the Taylor bubbles rising into reservoir may provide hot magma from depth which is entrained in their wake and drive convection currents. James, Lane, and Chouet [49] showed that it is possible to monitor the lava activity from distance by analyzing acoustic data from the bubble break up in the expansion conduit.

2.5 Chapter conclusion

A review of the two-phase flow, bubble rising, Taylor bubble in vertical tube and bubble through the contractions and expansions are presented. Both experimental and simulation works are devoted to this research area. A few conclusions can be drawn from the literature review:

- Existing numerical methods have proven to be sufficiently accurate for simulating the bubble flow in the pipe. Both the interfacial tracking and capturing methods can be used to simulate the bubble motions. Previous work has shown a large quantity of the

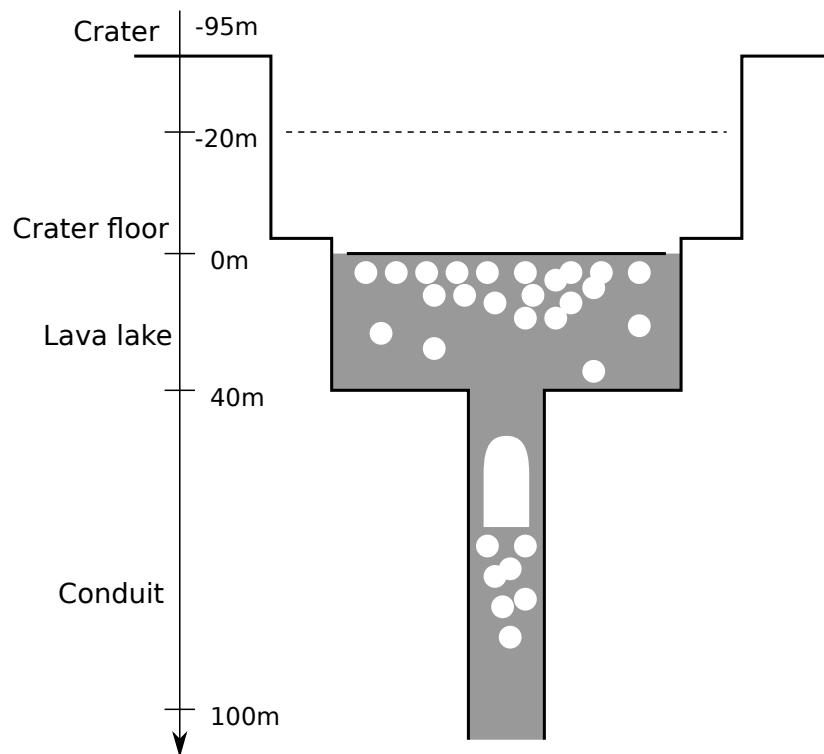


FIGURE 2.7: Diagram of the Taylor bubble in a lava conduit and its rising towards the lava lake. (Replot based on [21]).

simulations related to bubble behavior under a variety of conditions. The simulation results have been validated with the experimental data.

- The Taylor bubble rising in the vertical tube has been investigated thoroughly. Both the numerical and experimental studies have been devoted to this subject. Detailed information about the bubble has been provided, for example, the bubble terminal velocity, the filling film, the shape of the bubble nose, etc. The motion of the Taylor bubble in the straight tube is very well known.
- The investigation about Taylor bubbles rising through expansions is very limited. The investigations on the Taylor bubble only presented its terminal motion in straight pipe. The bubble transitional behaviors in the expansion are unclear.
- The bubble rising through the contractions is still an unknown area. A few studies have investigated the slug flow in the contractions. However, bubble motion encountering the contraction in a quiescent liquid is unknown and needs to be investigated.
- The literature review on two-phase flow clarified the background of the present study. We will focus on the Taylor bubble rising in expansions and contractions.

TABLE 2.3: Summary of the experimental studies of the Taylor bubble rising in vertical tube.

Test facilities	Published articles	Test object	Tube material	Tube size	Liquid properties	Range	Comments
1	[118]	Taylor bubble	Plexiglass	$D_{in} = 5$ to 38.7 mm $L > 0.6$ m	Water, butyric acid solution, sucrose solution, etc.	$Mo = 10^{-11}$ to 10^6	
2	[121] [65]	co-current liquid flow, gas-liquid upward slug flow	gas-Plexiglass	$D_{in} = 50.8$ mm $L = 4.56$ m	Electrolytic solution (NaOH, $K_3Fe(CN)_6$ and $K_4Fe(CN)_6$) air-water system ($\sigma = 0.010$ N/m)		Visualization aided by Rouge Solophenyle 6BL powder
2	[28]	Taylor bubbles rising through stagnant liquids	Acrylic	$D_{in} = 19, 52$ mm	Water, glycerol and aqueous glycerol solutions		
3	[80] [81]	Velocities in front of the bubble	Perspex	$D_{in} = 25$ mm $L = 4$ m	Water		
4	[95]	Taylor bubbles rising	Perspex	$D_{in} = 14$ mm $L = 4$ m	Water, Water-sodium-polywolframate solution, Water-cellulose ester solutions	$Mo = 10^{-11}$ to 10^{-5}	
5	[34] [35] [57]	Stationary Taylor bubbles	Taylor	$D_{in} = 99.7$ mm	Water		Air is blown through centered tubelets. Water is flowing downwards in a vertical tube.

TABLE 2.4: Summary of the experimental studies of the Taylor bubble rising in vertical tube.

Testfacilities	Published articles	Test object	Tube material	Tube size	Liquid properties	Range	Comments
6	[73]	Taylor bubbles rising through stagnant liquids	Acrylic	$D_{in} = 32$ mm $L = 6$ m	Water, glycerol and aqueous-glycerol solutions $\mu_l = 113 \times 10^{-3}$ Pa.s	-	-
6	[71, 72]	Taylor bubbles rising through stagnant liquids and co-current flow	-	-	-	-	-
6	[98, 99]	Taylor bubbles rising through stagnant non-Newtonian liquids	-	-	Carboxymethylcellulose solution (CMC)	-	-
7	[60]	Capillary waves on Taylor bubble	Borosilicate glass	$D_{in} = 14, 26, 44$ mm $L = 6$ m	Water	$Mo = 1 \times 10^{-11}$	-
8	[50]	Gas near surface expansion	Borosilicate glass	$D_{in} = 25$ mm $L = 2$ m	Vacuum oil	$Mo = 0,08$ $Eo = 179$ $N_f = 91$	-
9	[44]	Taylor drops	Acrylic	$D_{in} = 11,0, 20,1, 26,1, 30,8$ mm $L = 530$ mm	Dispersed Silicon oils Continuous phase: glycerol-water solutions	$Mo = 10^{-2,5}, 10^{-4,7}, 10^{-0,45}$ $Eo = 8$ to 91	-
10	[62]	Taylor bubble mini-channel	Polymethyl methacrylate	$D_{in} = 1, 2, 3, 6$ mm $L = 1$ m	Water	$Mo = 1 \times 10^{-11}$ $Eo = 0,136$ to $4,89$	-
11	[90]	Taylor bubble vertical channel	silicon	$D_{in} = 6$ mm $L = 200$ mm	3M Novec ($C_4F_9OCH_3$)	HFE $Mo \approx 1 \times 10^{-14}$	-
12	[114]	Taylor bubble vertical channel	Perspex	$D_{in} = 25$ mm $L = 2$ m	Water	$Mo \approx 1 \times 10^{-11}$	-

Chapter 3

Numerical model and validations

Gerris is a free software to solve the partial differential equations governing two-phase fluid dynamic problems. The source code is available online under the GPL license. This software is used for the simulations in this thesis.

The software solves the time-dependent incompressible Navier-Stokes equations. It also contains the VOF algorithm for interfacial flows. Another great advantage of this software is the Adaptive Mesh Refinement (AMR) algorithm which can adapt the resolution dynamically according to the features of the flow.

The objective of this chapter is to give a brief introduction of this solver, and to validate its ability and accuracy for the two-phase flow of interest in this work. This chapter is organized as follows. Firstly, the governing equations used in the presented simulations are introduced. Secondly, a simulation of single-phase flow is presented for validation purpose. Finally, a comprehensive simulation on the single bubble rising is carried out for testing the software for two-phase flows.

3.1 Introduction of the numerical solver

3.1.1 Governing equations

Gerris solves the incompressible Navier-Stokes equations:

$$\nabla \cdot \mathbf{U} = 0 \quad (3.1)$$

$$\rho \frac{\partial \mathbf{U}}{\partial t} + \rho(\mathbf{U} \cdot \nabla)\mathbf{U} = \nabla \cdot (\mu(\nabla \mathbf{U} + \nabla \mathbf{U}^T)) - \nabla p + \rho \mathbf{f} \quad (3.2)$$

where \mathbf{U} is the velocity, p is the pressure, ρ and μ are the density and viscosity of the fluid, respectively, \mathbf{f} indicates any body forces acting on the fluid. Above equations can be rewritten in dimensionless form. First, the dimensionless variables are defined as follows:

$$\bar{u} = u/U_0, \quad \bar{v} = v/U_0, \quad \bar{w} = w/U_0,$$

$$\bar{x} = x/L, \quad \bar{y} = y/L, \quad \bar{z} = z/L,$$

$$\bar{t} = tU_0/L, \quad \bar{p} = p/\rho U_0^2,$$

$$\bar{\rho} = \rho/\rho_0, \quad \bar{\mu} = \mu/\mu_0$$

where the variables which have subscript 0 are the reference value, and L is the reference length. Thus, the dimensionless form of the Navier-Stokes equations are

$$\bar{\nabla} \cdot \bar{\mathbf{U}} = 0 \quad (3.3)$$

$$\bar{\rho} \frac{\partial \bar{\mathbf{U}}}{\partial \bar{t}} + \bar{\rho}(\bar{\mathbf{U}} \cdot \bar{\nabla})\bar{\mathbf{U}} = \frac{1}{\text{Re}} \bar{\nabla} \cdot (\bar{\mu}(\bar{\nabla}\bar{\mathbf{U}} + \bar{\nabla}\bar{\mathbf{U}}^T)) - \bar{\nabla}\bar{p} + \bar{\rho}\bar{\mathbf{f}} \quad (3.4)$$

where the last term $\bar{\rho}\bar{\mathbf{f}}$ ($\bar{\mathbf{f}} = \mathbf{f}L/U_0^2$) can be considered as a general source term. The Reynolds number Re is $\rho_0 U_0 L / \mu_0$. The choice of the characteristic variables depends on the problem itself. But, the dimensionless equations could simplify the implementation of the software.

3.1.2 Numerical method for solving the incompressible Navier-Stokes equations

Basics of the projection method

Chorin [30, 31] has developed a practical numerical method based on a discrete form of the Hodge decomposition. This method is known as the projection method. The main idea is to calculate an intermediate velocity field and, then, project to divergence-free fields. The final velocity fields are recovered by the continuous equation.

Here, for clarity of the description, we simplify the equation (3.4) as follows:

$$\nabla \cdot \mathbf{U} = 0 \quad (3.5)$$

$$\frac{\partial \mathbf{U}}{\partial t} + \mathbf{A} = \mathbf{D} - \nabla p + \mathbf{f} \quad (3.6)$$

$$\mathbf{A} = (\mathbf{U} \cdot \nabla)\mathbf{U} \quad (3.7)$$

$$\mathbf{D} = \epsilon \Delta \mathbf{U} \quad (3.8)$$

where $\epsilon = 1/\text{Re}$. We assume that the density ρ and the viscosity μ are constants in the calculation region. Therefore, the dimensionless $\bar{\rho}$ and $\bar{\mu}$ are equal to 1. And, we drop the bar above variables for clarity.

The fractional time scheme can be expressed in an explicit form. The time derivative of the momentum equation is discretized by a forward explicit scheme. The equation (3.6) becomes

$$\frac{\mathbf{U}^{n+1} - \mathbf{U}^n}{\Delta t} + \mathbf{A}^n = \mathbf{D}^n - \nabla p^n + \mathbf{f}^n \quad (3.9)$$

The velocity at the end of the time step must be divergence free. Therefore,

$$\nabla \cdot \mathbf{U}^{n+1} = 0 \quad (3.10)$$

- Prediction step

The pressure term is dropped from the momentum equation. And, an intermediate velocity (\mathbf{U}^*) field is obtained.

$$\frac{\mathbf{U}^* - \mathbf{U}^n}{\Delta t} + \mathbf{A}^n = \mathbf{D}^n + \mathbf{f}^n \quad (3.11)$$

- Projection step
Find the pressure field coupled with velocity.

$$\nabla^2 p = \frac{1}{\Delta t} \nabla \cdot \mathbf{U}^* \quad (3.12)$$

- Correction step
Correct the velocity by adding the pressure gradient.

$$\mathbf{U}^{n+1} = \mathbf{U}^* - \Delta t \nabla p \quad (3.13)$$

This basic three steps projection method illustrated the main idea. But, this explicit method is only first-order accurate in time. It needs a restrictive time step to obtain acceptable accuracy. Kim and Moin [56] used the second-order-explicit Adams-Bashforth scheme for the convective terms and Crank-Nicolson for the viscous terms. Implicit treatment of the viscous terms eliminates the numerical viscous stability restriction. This method is second-order accuracy for the velocity. Further improvement of the projection method can be found in [15, 4, 24].

Projection method in the present study

The projection method in the solver is a classical time-fractional projection method [83]. The method is based on the works of Bell, Colella, and Glaz [15] and Bell and Marcus [16] and is known as the BCG method. This method is second-order in time for both velocity and pressure. The advection term is computed using a Godunov procedure. The viscous term is treated implicitly, the same for the Kim and Moin [56]'s method.

Equation (3.11) is rewritten as:

$$\frac{\mathbf{U}^* - \mathbf{U}^n}{\Delta t} + \mathbf{A}' = \mathbf{D}' - \nabla p^{n-1/2} + \mathbf{f}^n \quad (3.14)$$

where,

$$\begin{aligned} \mathbf{A}' &= [(\mathbf{U} \cdot \nabla) \mathbf{U}]^{n+1/2} \\ \mathbf{D}' &= \epsilon \Delta \left(\frac{\mathbf{U}^n + \mathbf{U}^*}{2} \right) \end{aligned}$$

The advection term \mathbf{A}' approximates at 1/2 time levels to obtain second-order in time by using an explicit predict-corrector scheme [4]. The scheme is stable for a CFL number smaller than 1. Note that a half level pressure term is used in equation (3.14). It is treated as a source term and only updated at the 1/2 time level. The viscous term is discretized by the Crank-Nicolson scheme.

Adaptive Mesh Refinement

The Gerris solver employs a Quadtree/Octree structure to adapt the mesh. The hierarchical structures are shown in Figure 3.1. The adaptation proceeds in two steps. Firstly, refine the

mesh by a user-defined criterion. Multiple criteria can be introduced, for example, the solid boundary, the vortex, the gradient temperature, etc. The mesh will be refined at a specific time step based on user's definition. Secondly, the solver will coarsen the mesh cells which do not satisfy the refinement criteria.

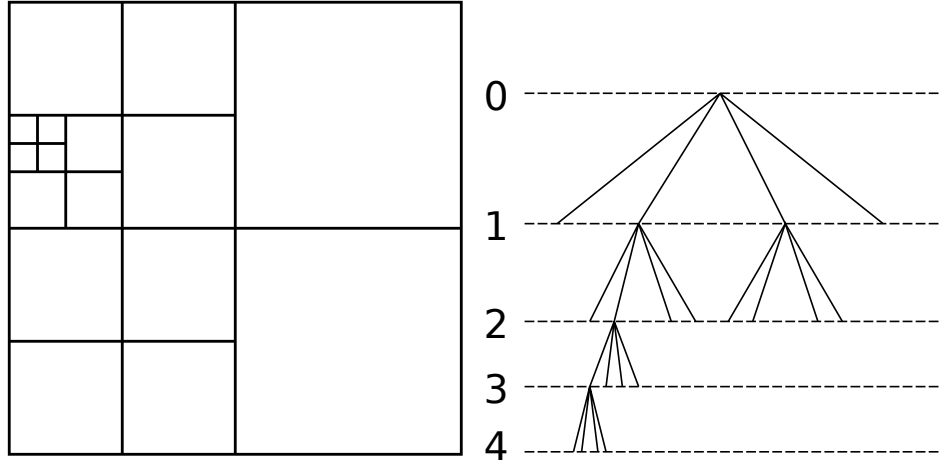


FIGURE 3.1: Example of quadtree mesh (left) and the corresponding tree-structure representation (right). [83]

The refinement procedure needs to interpolate values on the refined mesh. The values in children cells are calculated by a linear interpolation from their parent cell. The coarse procedure will take a mass-volumetric average from the children cells to the parent cells in order to maintain the local conservation. To simplify the calculations at cell boundaries between different level of the cells, Gerris introduces several constraints:

- The difference of level between direct-neighbor cells can not be bigger than 1;
- The difference of level between diagonal-neighbor cells can not be bigger than 1;
- All the cells directly neighboring a mixed cell must be at the same level;

The physical variables are collocated in the cell center. This type of arrangement is suitable for tree structure mesh. It is also simplifies the implementation of the Crank-Nicolson discretization of the viscous terms. The collocate mesh has a classical problem of decoupling between the pressure and velocity field. Gerris avoids this problem by carefully dealing with the projection step by using the approximate projection method [82].

First, the auxiliary velocity field \mathbf{u}_c^* is computed by equation (3.14). The auxiliary face velocity field \mathbf{u}_f^* is calculated by interpolating the cell center value to the face. If the face connects different levels of the cells, the face value is calculated by averaging the values from the refined faces. This process can guarantee the consistency of the corresponding volume fluxes. The divergence of the auxiliary velocity field is calculated by a finite-volume approximation.

$$\nabla \cdot \mathbf{u}^* = \frac{1}{V} \sum \mathbf{u}_f^* \cdot (a_f \mathbf{n}_f) \quad (3.15)$$

where V is the volume of the cell, \mathbf{n}_f is the unit normal vector to the face, a_f is the face area. After obtaining the auxiliary velocity field by the equation (3.15), the correction step is

applied to the face-centered auxiliary field. This procedure makes the velocity on the face-center divergence free. For the cell-centered velocity the correction step is given by:

$$\mathbf{u}_c^{n+1} = \mathbf{u}_c^* - |\Delta t \nabla_f p^{n+1/2}|_c \quad (3.16)$$

The operator $|\cdot|_c$ denotes the average over all the faces of the control volume. This procedure obtains a cell-center velocity field \mathbf{u}_c^{n+1} approximately divergence-free.

Volume-of-Fluid (VOF)

As we mentioned in Chapter 2, Gerris uses the Volume-of-Fluid (VOF) method to represent the interface. The basic notation is the same as described in Chapter 2. Here, we describe the method for advecting the volume fraction (c). Gerris adopted a geometrical approach to advect the c . This method is efficient and easy to implement for the Cartesian mesh. Since adaptation of the mesh is adopted in Gerris solver, a modified advection scheme to a quad/octree should be designed. As illustrated in Fig. 3.2, the total volume fraction in the left large cell will be advected to the right small cells. The flux will be calculated independently according to the size of the small cells. The volume fraction can be calculated as the area in the two dashed box in Fig. 3.2. The new c can be obtained in both coarse and refined cells. Next, new interfaces should be reconstructed in the cells. The method used in Gerris is the Mixed-Youngs-Centred (MYC) method [12]. As mentioned before, the method is one of the Piecewise Linear Interface Calculation (PLIC) methods.

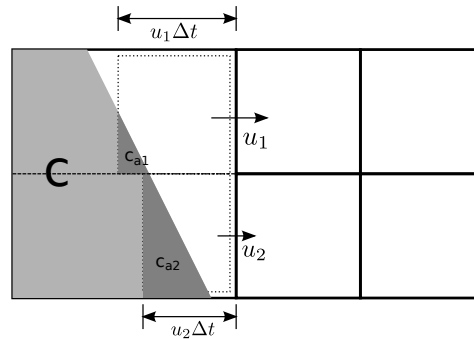


FIGURE 3.2: Geometrical flux computation on a quadtree mesh. [82]

Surface tension calculation

Accurately predicting the surface tension is one of the most difficult problems in numerical simulation. The surface tension term ($\sigma \kappa \delta_s \mathbf{n}$) can be added to equation (3.2) as an additional force.

In the context of VOF method, Brackbill, Kothe, and Zemach [22] proposed the following approximation:

$$\sigma \kappa \delta_s \mathbf{n} \approx \sigma \kappa \nabla c \quad (3.17)$$

) where $\kappa = \nabla \cdot \mathbf{n}$ is the surface curvature. σ is the surface tension coefficient. This approximation is called the *continuum-surface-force* (CSF). In order to recover exact discrete equilibrium

between surface tension and pressure gradient, the approximations of both gradients should be compatible. On the other hand, accurately estimating the curvature κ is also necessary.

The naive implementations of the CSF method can easily break the compatibility. Therefore, Gerris applies the surface tension force to the auxiliary face-center velocity field \mathbf{u}_f^*

$$\mathbf{u}_f^* = \mathbf{u}_f^* + \frac{\Delta t \sigma \kappa_f}{\rho(c_f)} \nabla_f c \quad (3.18)$$

The cell centered surface tension force to \mathbf{u} can be obtained in the same way as equation (3.16).

$$\mathbf{u}_c^* = \mathbf{u}_c^* + \left| \frac{\Delta t \sigma \kappa_f}{\rho(c_f)} \nabla_f c \right|_c \quad (3.19)$$

The subscript f indicates the face center value and c is the cell center value. The operator $||_c$ denotes the average over all the faces of the cell, which is the same as the one used for the pressure gradient in equation (3.16).

Height function

The height function method is used for estimating the curvature of an interface [32]. For example, the height function of a continuous line $f(x)$ can be define as:

$$H(x; h) = \frac{1}{h} \int_{x-h/2}^{x+h/2} f(x) dx \quad (3.20)$$

The normal vector and curvature can be written as

$$\mathbf{n} = \frac{1}{[1 + (H_x)^2]^{1/2}} (H_x, 1) \quad (3.21)$$

$$\kappa = -\nabla \cdot \mathbf{n} = \frac{H_{xx}}{[1 + (H_x)^2]^{3/2}} \quad (3.22)$$

A standard height function in 2D Cartesian grids is proposed by Cummins, Francois, and Kothe [32]. Firstly, choose a stencil centered on the cell where the curvature is needed to calculate. The size of the stencil usually 3×7 or 7×3 blocks in 2D. The orientation of the stencil should be aligned with the interface normal direction. Secondly, build the height function on each column of the stencil. The function could be $y = H(x)$ or $x = H(y)$, which depends on the orientation of the stencil. Finally, the curvature can be estimated from equation (3.22). Improvement of the method and generalization to the quad/octree mesh can be found in [82, 101].

Parallelization

Parallelization is important for the large-scale computational problem. The parallelization of Gerris is built on the MPI (Message Passing Interface) library. Gerris only allows *coarse-grain*

parallelism where the smallest parallel subdomain is an entire quad/octree. The whole calculation domain consists of multiple quad/octrees. The distribution of the tree data structure have two cases:

The two neighboring trees are located on the same processor. The connection of the tree is matching the memory pointers. The memories are shared on the same processor. Therefore, all operations on the multiple trees can be treated as a single tree.

If the two neighboring trees located on different processors. Ghost layers are needed for transfer of information between the processors. The ghost layers nodes are defined independently and "stitched" on the trees, which are often used for defining the boundary conditions. In the parallel case, the ghost layer is considered as a parallel boundary condition which swaps the data through `MPI_Send` and `MPI_Recv` functions.

The details of the parallelization in Gerris are reported in [2]. We used Gerris on a cluster. The real performance needs to be tested and results will be present in the following sections.

3.2 Basic test cases

3.2.1 Error quantification

The relative error norms can be measured against suitable reference solutions. The three relative error norms are defined as:

$$\|e\|_1 = \frac{\sum_{i=0}^n |q_{i,ref} - q_i|}{\sum_{i=0}^n |q_{i,ref}|} \quad (3.23)$$

$$\|e\|_2 = \left(\frac{\sum_{i=0}^n |q_{i,ref} - q_i|^2}{\sum_{i=0}^n |q_{i,ref}|} \right)^{\frac{1}{2}} \quad (3.24)$$

$$\|e\|_\infty = \frac{\max |q_{i,ref} - q_i|}{\max |q_{i,ref}|} \quad (3.25)$$

where q_i is the temporal evolution of quantity q . The choice of the quantity q and the reference q_{ref} depends on each test case. Additionally, the rates of convergence (ROC) can be numerically calculated by considering the error $\|e\|^h$, obtained with grid spacing h , and $\|e\|^{h/2}$ at finer grid. It can be calculated as

$$ROC = \frac{\ln(\|e\|^h / \|e\|^{h/2})}{\ln(h/(h/2))} \quad (3.26)$$

3.2.2 Lid-driven cavity

The lid-driven cavity is a classical fluid dynamics problem which has been investigated by many researchers. Pioneer works [43, 93] presented results of the steady state solutions, which are often taken as benchmark solutions for the numerical solvers.

The problem is described as the solution of the unsteady incompressible Navier-Stokes equations in a unit square $\Omega = (-0.5, 0.5) \times (-0.5, 0.5)$ (Fig. 3.3). Only the velocity u on top boundary Γ_3 equals to 1. The other velocity boundaries are Dirichlet boundary conditions

and equal to 0. The initial velocities and pressure fields are equal to 0. The flow will be driven by the lid as time advanced. Here, we consider that steady state is achieved when the difference of U ($=\|\mathbf{u}\|$) between the present step and 10 steps before is less than 1×10^{-5} . We take this test problem to verify the Gerris solver for the single phase flow.

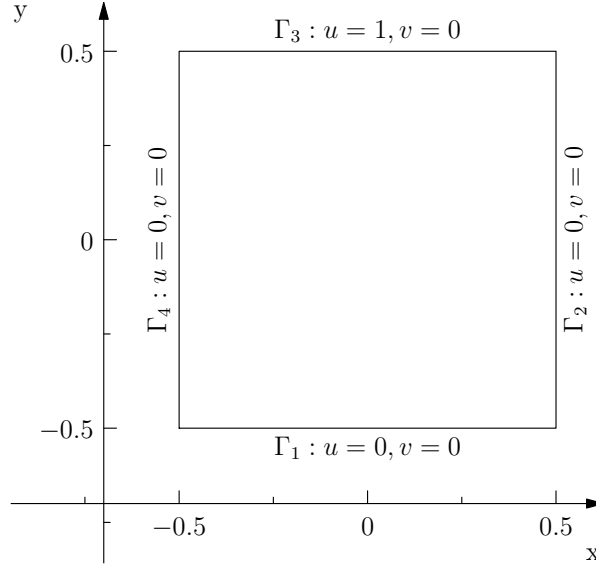


FIGURE 3.3: Boundary conditions of the lid-driven cavity problem.

Ghia, Ghia, and Shin [43] presented the u -velocity along the vertical line through the geometric center of the cavity and the v -velocity along the horizontal line through the geometric center of the cavity. We choose two test cases ($Re = 100$, $Re = 1000$) comparing the results with those obtained with the Gerris solver in Fig. 3.5. The solver obtained results close to those presented in [43]. The velocity convergence rates are shown in Fig. 3.4. It is clear that the convergence rate on this problem is close to second-order, except on the finest grid. Furthermore, we investigated the convergence rates for the pressure field. Botella and Peyret [20] presented the pressure field at $Re = 1000$, Fig. 3.6. Figure 3.6(b) shows that the pressure convergence rate is also second-order. The solver can handle this test problem very well. Next, we will test the performance of this solver for two-phase flow problems.

3.2.3 Bubble rising in stagnant liquid

Benchmark test cases

This section describes the setup for the test cases for two-phase flow presented in [3] and [48].

The domain $\Omega = [0, 1] \times [0, 2]$ is filled with fluid 1 except for a circular bubble, which is occupied by fluid 2. The configuration of the domain is shown in Fig. 3.7. The bubble is centered at $(0.5, 0.5)$ with a radius of 0.25. The density of the bubble is smaller than that of the surrounding fluid ($\rho_2 < \rho_1$). The no-slip boundary condition ($\mathbf{u} = 0$) is imposed at the top and bottom boundaries, whereas the free slip condition is imposed on the vertical walls.

The fluid properties are shown in Table 3.1. The subscript "1" and "2" indicate the parameters for fluid 1 and 2, respectively.

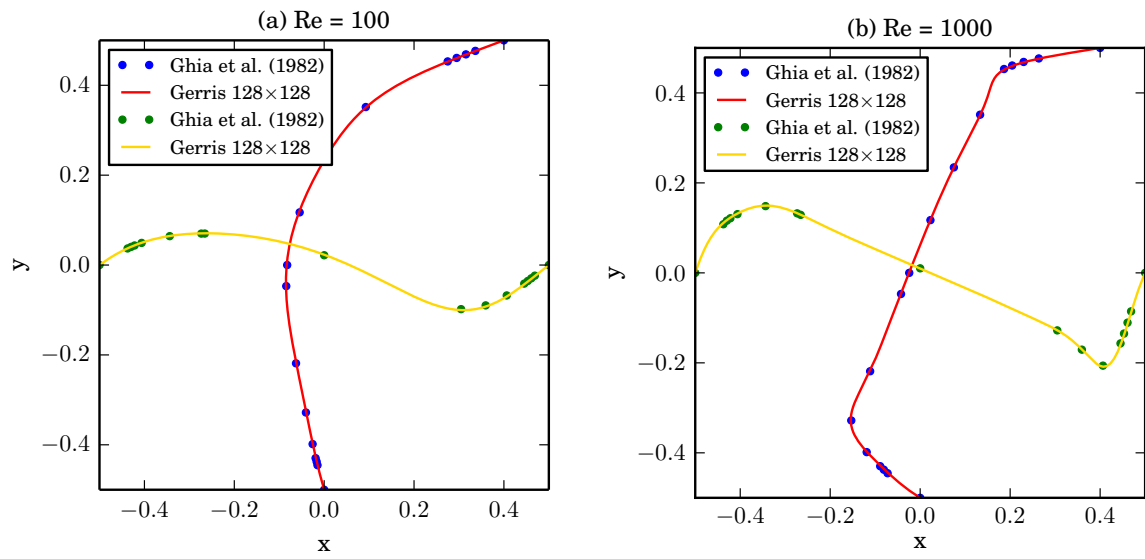


FIGURE 3.4: Velocity (u and v) comparison with the results in [43]. (a) $Re=100$, (b) $Re=1000$

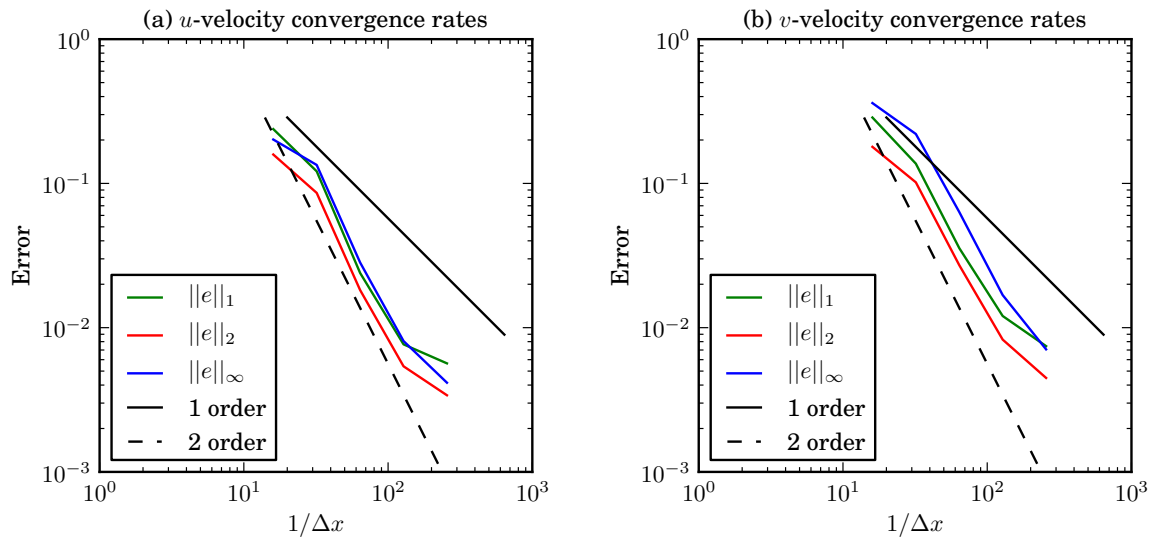


FIGURE 3.5: Convergence rates of (a) u -velocity and (b) v -velocity along the center of cavity.

TABLE 3.1: Physical parameters of the test cases

Test Case	ρ_1	ρ_2	μ_1	μ_2	g	σ	ρ_1/ρ_2	μ_1/μ_2
1	1000	100	10	1	0.98	24.5	10	10
2	1000	1	10	0.1	0.98	1.96	1000	100

Three benchmark quantities describe the temporal evolution of the bubbles. The quantities defined specially for the bubbles are:

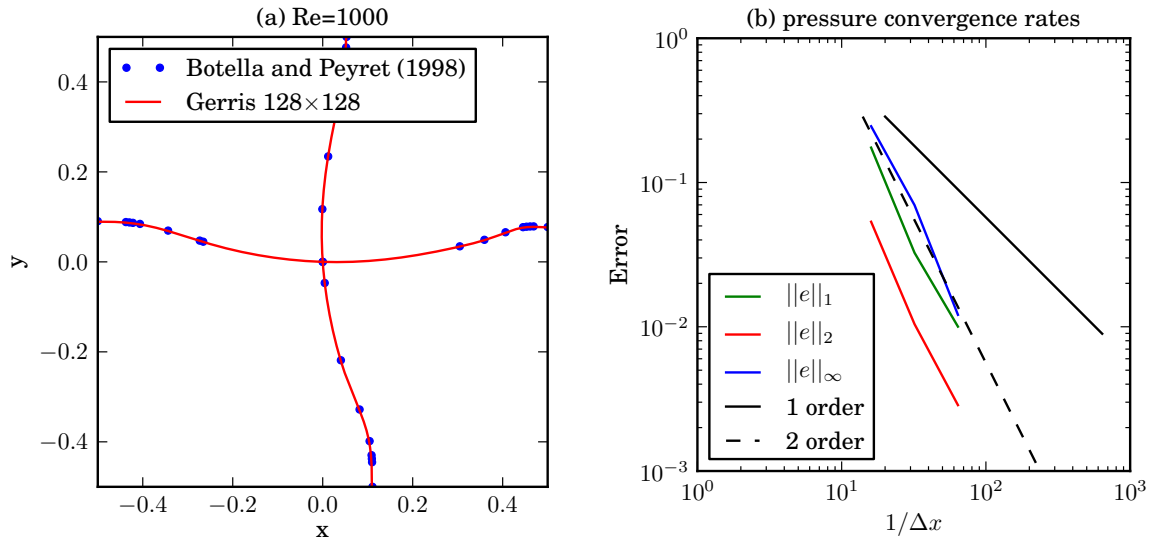


FIGURE 3.6: Pressure field along the center of cavity and its convergence rate.

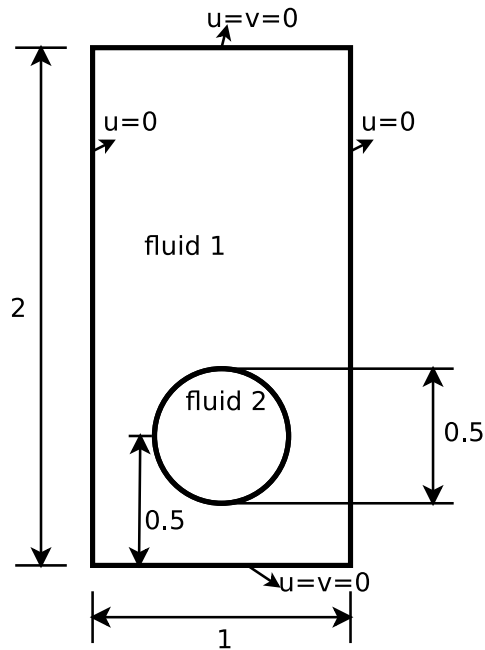


FIGURE 3.7: Initial configuration and boundary conditions for the test cases.

- *Point quantities:* Various points can be used for tracking the translation of bubbles. Commonly, the centroid (center of mass) is used, defined by

$$\mathbf{X}_c = (x_c, y_c) = \frac{\int_{\Omega_2} \mathbf{X} dx}{\int_{\Omega_2} 1 dx} \quad (3.27)$$

where Ω_2 denotes the region that the bubble occupies. The (x_c, y_c) is the coordinate of bubble centroid.

- *Circularity*:

$$\Phi = \frac{P_a}{P_b} = \frac{\text{perimeter of area-equivalent circle}}{\text{perimeter of bubble}} = \frac{\pi D_a}{P_b} \quad (3.28)$$

Here, P_b denotes the perimeter of a circle with diameter D_a , which has an area equal to that of a bubble with perimeter P_b . For a perfectly circular bubble, the circularity will be equal to 1.

- *Rise velocity*: The mean velocity of the bubble rising is a particularly important quantity, defined as

$$\mathbf{U}_c = (u_c, v_c) = \frac{\int_{\Omega_2} \mathbf{U} dx}{\int_{\Omega_2} 1 dx} \quad (3.29)$$

where Ω_2 denotes the region that the bubble occupies.

Results of the test case 1

Figure 3.8 shows the evolution of the bubble with time for the finest grid ($h = 1/256$). The bubble is initially circular. Then, it stretches horizontally. Finally, it evolves to a stable oval shape.

We first carry out mesh dependency tests. All computations were performed on uniform regular grids with cell sizes $h = 1/[16,32,64,128,256]$. At first, we show the bubble shape at $t = 3$ of different resolutions. Figure 3.9 shows that the final bubble shape is not changing too much with different meshes. The reconstructed segments from the VOF method are not connecting, in particular for the coarse mesh. Increasing the meshes resolution could remedy this problem. Merely from observing the bubble shapes, it is hard to tell the accuracy on each grid. We should use the previously defined benchmark quantities, equations (3.27), (3.28) and (3.29).

Figure 3.12 shows the center of mass evolving with time. There are no significant differences between the different grids. Figure 3.13 depicts the circularity of the bubbles. It is possible to observe some deviations on the coarsest grid ($h = 1/16$). The piecewise linear VOF can not represent curvature accurately on the coarse grid. As shown in Fig. 3.13, the circularity converges well on finer grids ($h < 1/128$). The time evolutions of rising velocity are shown in Fig. 3.14. The rise velocity reaches its maximum value then becomes stable. The rise velocity and the centroid converge well at different mesh resolution. These two quantities do not depict the bubble shape. Since the VOF method conserves the mass very well, the total quantity of the color function is the same at different resolutions. Therefore, the rise velocity and the centroid are not affected by the mesh resolution in this case.

Results of the test case 2

The simulation setup for case 2 is similar to case 1, except for the fluid properties. In test case 2, the decrease in surface tension causes the bubble to evolve to a non-convex shape with filaments. The bubble will form a skirt shape on the rear the bubble. Without experimental results, it is still unclear whether the bubble filaments would break off in this condition. In [3], the filaments become very thin, but they do not break off. In [48], the trailing filaments do

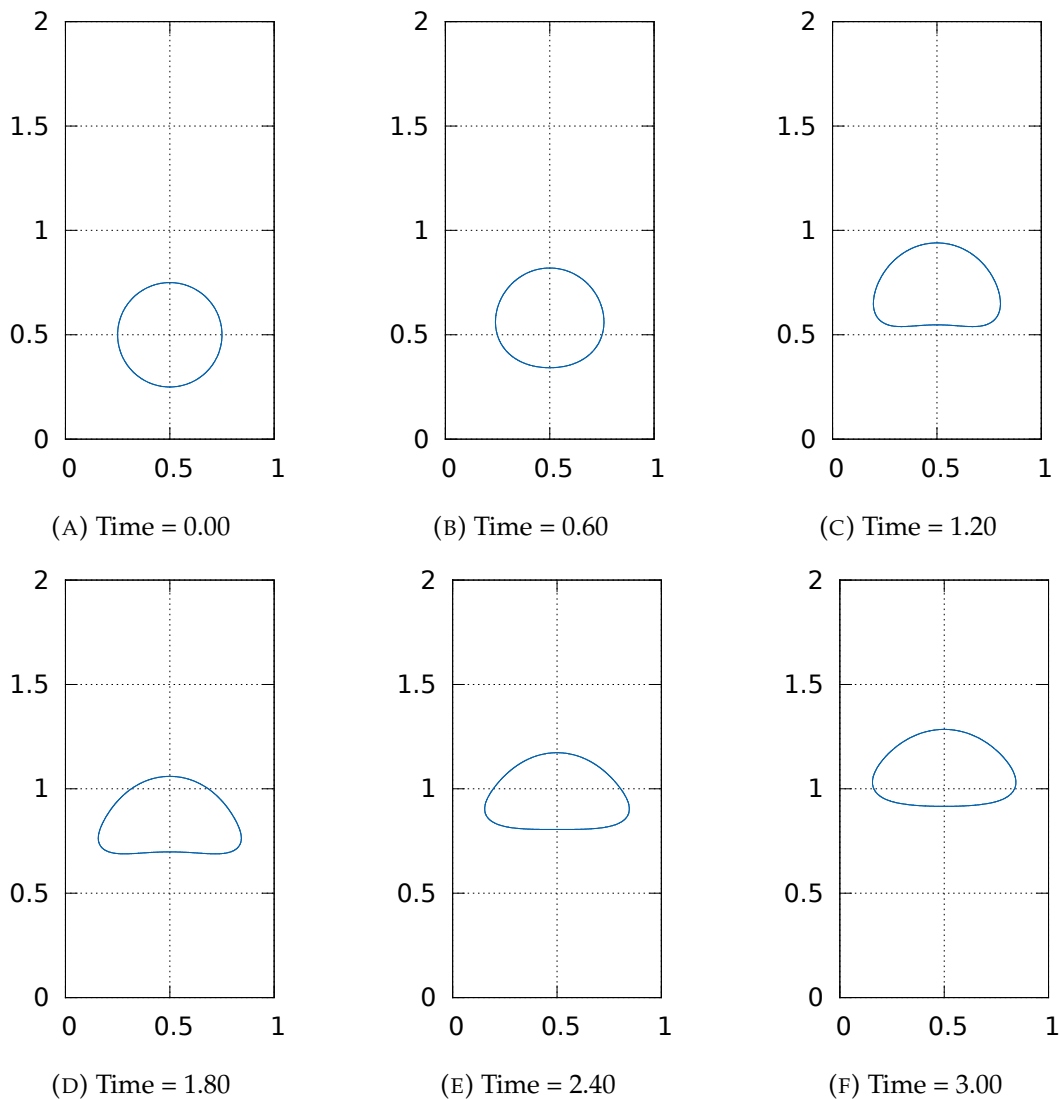


FIGURE 3.8: Time evolution of the interface for test case 1 on the finest grid.

not remain intact for two codes (TP2D and FreeLIFE) as our results presented here. Fig 3.10 shows the bubble evolving with the time. The filaments elongate at both sides of the bubble rear. Then, the filaments break off.

The center of mass for test case 2 is shown in Fig. 3.12. The position of the bubble at finer mesh ($h=1/256$) is higher than the others with coarse meshes. As shown in Fig. 3.11, more bubbles fluid with lower resolution is trapped into the tail filaments. The distribution of c affects the position of the center. Even though, the position of the bubble converges to the results with finer grids. In Fig. 3.13, the circularities at different resolutions do not converge to a constant value. The bubbles have their own shapes at different meshes, especially the tail shapes.

Figure 3.14 shows the rising velocity of the bubbles with different meshes. The velocities have slight fluctuations because of the formation of the tails. However, the velocity trend converges for higher resolutions.

We have compared the results obtained by Gerris with the data presented in [3] and [48].

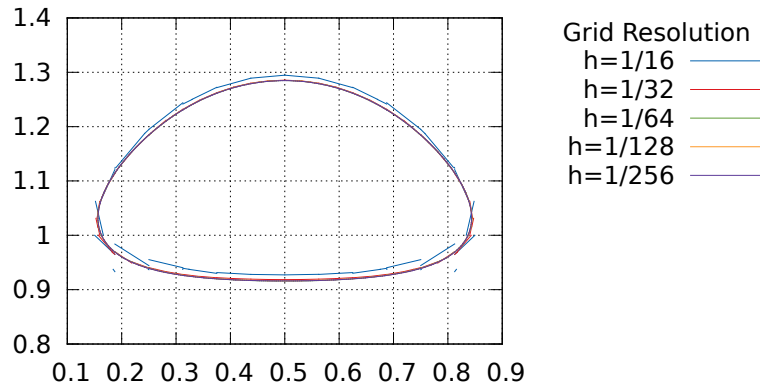


FIGURE 3.9: Test case 1 bubble shapes at $t = 3$. The shapes are computed on different grid resolutions.

The results show a good agreement with [3] for both test cases. The detailed comparison can be found in appendix A. The comparison shows that the errors are large for lower mesh resolutions. The different methods have different performances at lower mesh resolutions, whereas increasing the grid resolutions reduces the errors. The different methods converge to the same result at finer mesh.

To quantify the accuracy, we tested the errors at different meshes in terms of the center of mass, circularity and rising velocity. Since there is no analytical solution for these two test cases, we use the reference solution at finest grid resolution ($h=1/256$). The results are shown in appendix A. The ROC for this test is, in general, less than 2. The test 2 has lower converge order than the test case 1. The results show negative orders of convergence for circularity, which indicates that model does not yet converge to the reference solution.

Adaptive mesh tests

Adaptive mesh refinement (AMR) changes the accuracy of the solution in certain regions. Here, we use AMR to adapt the interface. In other words, the grid will be automatically refined to a certain level in the interface regions where the color function c is between 1 and 0. The bubbles with different adaptive levels are shown in Fig. 3.15. The adaptive mesh increases the local resolution.

Further comparison of the adaptive mesh and the uniform mesh are shown in Fig. 3.16. The comparison confirms that the adaptive mesh will reduce the accuracy, but the relative errors are in the acceptable range. Here, we compare the relative error of the center of the mass and rising velocity. Figure 3.16(A) shows the relative errors of the center of the mass between the uniform and adaptive mesh. For example, the results from adaptive mesh are obtained from a coarse mesh $h = 1/16$ and finest adaptive mesh $h = 1/64$ at bubble interface. The corresponding results on the uniform mesh are obtained with $h = 1/64$. We have tested the mesh resolution up to $h = 1/256$. The errors reduced with increasing the mesh resolution. Figure 3.16(B) are plotted in the same way. The relative errors of the center of mass are less

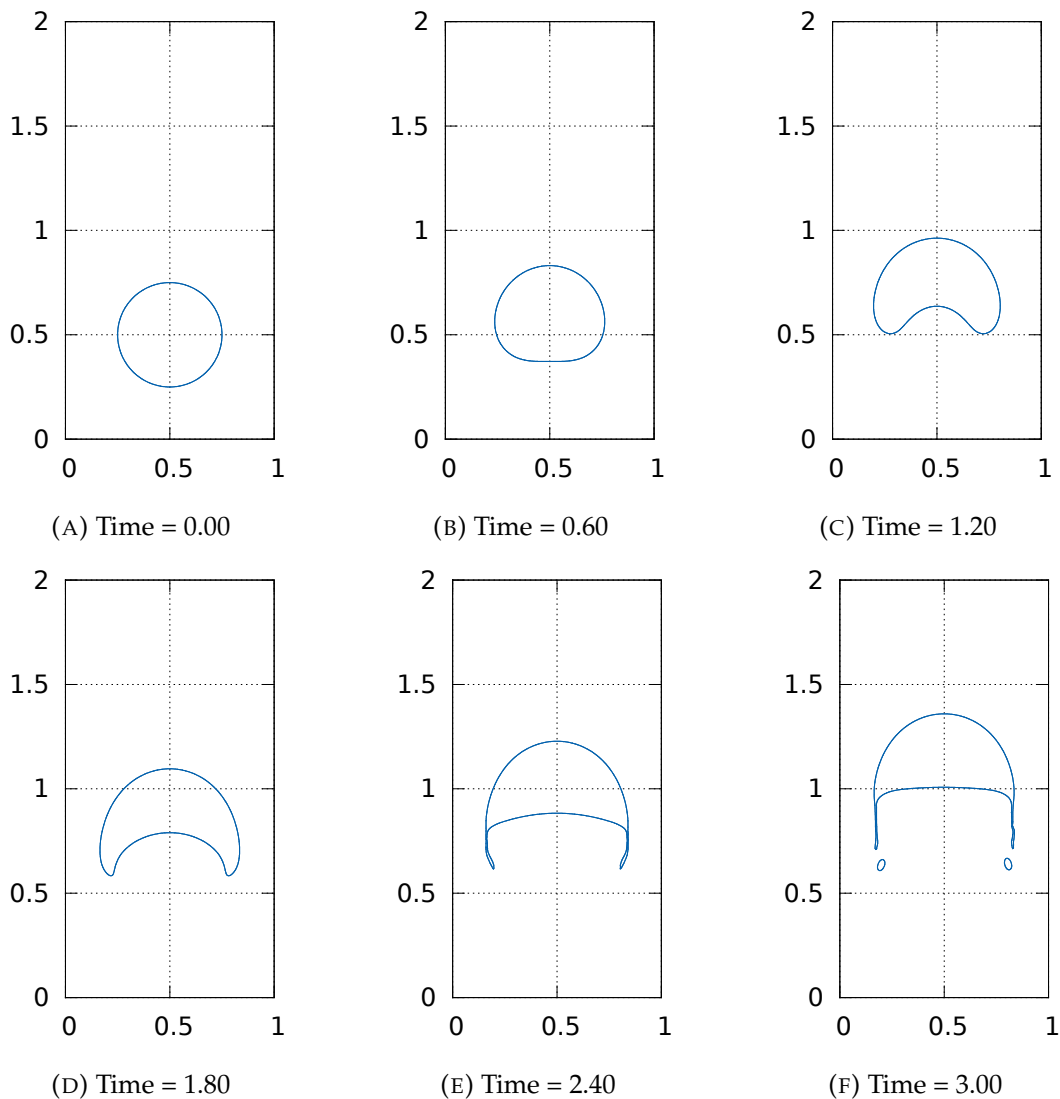


FIGURE 3.10: Time evolution of the interface for test case 2 on the finest grid.

than 1%. And, the relative errors of the bubble velocity are less than 6%. For the mesh with finest resolution $h = 1/256$, the errors reduced to less than 0.5% for the center of the mass and 3% for the bubble velocity.

The computational time is shown in Fig. 3.17. The adaptive mesh saves a lot of time of the calculation. For the mesh of $h = 1/128$, the calculation on the adaptive mesh is 10.4 times faster than the corresponding uniform mesh.

The conclusion can be drawn that the adaptive mesh introduces the calculation a small error, but it saves great amount of the calculation time.

Tests in Cylindrical coordinates

The test cases shown above are done on 2D Cartesian meshes which are not similar to the real bubble. Here, the configuration changes to cylindrical coordinates which is closer to real situations. The bubble has a spherical shape in the cylindrical coordinate configuration. The objective of this section is to simulate the bubble rising in the liquid. This is different from

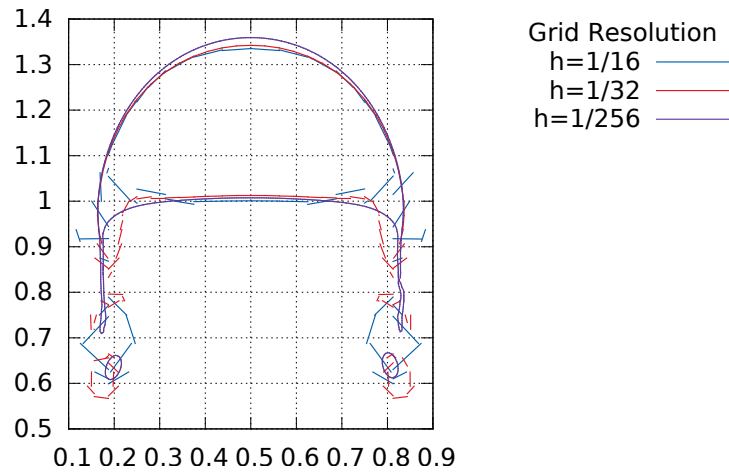


FIGURE 3.11: Test case 2 bubble shapes at time=3. The shapes are computed on different grid resolutions.

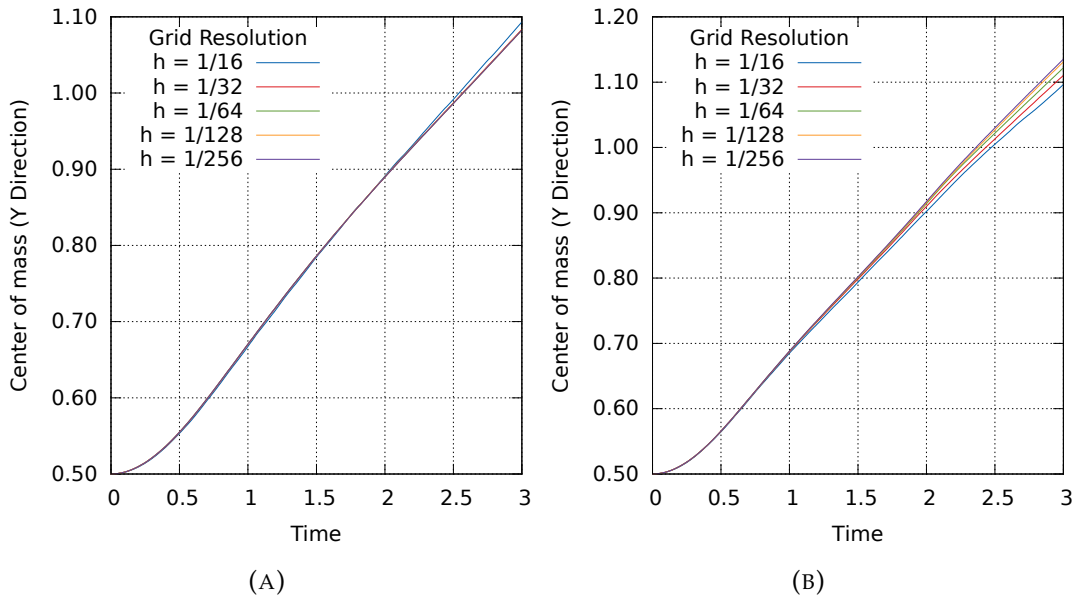


FIGURE 3.12: Center of mass for test case 1 (A) and 2 (B).

the test cases in previous sections which intends to validate with the benchmark solutions. In order to obtain the similar results, we adopted the same parameters presented in the literature for the benchmark tests.

The bubble initial configuration is similar to the previous case. The only difference is the vertical center line of the calculation domain is the rotational axis-symmetric boundary. The bubble is initialized as a sphere at $\mathbf{x} = (0, 0.5)$. The diameter of the bubble is 0.5. The width (L) of the calculation domain should be defined. The bubble is freely rising in the calculation domains and should not be affected by the side walls. The boundary condition on the side walls are slip-boundary conditions. The boundary condition of the u -component is $\frac{\partial u}{\partial x} = 0$. And, the boundary condition of the v -component is $v = 0$. Here, we carried out 3 tests for different widths of the calculation domains. Since the domains are axisymmetric, the

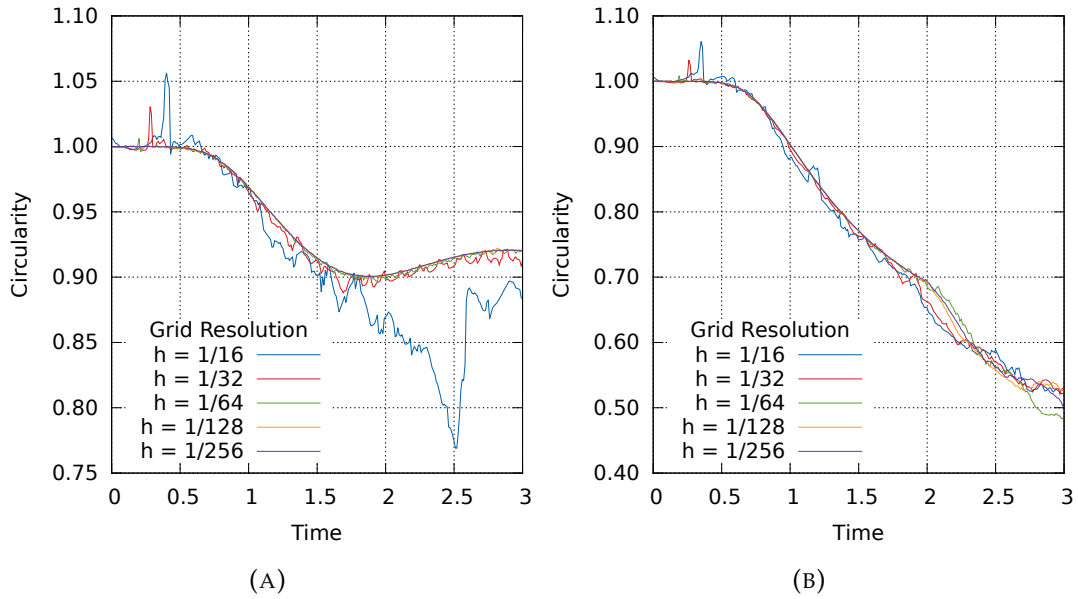


FIGURE 3.13: Circularity for test case 1 (A) and 2 (B).

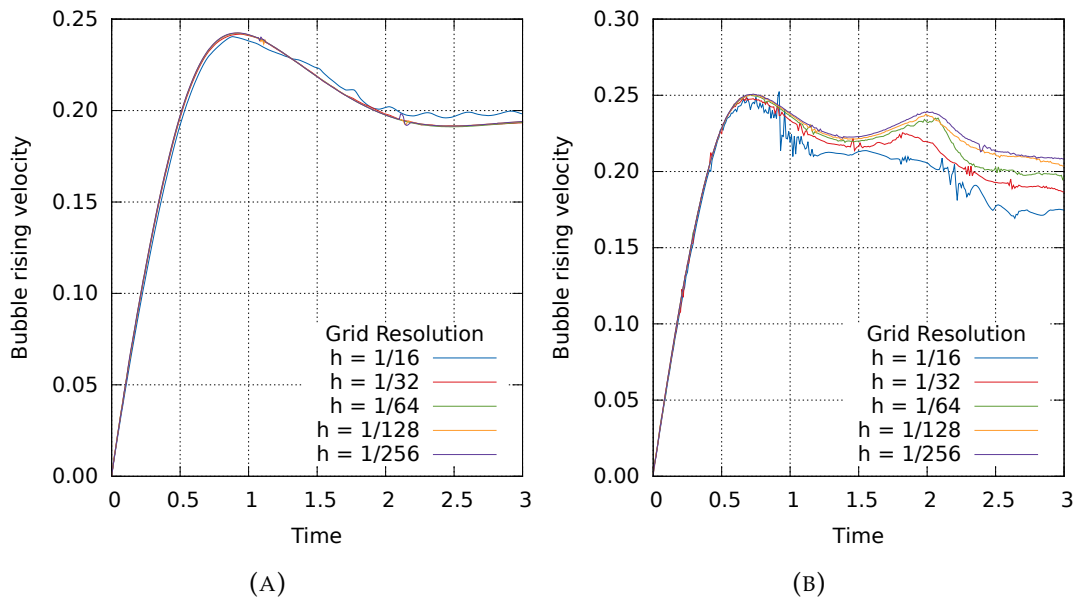


FIGURE 3.14: Rise velocity for test 1 (A) and 2 (B).

actual width of the calculation domains is only $L/2$. The tests performed in different domain widths, $L = 2D, 4D, 8D$. Figure 3.18(A) shows the bubble rising velocities. The domain width $L = 2D$ has strong effects on the bubble rising velocity. If the domain width increases to $4D$ or $8D$. The side wall effects on the bubbles are reduced. On the other hand, the bubbles in $4D$ and $8D$ have similar shapes. But, the bubble locations at $t = 5$ are slightly different, see Fig. 3.18(B). The reason is that the existence of the side wall will slow down the bubble. Considering the computational load and the accuracy, we chose $L = 4D$ as the calculation domain width for the bubble rising cases.

We have performed multiple tests to predict the bubble in a wide range of Reynolds and Bond numbers. The results are shown in Table 3.2. The definition of the Reynolds and Bond

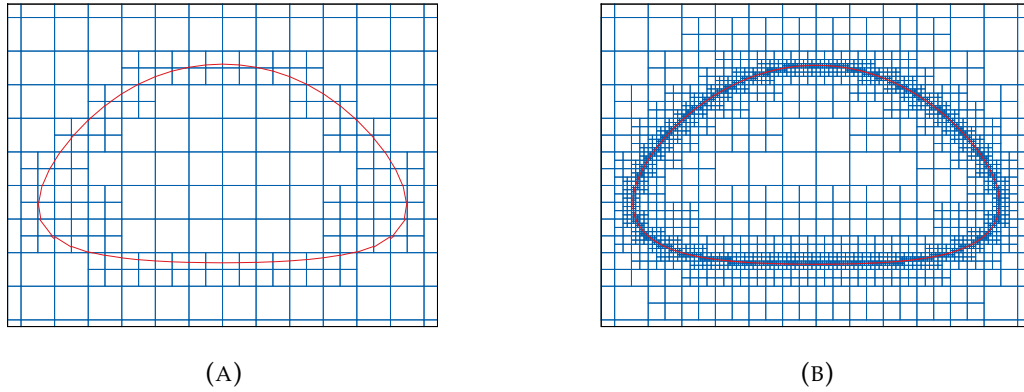


FIGURE 3.15: Adaptive mesh and interface of the bubble at $t = 3$ for test case 1. (A) The finest level of mesh equals to $1/32$. (B) Finest level of mesh equals to $1/256$.

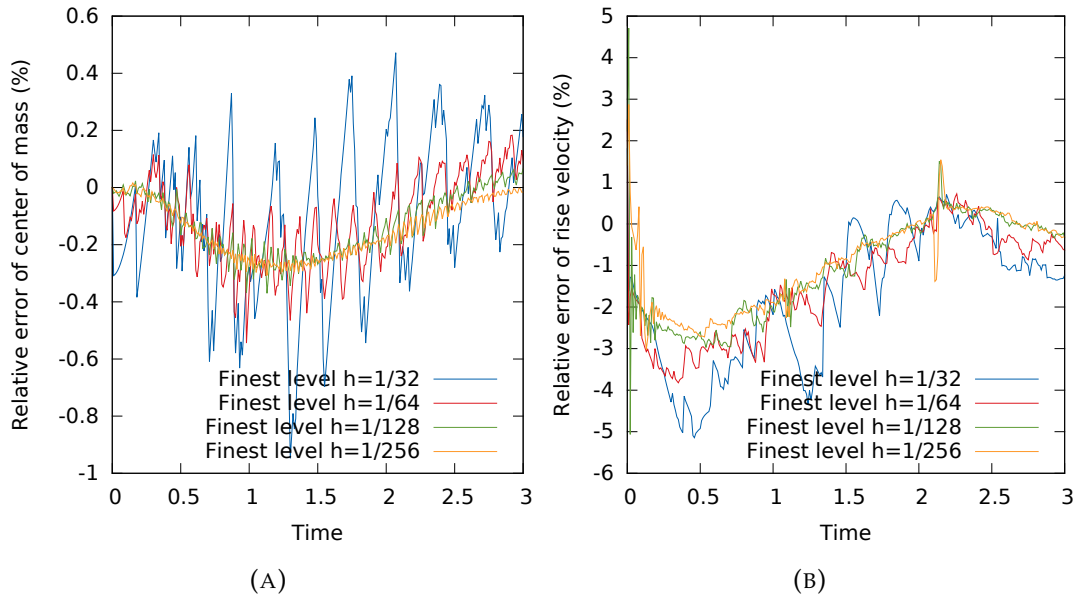


FIGURE 3.16: Relative errors of adaptive mesh with their corresponding results in uniform mesh for test case 1. (A) Relative error of the center of mass. (B) Relative error of the velocity.

numbers can be found in equation (2.1). The characteristic velocity U is not the terminal velocity of the bubble. Here, we take $U = \sqrt{gD}$ as the characteristic velocity simply since the terminal velocity is not known *a priori*. The D is the initial bubble diameter. Similar tests are carried out by Hua and Lou [47]. But, they used a different solver based on the front tracking method.

In the regimes of low Re and Bo numbers ($Re \approx 10$ or $Bo \approx 1$), the bubbles remain spherical. Slightly increasing the Re number ($Re \approx 20$), the bubble shape remains spherical for low Bo number. Whereas, the bubble bottom becomes flat and dimpled for higher Bo number ($Bo > 35$). For the regimes with higher Re number ($Re > 50$) and lower Bo number ($Bo < 50$), the bubble becomes elliptic/oblate ellipsoid shape. If further increasing the Re number ($Re > 100$), the elliptical-cap shapes can be observed. The results of [47] show that skirt bubbles

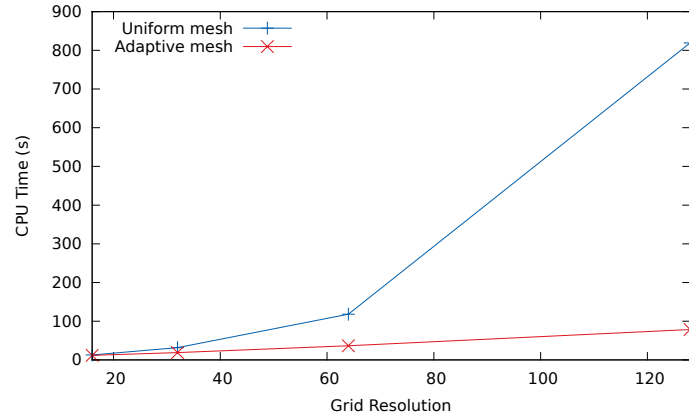


FIGURE 3.17: CPU times consume in uniform mesh and adaptive mesh for test case 2

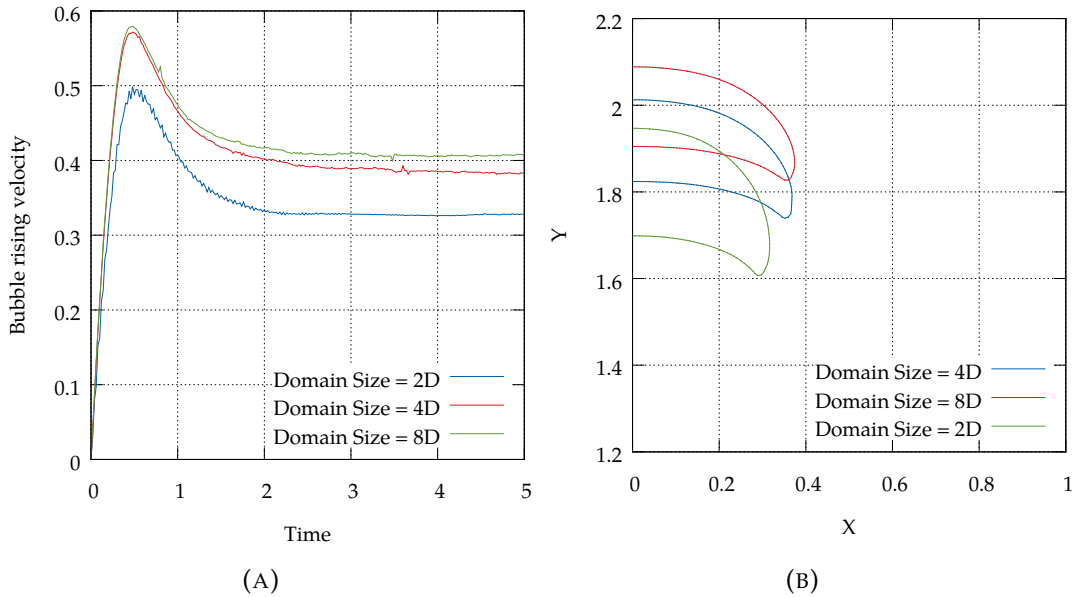


FIGURE 3.18: Sensitive analysis on the calculation domain width. ($Re = 35$, $Bo = 125$) (A) Bubble velocity. (B) Bubble shape at $t = 5$.

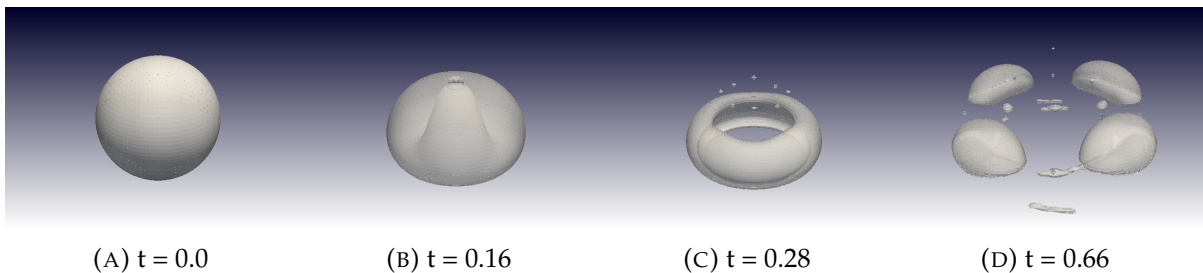
are formed at higher Re and Bo numbers ($50 < Re < 200$, $100 < Bo < 200$). Our simulation obtained the similar results at the early stage of the simulation ($t < 2$). The skirt of the bubble will eventually break up into smaller bubbles behind the leading bubble ($Re = 200$, $Bo = 50$). For $Re = 200$ and $Bo = 200$, the bubble breaks up soon after starting the simulation. There are no definitive shapes that can be obtained. Hence, the results are not shown in Table. 3.2. We will perform the simulation for the case ($Re = 200$ and $Bo = 200$) in 3D in the next section. We can conclude that the simulation can predict the bubble shapes in a wide range of flow regimes. However, for the highest Re and Bo numbers, the bubble shapes deviates to the results in [47].

TABLE 3.2: Prediction of the bubble shapes .

		1	5	10	Bo 35	50	100	125	200
Re	10								
	20								
	50								
	100								
	200								

3D tests

In the previous section, we have predicted the bubble shape in a wide range of Re and Bo numbers, but failed at large Re and Bo number. The reason is that the bubbles at large Re and Bo numbers does not deform in an axisymmetrical way. Here, we carry out a 3D simulation to test bubble rising at such condition. The Re and Bo numbers are both equal to 200. Similar to the previous definition, the bubble is initiated as a sphere in Fig. 3.19(A). The bottom quickly penetrates the bubble in middle (Fig. 3.19(B)). Then, a toroidal bubble can be observed in Fig. 3.19(C). This observation agrees with the results in [47]. But, the toroidal shape is only a transient shape. The toroidal ring breaks up and forms 4 offspring bubbles (Fig. 3.19(D)).

FIGURE 3.19: Bubble shape evolution with the time. ($Re = 200$, $Bo = 200$)

3.2.4 Parallelisation tests

We carried out the calculations on the computing center P2HPD hosted by the University of Lyon 1. We have used 7 nodes in the cluster. Each node has 16 CPU cores. The maximum CPU cores that can be used are 112 cores. Another calculation resource is the local workstation. It has 4 cores which are Intel Xeon(R) CPU E5-1607 v2 @ 3.00GHz.

The first test case is the 3D lid-driven cavity flow on the cluster. The test performance is shown in Fig. 3.20. There are three different uniform mesh sizes ($h = 1/32, 1/64, 1/128$). The

computing performance is increased on the cluster. Doubling the number of CPU nodes, the calculation could save almost half of the time.

However, we found that the calculation performance decreases when using the adaptive mesh. The parallel strategy limits the parallel subdomains of entire quad/octree [2]. Therefore, the elements on each CPU core are not the same. The data exchanged between different nodes are also not the same. A good calculation performance can not be obtained if too much data exchanges between the cluster nodes. The performance as shown in Fig. 3.20 will not be achieved. Usually, we could define the load balance ratio to indicate whether the computation loads are the same. It is written as:

$$r_b = (n_{\max} - n_{\min})/n_{\max} \quad (3.30)$$

where n_{\max} and n_{\min} are the maximum and minimum calculation elements on the node. If the elements are evenly distributed on each node, the balance ratio r_b will be zero. In practice, we should keep the balance ratio as small as possible.

We use the bubble rising case 1 to test the balance ratio. The AMR strategy is based on the VOF fraction. Here, we choose different finest meshes to maintain a good load balance ratio. The coarsest mesh is $h = 1/32$. The finest meshes are $h = 1/64$, $1/128$, $1/256$, $1/512$. Figure 3.21 shows the minimum, maximum and average elements on different cores. The level differences between the coarsest and finest mesh are 1 for Fig. 3.21(A), 4 for Fig. 3.21(B). The average balance ratios are 0.08 and 0.37. To optimize the computational speed, we choose the level difference between the coarsest and finest mesh less than 3.

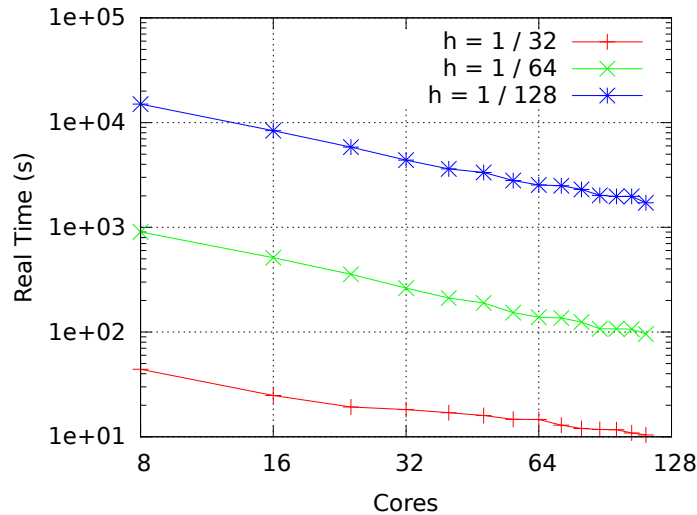


FIGURE 3.20: Real time spent with different number of CPU cores.

3.3 Chapter conclusion

The numerical solver has been tested with different one and two-phase flow problems. The Gerris solver is suitable for simulating the bubble flow. The following conclusions can be drawn:

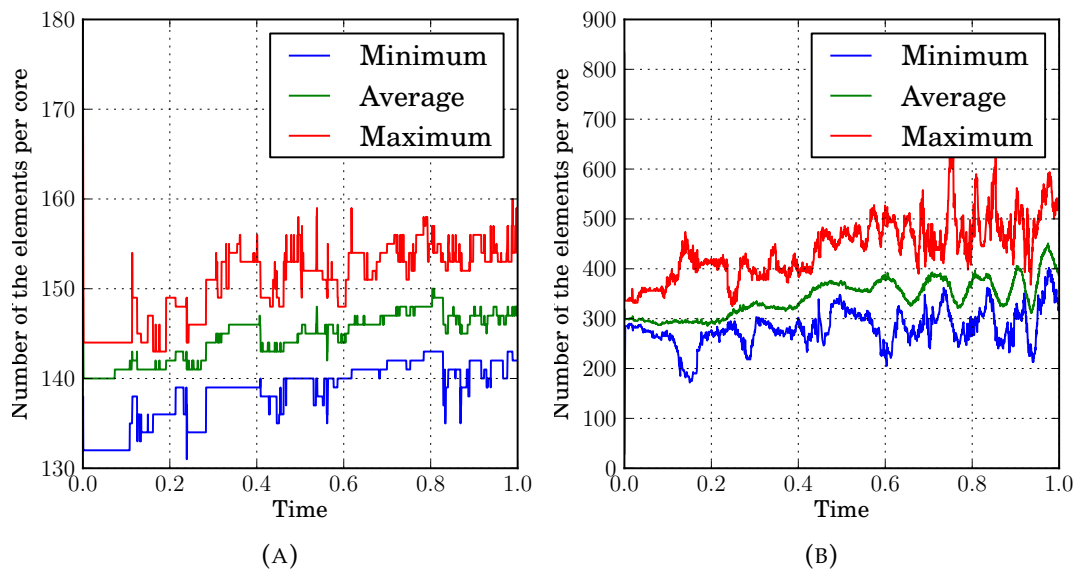


FIGURE 3.21: The maximum, minimum and average number elements on different CPU cores. Total number of the CPU cores is 16. Finest meshes are (A) $h = 1/64$, (B) $h = 1/512$.

- The Lid-driven cavity test validates the numerical solver for the single phase Navier-Stokes equations. The convergence rates are close to second-order both for velocities and pressure.
- The bubble rising test case validates the numerical solver for the bubble simulations. The results agree with the data in the literature. The solver can predict the bubble shape in a wide range of the Re and Bo number. Note that many other test and validation results concerning both single and two phase flow problems can be found on the Gerris website (gfs.sourceforge.net).
- The adaptive mesh refinement method improves the efficiency of the solver. This method saves much of computational time.
- The solver works well on the cluster. The parallelization tests show that performance may be reduced due to unequal distribution of the computational load for adaptive mesh.

Chapter 4

Description of the experiments

This chapter presents the methodology, structure and procedure of a series of experiments performed in the CETHIL laboratory, National Institute of Applied Sciences (INSA de Lyon). The experiments detailed in this chapter investigate the behavior of Taylor bubbles rising through a vertical cylindrical pipe encountering the changing diameters.

4.1 Description of the experimental test facility

The experimental apparatus consists of two main parts, the gas supply and the test section, shown in Fig. 4.1. In the present experiments, the gas is provided by compressed nitrogen. The high-pressure nitrogen is depressurized by a valve. The test section has two parts, the bubble generator chamber and the visualization box. The detailed structure will be showed in next section.

The test section is filled with liquid. The gas is injected at the bottom of the bubble generator chamber, see Fig. 4.1. Before entering the test section, the gas pressure is controlled by two valves, the depressure valve (Valve 1) on the nitrogen bottle and a micro-valve (Valve 2). The depressure valve is AIR LIQUIDE HBS 200-3-25. It can control the outlet pressure from 0.01 to 0.3 MPa. In the present experiments, the pressure is always maintained at 0.1 MPa. The micro-valve controls the gas flux. The bubble forms in the bubble generator chamber showing in Fig. 4.2. And then, the bubble goes to a long vertical pipe. The pipe is long enough to stabilize the bubble and make sure the bubble reaches the terminal velocity before encountering expansion or contraction. The length of the tube is 1.2 m. Then, the bubble rises into the visualization section which is shown in Fig. 4.3. The motion of the bubble is captured by a high-speed camera. Finally, the bubble reaches the liquid free surface and releases to the atmosphere.

The experimental test bench is suitable for visualizing bubbles in several kinds of transparent liquids. In the present study, we only tested the water and water-glycerol solutions.

4.1.1 Bubble generator chamber

The bubble generator chamber consists of a cylindrical chamber and a rotational cup which are shown in Fig. 4.2. Before injecting the liquid, the cup is turned upside down. Then, the gas is injected from the nozzle at the bottom of the chamber. The diameter of the nozzle is 4 mm. The bubbles generated from the nozzle are rather small. The rotating cup is used for

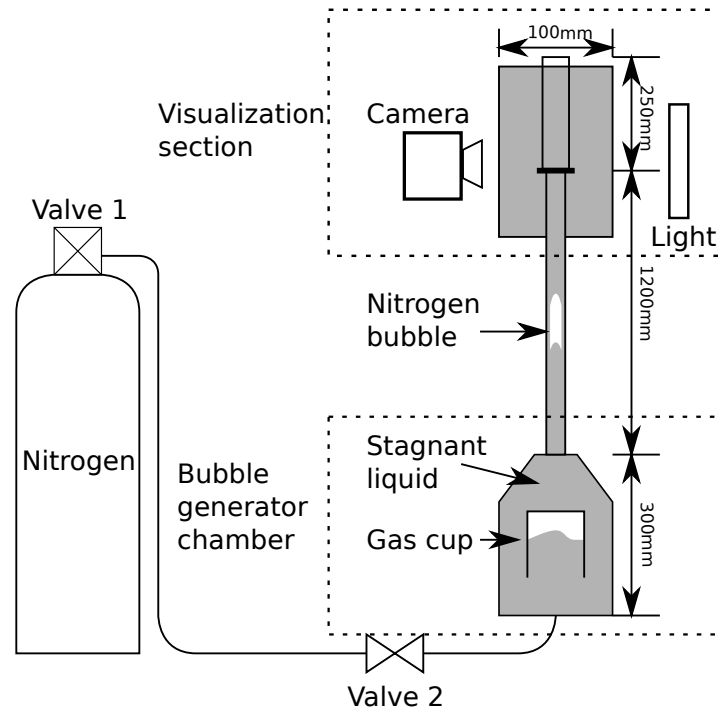


FIGURE 4.1: Configuration of the experimental test bench.

collecting the small gas bubbles. The bubbles agglomerate in the cup. When it is stable, the cup is rotated. The Taylor bubble will rise into the tube.

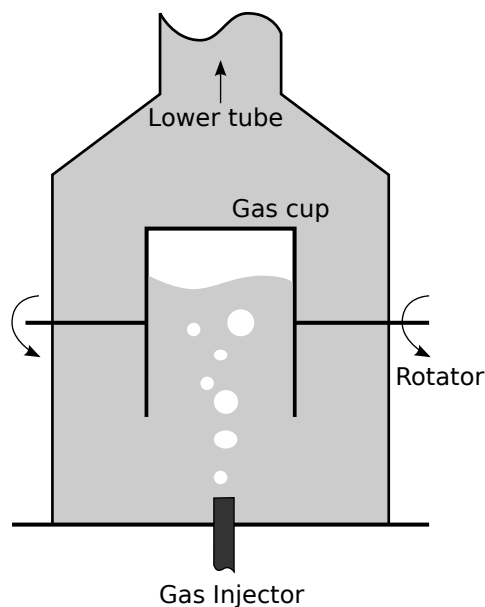


FIGURE 4.2: Illustration of the bubble generator chamber.

The purpose of the rotating cup is to stabilize the gas and gather the bubbles. Of course, small bubbles could agglomerate in the pipe and form a Taylor bubble. But, a longer pipe is then needed to stabilize the bubble. The rotating cup used for generating the large bubble allows us to reduce the pipe length for stabilizing the bubble. Secondly, the cup helps to control the volume of the bubbles. The gas quantity can be observed in the rotating cup. In

the present experiments, the bubble volume is less than 6000 mm^3 . The real bubble volume is measured by image analysis.

4.1.2 Visualization section

The schematic view of the visualization section is shown in Fig. 4.3. The visualization box is a transparent box which is used for reducing the optical distortion. The two pipes with different sizes are in the middle of the box. The lower pipe is fixed on the visualization box and connected to the bubble generator chamber. The upper pipe is fixed with the lower pipe by a thin plate. The camera is installed at the front of the visualization box. The light is installed at the back of the box.

The cross sectional size of the visualization box is $10 \times 10 \text{ cm}^2$. The height is 45 cm. The top side opens to the atmosphere. The bottom side is closed and has drainage outlet. The four side walls are made of plexiglass. The observation can be done in four directions. The sketch of the plate is shown in Fig. 4.4. The thickness of the plate is 2 mm and it is made of plexiglass. It adapts to the two tubes. The D_{out}^{lower} hole connects to the down tube. And, D_{out}^{upper} hole connects to the upper tube. The plate can be used for fixing the upper pipe. The depth of the notch is 1 mm, which prevents fluid exchange between the box and the tube. Note that sealing between the two pipes is weak. However, we use the same liquid in- and outside of the tube and the pressure difference is small. Therefore, the notch on the plate just eliminates the pressure disturbance induced by the bubble and seals the liquid in the tube to the liquid in the box. The plate also creates a sudden expansion/contraction between two tubes.

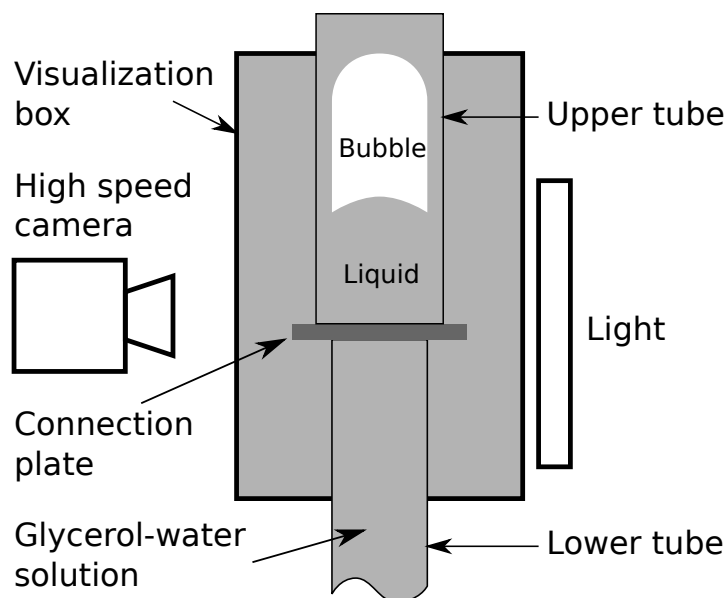


FIGURE 4.3: Illustration of the visualization section.

The camera was connected via an ethernet cable to a computer running the Photron video capture software to record the images. The software provides an interface which allows the user to control the resolution of the images, the frame rate and exposure of the video recordings. Relevant specification of the high-speed camera are shown in Table 4.1.

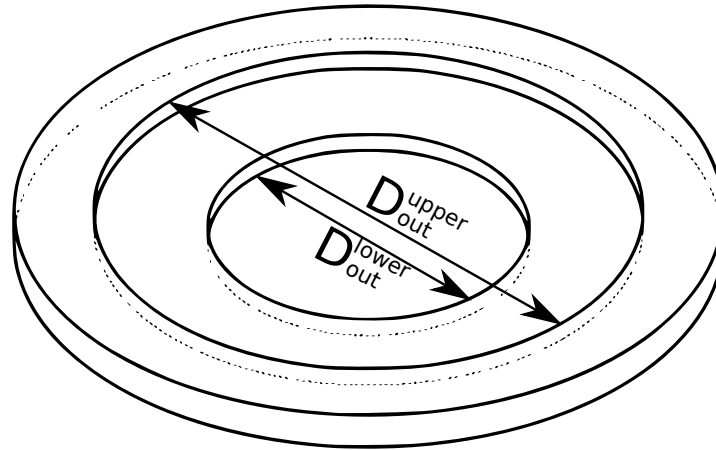


FIGURE 4.4: Sketch of the connection plate.

4.2 Experimental procedure

When the apparatus are tested leak-free, the experiments are ready to start. The procedures are shown as follows:

- Filling with the liquid: when the glycerol is filled into the tubes and visualization box, there are many small bubbles trapped in the liquid. They will block the view for observation. Therefore, we should wait for more than 3 hours before proceeding the experiments with glycerol. If the liquid is water, the small bubbles will release rapidly. In practice, 10 minutes is sufficient.
- Leveling the apparatus: the main objective is making the pipe vertical. We use the gradiometer to measure the long connection tube from various directions. And then, we slightly adjust the tube and make sure it is vertically positioned.
- Aligning the camera: the parameters of the camera are set up before the experiments according to Table 4.1. The alignment of the camera is to position the tube vertically in the middle of the image. The alignment is based on the image measuring tool in the Photron software.
- Visualizing the Taylor bubbles: the different bubbles were generated manually from the bubble generator chamber. We intend to visualize the bubble one by one. Therefore, the

TABLE 4.1: Camera related parameters.

Camera Type	FASTCAM SA3 model 120K-M2
Record Rate (fps)	1000
Shutter Speed (s)	3000
Total Frame (-)	5453
Image Width (pixel)	256
Image Height (pixel)	1024
Color Bit (-)	8

time interval between two rising bubbles are 5 minutes. We wait for the liquid in tube to be quiescent.

- Cleaning the apparatus after the experiments and preserving the glycerol in the bottle: this procedure prevents the glycerol from absorbing the water in the atmosphere.

4.3 Measurements and data acquisition

4.3.1 Uncertainty calculation

The uncertainty of the result of a measurements generally consists of several components. The components are regarded as random variables, and can be grouped into two categories according to the method used to estimate their numerical values:

- Type A: The uncertainty evaluated by statistical methods. The standard deviation of the mean of a series of independent observations is considered as the uncertainty. The quantity X_i is estimated from n independent observations. The mean value of the quantity X_i can be expressed as:

$$x_i = \bar{X}_i = \frac{1}{n} \sum_{k=1}^n X_{i,k} \quad (4.1)$$

and the standard uncertainty U_{xi} can be written as follows:

$$U_{xi} = \left(\frac{1}{n(n-1)} \sum_{k=1}^n (X_{i,k} - \bar{X}_i)^2 \right)^{1/2} \quad (4.2)$$

- Type B: The uncertainty estimates from other information. This could be information from past experience, from calibration certificates, manufacturer's specifications.

In most case, a quantity can not be measured directly, but is determined from other quantities. Here, we introduce the root-sum-square method to estimate the combining uncertainty from a series of independent variables' uncertainty [36]. The valuable U_y is an uncertainty of the valuable which depends on individual uncertainty U_{xi} in each independent variable x_i . The relation is expressed as:

$$U_y = \sqrt{\sum_{i=1}^N \left(\frac{\partial f}{\partial X_i} \cdot U_{xi} \right)^2} \quad (4.3)$$

where $y = f(x_1, x_2, \dots, x_N)$ and the variation in each independent variable is assumed to follow the Gaussian (Normal) distribution. The next sections will present the uncertainty of each independent variable. The uncertainty of a combined variable is calculated by equation 4.3.

TABLE 4.2: Diameter of the upper tubes.

Index	D_{out}^{upper} (mm)	D_{in}^{upper} (mm)	$\epsilon = D_{in}^{upper}/D_{in}^{lower}$
1	32.30	27.80	1.72
2	28.00	23.30	1.44
3	26.00	21.40	1.33
4	24.00	20.00	1.24
5	21.90	18.10	1.12
6	18.90	15.00	0.93
7	17.10	13.10	0.81
8	15.00	11.10	0.69

4.3.2 Tube diameter

The tube diameters have been measured with a vernier caliper with a resolution of ± 0.02 mm. The outside diameter is measured 10 times along the tube at random locations. The outside diameter is the average value from these measurements. The type A uncertainty can be obtained for the D_{out} . The value of tubes are listed in Table. 4.2. The maximum relative uncertainty is

$$\Delta D_{out}/D_{out} < 0.12\%$$

The inside diameter is measured at both ends of the tube. This uncertainty comes directly from the measurement instruments.

$$\Delta D_{in} = \pm 0.02$$

In the present study, the inside diameter of the lower tube is 16.40 mm, and the outside diameter is 19.90 mm. The upper tubes are connected to the lower tube. Their diameters are listed in Table. 4.2. D_{in} is the inside diameter of the lower tube. And, D_{out} refers to the outside diameter of the lower tube. ϵ is the inside diameter ratio of the upper tube over the lower tube, i.e., $\epsilon = D_{in}^{upper}/D_{in}^{lower}$.

4.3.3 Temperature

The K-type thermocouple measured the ambient temperature. The thermocouple has been calibrated. The uncertainty is ± 0.1 °C. The ambient temperature is 18 °C during the experimental tests. The temperature fluctuations during the experiment are

$$\Delta T = \pm 1.2^\circ\text{C} \quad (4.4)$$

4.3.4 Water-glycerol solutions

The original glycerol is 99.5 wt%, from which 5 different solutions were made by mixing mixed with the distilled water. The volume percentages are close to 95%, 90%, 80%, 70%, and 60%. The relative uncertainty of the volume percentages is $\pm 1.4\%$, i.e.,

$$\Delta \text{vol}\% = \pm 1.4\% \quad (4.5)$$

4.3.5 Viscosity measurement

The viscosity measurement is performed on a rheometer (Anton Paar MCR 302). The temperature for the test samples is set at 18°C. The test results are shown in Fig. 4.5. As can be seen in Fig. 4.5(A), the shear stress is linear with the shear rate. The water-glycerol solutions are thus considered as Newtonian fluids. The results are compared with the data in [11]. The viscosity of the original glycerol deviates from the data in [11]. Note that the glycerol has strong water absorption. During the experiments, the glycerol absorbed the water from the atmosphere. Therefore, the samples are taken after the experiments. The uncertainty of viscosity comes from the instrument and is written as:

$$\Delta\mu/\mu = \pm 1.5\% \quad (4.6)$$

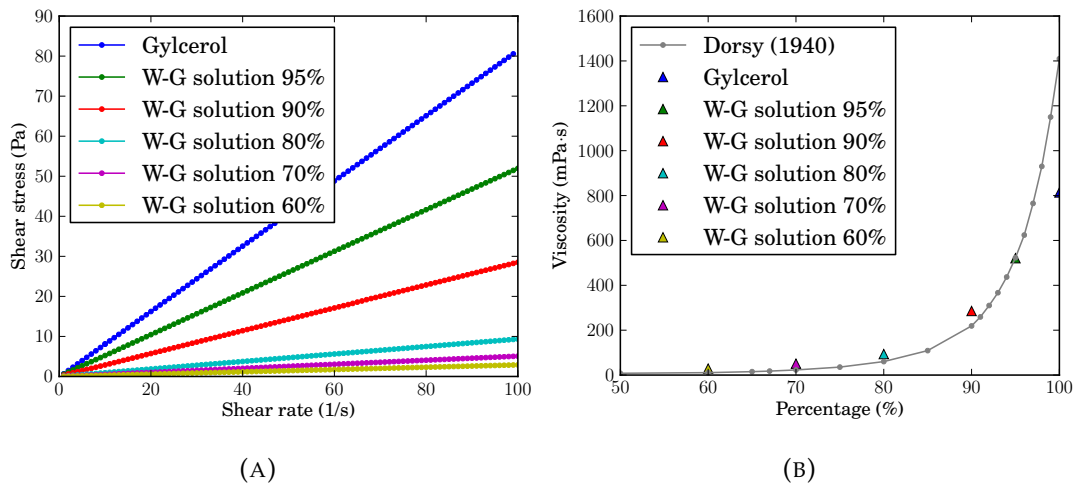


FIGURE 4.5: (A) Shear rate vs. shear stress of different water-glycerol solutions. (B) Measured viscosity of the water-glycerol solution as a function of the measured volume percentage of glycerol.

4.3.6 Density measurement

The density of the sample fluid is calculated from the volume and the weight. The volume is measured by the graduate bottle. Its uncertainty is ± 0.2 ml. The weight of the samples is measured by an electronic balance. The uncertainty is ± 0.05 g. The sample volume is 10 ml. Therefore, the relative uncertainty of the density is 2%, i.e.,

$$\Delta\rho/\rho = \pm 2\% \quad (4.7)$$

4.3.7 Fluid properties

The fluid properties are listed in Table 4.3. The surface tension of the water-glycerol solution is obtained from [11] using the volume fraction. Nitrogen is the gas phase in the present study. Its properties were calculated from the REFPROP software.

TABLE 4.3: Summary of the properties of the water-glycerol solutions.

Samples	Density ($\text{kg}\cdot\text{m}^{-3}$)	Viscosity ($\text{mPa}\cdot\text{s}$)	Surface tension ($\text{mN}\cdot\text{m}^{-1}$)
Water	996.56	0.853	71.2
Glycerol	1261.34	813.84	62.4
W-G solution 95%	1244.35	520.76	62.8
W-G solution 90%	1235.10	285.52	63.1
W-G solution 80%	1208.50	93.46	63.8
W-G solution 70%	1081.25	50.76	64.8
W-G solution 60%	1053.80	28.90	65.2
Nitrogen	1.1581	0.01747	

4.3.8 Image processing

The images are captured by a Photron high-speed camera. The image parameters are shown in Table 4.1. The original images have a resolution of 256×1024 pixels. We used a Python library to process the images. The library is called Pillow which is a fork of the Python Imaging Library (PIL). The process procedure is shown as follows:

- Importing the images into the program: in order to obtain a good contrast, we enhance the contrast of the images. In some of the test cases, the exposure is also increased in this procedure.
- Detecting the tube: the tube is vertically positioned on the image. We often choose only one image without the bubble to detect the tube position. First, we chose a sub-rectangle region on the image, which contains the tube. Then, the operations performed only in this sub-region. We obtain the gray scale gradients on the horizontal direction. The location of the maximum gradient is the tube wall. In fact, we could find two peaks of the grayscale gradient, which correspond to the inner and the outer tube wall. In the present study, we only detect the peak for the inner tube wall. The horizontal detections are performed at 10 locations along the vertical direction. As illustrated in Fig. 4.6(A). All the locations are fitted with a line equation. The slope of the line indicates the image tilt angle.
- Rotating the images: once we obtain the lines for the tube walls, the tilt angle is known. Then, all the images are rotated by the same angle. The rotational center is at the connection center of the two tubes (red dots in Fig. 4.6(B)). In practice, we aligned the tube vertically in the images. If the rotation angle is less than 0.055° , this procedure can be ignored.
- Removing the noises on the images: we cropped the images and left the part which is inside of the tube. There are still background noises around the bubble (Fig. 4.6(C)). Here, we do not use the method in Pillow library. The method, such as blurry, will smear the noise, but also blur the bubble interface. Our method is averaging the grayscale of 2×2 pixels to 1×1 pixel. The original image is reduced to the resolution of 128×512

pixels. Then, aforementioned gradient detection method is used on this resolution reduced image. The edge detections are only applied in the horizontal direction. The bubble interfaces are obtained on the low resolution images. Then, the region inside of the bubble projects back to the original image. The same edge detecting method is performed on the original image. This image only has the bubble part. Finally, the interface of the bubble can be obtained.

- Selecting the main bubble: there are still small bubbles and the connection plate in the images. Therefore, the original images are transferred to binary images. The potential bubble regions are set to 1, and the rest parts are set to 0. We design a traversing algorithm to detect the largest region (Fig. 4.6(D)). We consider that region is the Taylor bubble. The plate for connecting the pipe is also a dark region in the image. We examined multiple frames to find the dark regions which do not move with time. This region is considered to be the plate.

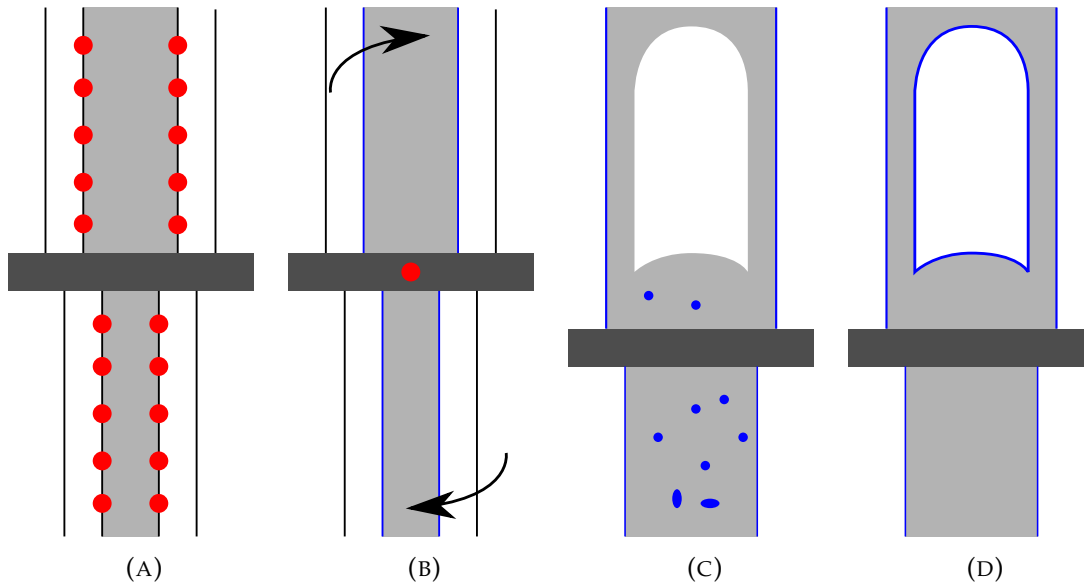


FIGURE 4.6: (A) Detecting the tube. (B) Rotating the image. (C) Removing the noises on the image. (D) Select the main bubble.

The uncertainty of the interface detection can be considered as the pixel distance from white to black. The interface is located between these two pixels. The average pixel distance in the present study is 7 pixels. Therefore, we consider that the uncertainty for the interface detection is ± 3.5 pixels. The real scale of the one pixel is less than 0.3 mm. Therefore, The uncertainty of the interface detection in millimeter is:

$$\Delta x < \pm 1.05 \text{mm} \quad (4.8)$$

4.3.9 Optical correction

The visualization box filled with liquid reduces the optical distortion. However, the refraction always exists due to the fact that tube wall and the liquid are not made of the same materials.

Here, we established analytical model to correct the optical refraction. The cross sectional

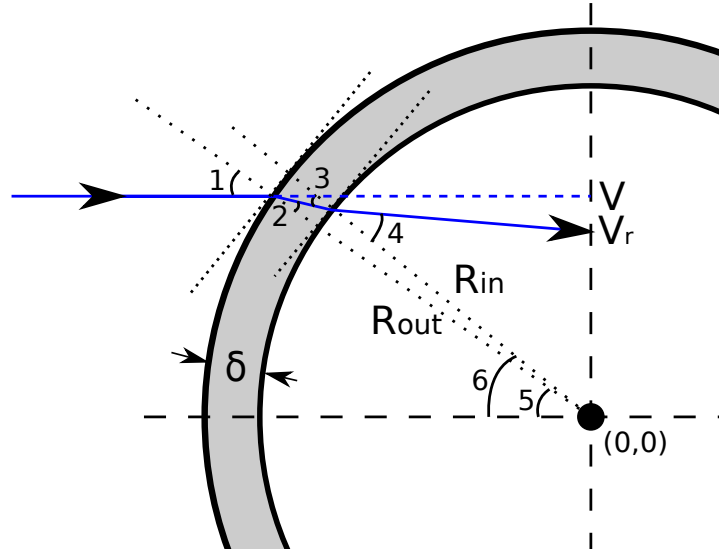


FIGURE 4.7: Illustration of the light refraction across tube wall.

view of the tube is shown in Figure 4.7. The coordinate original point locates at the center of the tube. The location of the bubble interface observed is at V . The real location is at V_r . This model considers the thickness of the tube wall ($\delta = R_{out} - R_{in}$). We assumed that the light outside of the tube is parallel. A simple relation of the angle of incidence can be obtained ($\theta_1 = \theta_5$):

$$\sin \theta_5 = \sin \theta_1 = \frac{V}{R_{out}} \quad (4.9)$$

According to Snell's law, for a given pair of media and a wave with a single frequency, the ratio of the sines of the angle of incidence θ_1 over the angle of refraction θ_2 is equivalent to the opposite ratio of the indices of refraction (n_2/n_1), i.e.,

$$\frac{\sin \theta_1}{\sin \theta_2} = \frac{n_{glass}}{n_{liquid}}$$

Then, we obtain the incidence angle (θ_3) for inner tube wall by

$$\frac{R_{in} \sin \theta}{\delta + R_{in} - R_{in} \cos \theta} = \tan \theta_2 \quad (4.10)$$

where, $\theta = \theta_6 - \theta_5$. R_{in} is the inner radius of the tube. And then, $\theta_3 = \theta + \theta_2$. The refraction angle θ_4 can be obtain by

$$\frac{\sin \theta_3}{\sin \theta_4} = \frac{n_{liquid}}{n_{glass}}$$

The optical distortion ΔV is thus:

$$\Delta V = V_r - V \quad (4.11)$$

$$= R_{out} \sin \theta_5 - R_{in} \sin \theta_6 + R_{in} \cos \theta_6 \tan(\theta_6 - \theta_4) \quad (4.12)$$

TABLE 4.4: The refraction index of glass and glycerol solution.

	Refractive Index (n)
Pyrex Glass	1.474
Glycerol	1.47339
W-G solution 95%	1.46597
W-G solution 90%	1.45839
W-G solution 80%	1.44290
W-G solution 70%	1.42789
W-G solution 60%	1.41299

In the present study, we obtain the refraction index data from [94] which are listed in Table. (4.4). Figure 4.8 shows that the optical distortion is large at positions close to the tube wall. The mixtures with lower glycerol percentage have larger optical distortion. However, the absolute distortion due to refraction on V is less than 0.064 mm, i.e.,

$$|\Delta V| = |V_r - V| < 0.064\text{mm} \quad (4.13)$$

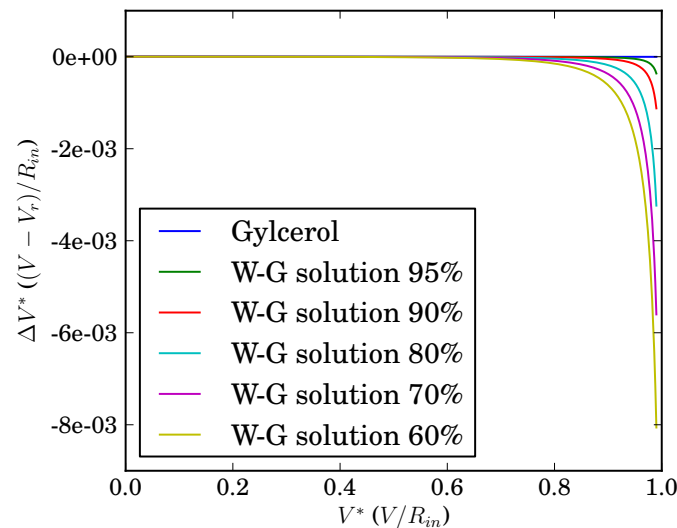


FIGURE 4.8: The optical correction along the radius.

4.3.10 Calculation of the bubble volume

The results obtained from the image processing are the points on the interface. These points should be connected to obtain the volume of the bubble. Figure 4.9 shows the points obtained from image processing. The points are separately distributed around the interface. Our method just detects the interface in the horizontal direction. The points can be separated into two groups, the points on the right (green) and the points on the left (blue). The first step is to sort the points from the bubble nose to the bottom. We randomly choose a virtual point inside of the bubble. This point can be set as the original point of a spherical coordinate.

Therefore, all points on the interface can be transformed to the spherical coordinate. Each point has its polar angle (θ).

Then, the points are connected from the bubble nose to the bottom. The results are shown in Fig. 4.9 (right). We set rotational axis located at the center of the bubble. The two interface lines rotate around the rotational axis to generate two halves of the bubble, see Fig. 4.10. This volume calculation method is applied to each frame. The bubble volume variations are shown in Fig. 4.10. For this particular case, we obtain an average volume equal to 2307 mm^3 . The volume will be used for the simulation. We observed that the bubble volume has great fluctuations from the 1500th to the 1690th frame. The inaccuracy is due to the fact that part of the bubble is blocked by the plate. For the blocked part, we simply use a straight line to approximate the bubble interface. Considering the inaccuracy of estimating the bubble interface, the uncertainty of the bubble volume can be shown as:

$$\Delta V_{\text{bubble}}/V_{\text{bubble}} < \pm 7.6\% \quad (4.14)$$

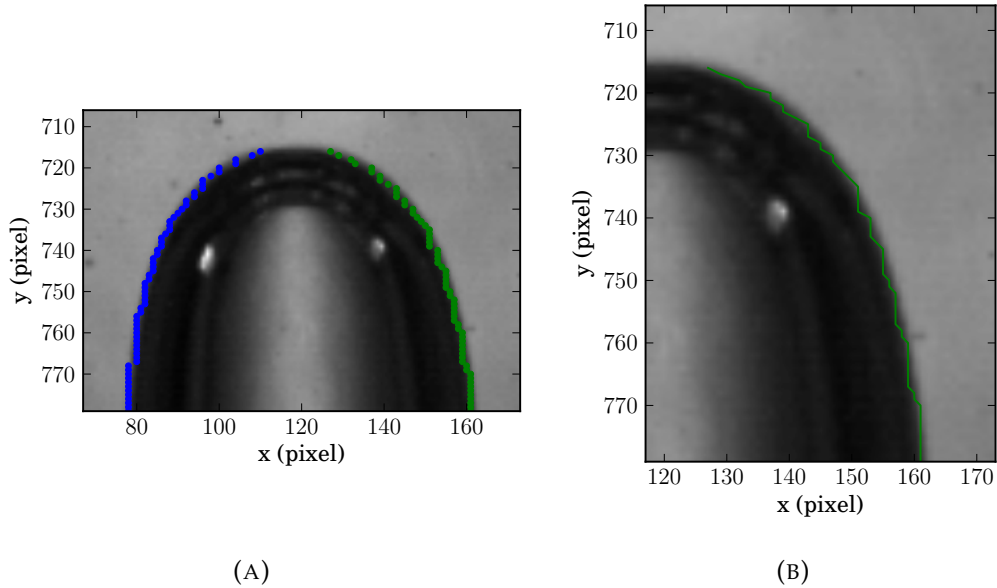


FIGURE 4.9: (A) The points indicate the surface. (B) Rearrangement and connection of the points.

4.3.11 Calculation of the bubble velocity

The first step of the calculation of the bubbles velocity is detecting the bubble location in each frame. The distance of displacement of the bubble in consecutive frames can be referred to Δs . The time interval (Δt) between each frame is fixed, which is $1/1000 \text{ s}$ in present study. The velocity of the bubble can be obtained by $U = \Delta s/\Delta t$. However, this simple method will lead to inaccurate results. A few restrictions should be added to obtain the bubble velocity:

- Defining the bubble location at the nose of the bubble. The bubble nose is the most stable part. It also has a sharp and clear edge on the raw images. Therefore, the displacement of the bubble nose is considered as the displacement of the bubble.

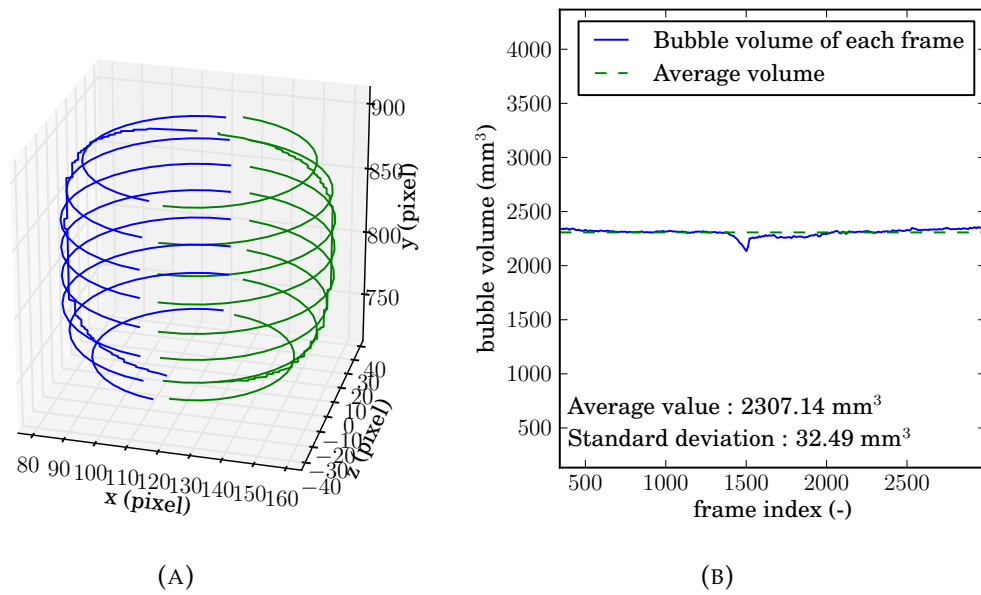


FIGURE 4.10: (A) The two halves of the bubble. (B) The results of the bubble volume in each frame.

- Increasing the time interval. In practice, the bubble displacement is very small in 1 ms, especially, for the bubbles in high viscous liquid. If the bubble movement is less than the uncertainty of the bubble interface detection, Δs is inaccurate. In present study, the bubble should move more than 7 pixels on the images, which can be considered as a validate displacement.

The uncertainty of estimating the bubble velocity are attributed to the uncertainty of the bubble interface detection, i.e.,

$$\Delta U_{\text{bubble}}/U_{\text{bubble}} < \pm 2.4\% \quad (4.15)$$

4.4 Summary of experimental data range

The main parameters for the experiments are shown in Table 4.5. The table shows the ranges of the experimental data. The precise values will be given in the next chapters.

TABLE 4.5: Summary of parameters in the experiments.

Fluids :	Water-glycerol solution, vol% = [95%,90%,80%,70%,60%]
Gas :	Nitrogen
D_{in}^{upper} (mm) :	15.00 to 32.30
D_{in}^{lower} (mm) :	16.40
ϵ :	0.69 to 1.72
Bubble volume (mm ³):	1322 to 6231
Bubble velocity (m/s):	0.026 to 0.161

4.5 Chapter conclusion

The experimental test bench has been successfully built up at the CETHIL laboratory. The test section can adapt to different ratios of the expansion and contraction. A high speed camera successfully capture the bubble motion through the singularity. The following conclusions can be drawn as follow:

- The experimental apparatus has been proved to be effective for the present study. The bubble motion can be captured in the test section.
- The glycerol solutions are made in the laboratory. The volume percentages have relatively large uncertainties. Whereas, the measurements of the properties of the solutions do not depend on the volume percentages. Therefore, the fluid properties can be obtained accurately.
- The self-designed post-processing algorithm can detect the bubble interface in the raw images. The bubble shape is then corrected by the optical correction algorithm. A similar method is also applied to the tube wall detection. Other data, such as bubble volume, bubble rising velocity, can be obtained.

Chapter 5

Bubble rising in straight tube

In this chapter, we present the results of the simulation of the bubble rising in a straight tube. The previous chapters have presented the numerical method and described the experimental setup. This chapter focuses on the Taylor bubble rising in the straight tube. The purpose is to validate the numerical model and also verify the experimental data.

The chapter will be presented as follows. First of all, a brief introduction about the configuration of the simulation model is shown. A parametric study of the model will be presented. Then, the simulation results will be compared to the experimental data from the test bench and also to those from the literature.

5.1 Model description

The simulation is performed on the cylindrical coordinates. The initial shape of the Taylor bubble is a rectangle body with a semi-circular nose (Fig. 5.1). The radius of the circle is r_0 . The distance from bubble bottom to the bottom of the calculation domain is $4r_0$. This distance minimizes the effects of the bottom on the bubble. r_0 is the initial bubble head radius which equals to $R - \lambda$, where λ is the film thickness which is calculated by equation (2.48). The film thickness is unknown before the simulation. The value can be set randomly. The final value will converge to a fixed value for a fixed group of parameters. In other words, the bubble terminal state is independent of the initial film thickness. We found that a good prediction of the film thickness will make the bubble reach the terminal state faster. Therefore, we use equation (2.48) to predict the film thickness. The length of the calculation domain size is L . Unless indicated otherwise, the domain length was given by $L = 8D$. This length was chosen to be sufficiently long so that the bubble could be fully developed [26]. And, the bubble initial length is l_0 . The boundary condition on the center is axi-symmetry. The upper and lower walls explicitly impose the Dirichlet condition ($u = 0, v = 0$). The side wall is also the no-slip boundary condition ($u = 0, v = 0$).

All the quantities are non-dimensional for the simulations. The characteristic length is the tube diameter (D). Therefore, all the lengths are normalized with respect to D . The characteristic velocity U_o is \sqrt{gD} . The definition of the dimensionless numbers are shown in equation (2.28). The continuous phase in the present case is the liquid phase. And, the disperse phase is the gas phase. The subscripts C and D in equation (2.28) change to l and g .

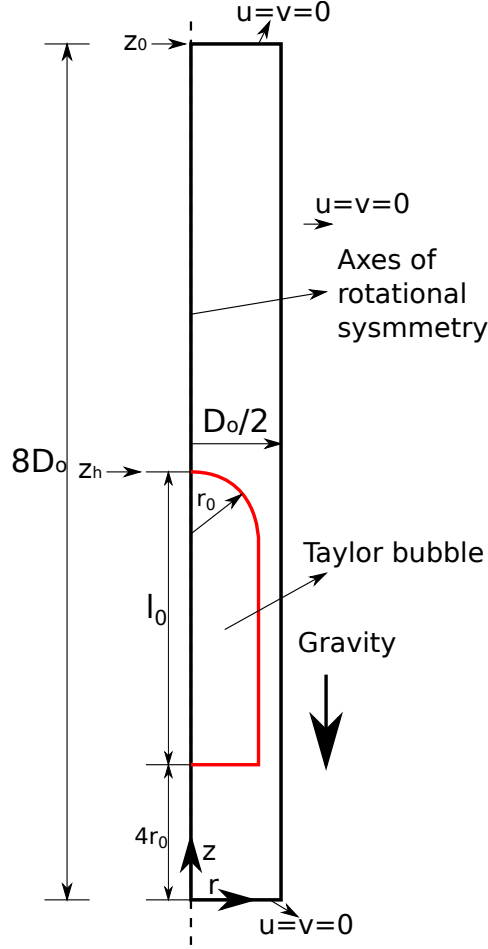


FIGURE 5.1: Initial configuration for the simulation.

The governing equations (3.4) can be written as

$$\bar{\nabla} \cdot \bar{\mathbf{U}} = 0 \quad (5.1)$$

$$\bar{\rho} \frac{\partial \bar{\mathbf{U}}}{\partial t} + \bar{\rho} (\bar{\mathbf{U}} \cdot \bar{\nabla}) \bar{\mathbf{U}} = \frac{1}{N_f} \bar{\nabla} \cdot (\bar{\mu} (\bar{\nabla} \bar{\mathbf{U}} + \bar{\nabla} \bar{\mathbf{U}}^T)) - \bar{\nabla} \bar{p} + \bar{\rho} \bar{\mathbf{g}} + \frac{1}{Eo} \kappa \delta_s \mathbf{n} \quad (5.2)$$

where N_f is the inverse viscosity number ($N_f = \frac{\rho_l \sqrt{g D^3}}{\mu_l}$), Eo is Eötvös number ($Eo = \frac{\rho_l g D^2}{\sigma}$). The only body force is the gravity. The \mathbf{g} indicates the direction of the gravity.

5.2 Sensitivity analysis

5.2.1 Mesh independency analysis

The adaptive mesh is applied in the present simulation. Chapter 3 has tested the performance of the AMR. The maximum level difference between the coarsest mesh and the finest meshes is 3. Here, we carried out 3 tests using the adaptive mesh. The parameters are shown in Table 5.1. The physical parameters are the same for 3 test cases ($Eo = 100$, $N_f = 100$). The initial bubble length is $4r_0$.

The results are shown in Fig. 5.2. We choose the bubble nose as the reference point. The bubble shape can be drawn in the same figure. The z_h is the location of the bubble nose. There are small differences of the bubble shape. For bubble nose shapes, it is difficult to observe the differences. Therefore, Fig. 5.2(A) shows the bubble tail shape. The M2 and M3 are almost the same. The bubble in M1 is slightly short than the others. A velocity profile comparison is shown in Fig. 5.2(B). The profiles are at $z^* = (z_h - z)/D = -1.54$. The average velocities can be obtained from the profiles. The M3 is the finest mesh. Therefore, the average velocity of M3 can be regarded as the reference value. The relative error of M1 and M2 is -7.4% and -1.8% respectively. Considering the computational time, we choose M2 for the other simulations.

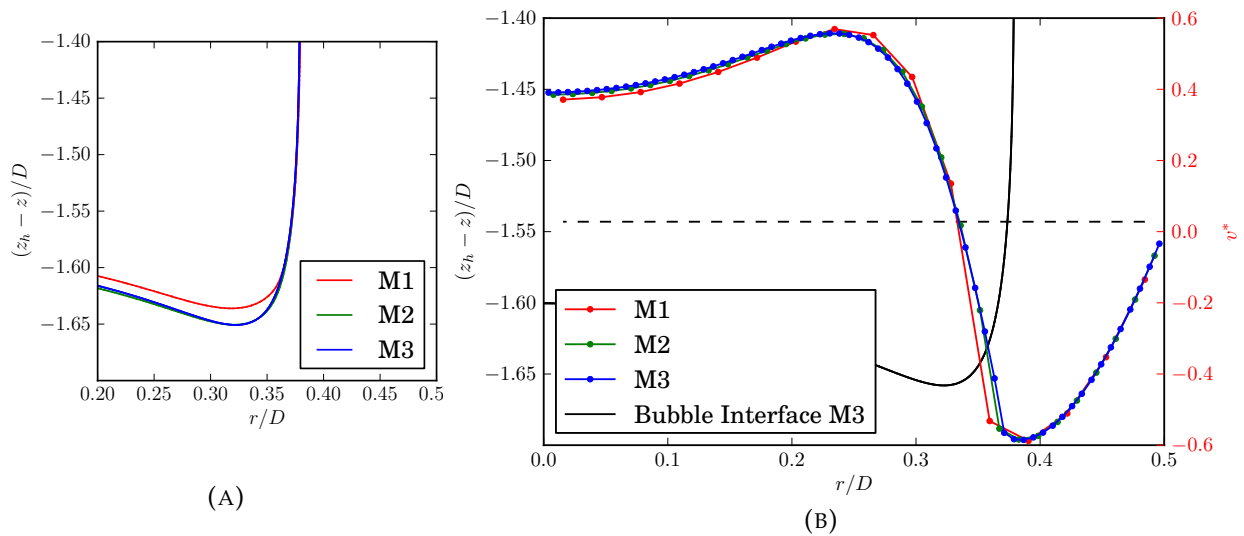


FIGURE 5.2: (A) Bubble tail shapes for different meshes. (B) Velocity profile in different meshes.

5.2.2 Effects of initial bubble lengths

The terminal velocity of the Taylor bubble is independent of the bubble length [118]. This conclusion is obtained from the experimental study. Here, we carried out 3 tests to confirm this conclusion. The physical parameters are the same for these 3 cases: $Eo = 100$, $N_f = 100$. The initial bubble lengths are $4r_0$, $5r_0$, and $6r_0$. The dimensionless bubble nose velocities are the same. The difference can be observed at the bubble tail (Fig. 5.3). The tail velocities oscillate and finally reach the steady state. The tail velocity of the longer bubble ($l_0 = 6$) takes longer time to stabilize. The initial film thicknesses for the 3 cases are the same. The bubble

TABLE 5.1: Mesh parameters.

Mesh	Coarsest	Finest
M1	R/16	R/128
M2	R/32	R/256
M3	R/64	R/512

evolves to a new shape according to the forces acting on it. And, interface waves develop from the nose of the bubble to its tail. The longer bubble has a long liquid film which takes more time to develop to the stable liquid film. Finally, the velocities converge to the terminal velocity. The observation on the bubble shapes shows that the nose, tail, and film thickness are the same.

The simulation results confirm that the initial bubble length only affects the transient behavior of the bubble. The initial bubble lengths dose not influence of the bubble terminal state.

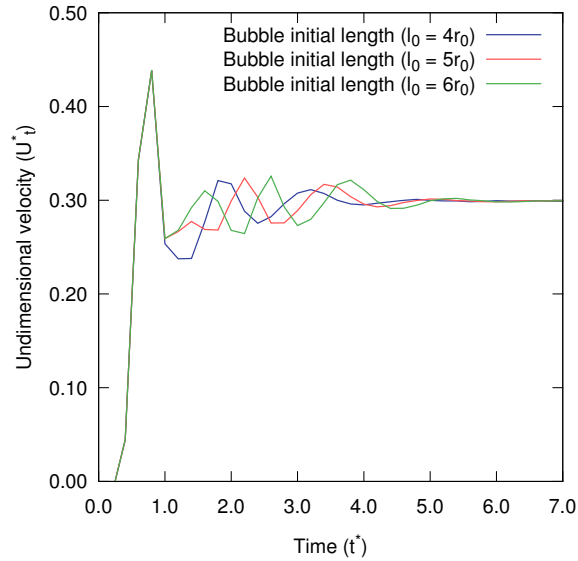


FIGURE 5.3: Tail velocities with different initial bubble lengths.

5.2.3 Effects of density ratios

The density difference creates the buoyancy force which is the driven force of the bubble rising. Here, we carried out a few simulations to test the effects of density ratios on the Taylor bubble. The density ratios range from 10 to 1000. In the 5 tests, other parameters such as viscosity ratio (r_μ), Eo number, and inverse viscosity number (N_f) remain the same, i.e. $r_\mu = 100$, $Eo = 50$, and $N_f = 59.4$. The terminal tail shapes are shown in Fig. 5.4(A). Decreasing the density ratio, the bubble tail becomes elliptic. The differences of the shape can hardly be observed if the density ratio is greater than 50. Figure 5.4(B) shows the terminal velocities at different density ratios. The terminal velocities decreases abruptly if the density ratio is less than 100.

The variations of velocities from the beginning of the simulation are shown in Fig 5.5. The bubble velocities oscillate at the beginning stage. In the present test case, the nose velocity becomes stable when t^* is greater than 6.5 (Fig 5.5(A)). And, the tail velocities need more time to become stable ($t^* > 9$) (Fig 5.5(B)). The tendency of the velocities development is independent of the density ratio.

The observation of the bubble shape concludes that the density ratio has a minimal effect on the bubble shape. The similar results are also found by Kang, Quan, and Lou [53]. The density ratios have strong effects on bubble terminal velocities, especially for cases where the density ratios are less than 100. We have tested the density ratio equals to 10000, but the bubble includes some unphysical filament. The large density jump between the two phases creates numerical oscillations and produces incorrect results.

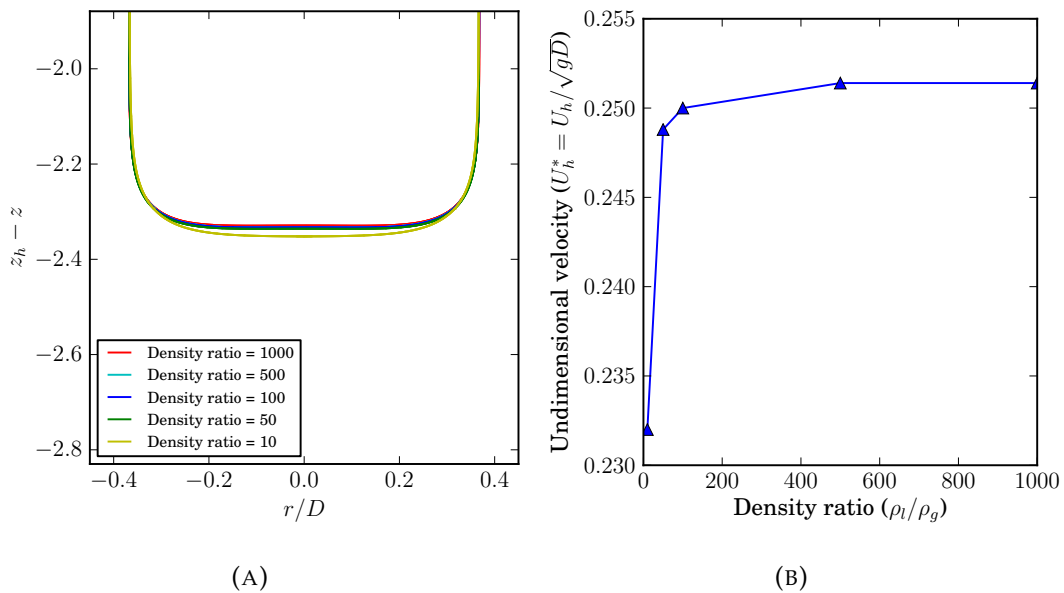


FIGURE 5.4: (A) Effect of density ratios on bubble tail shapes. (B) Effect of density ratios on the bubble terminal velocities.

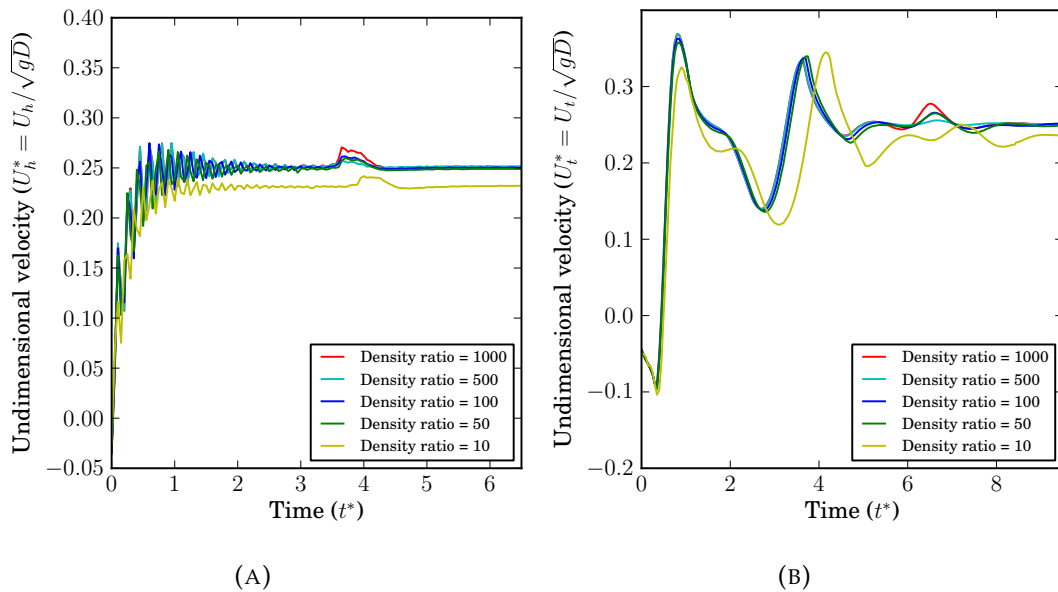


FIGURE 5.5: (A) Effect of density ratios on bubble nose velocities. (B) Effect of density ratios on bubble tail velocities.

5.2.4 Effects of viscosity ratios

The viscosity ratios (r_μ) ranges from 50 to 10000. 6 cases have been carried out for testing the effects of viscosity ratios. Other parameters remain the same, i.e. $r_\rho = 1000$, $Eo = 50$, and $N_f = 59.4$. The bubble shapes are shown in Fig. 5.6(A). There are no significant changes on the tail of bubbles as well as for the terminal velocities. They slightly increase with increasing the viscosity ratios (5.6(B)). Kang, Quan, and Lou [53] and Lu and Prosperetti [63] have found similar results. Kang, Quan, and Lou [53] found that the selected viscosity ratios lead to small variation in dimensionless numbers (Eo and N_f), which gives minimal effects on the bubble dynamics. In the present study, we keep the same Eo and N_f numbers for all the test cases. The only variable is the viscosity ratio. The results, both shapes and terminal velocities, appear to be very similar. Therefore, we can conclude that the viscosity ratio has minor effects of the bubble motion.

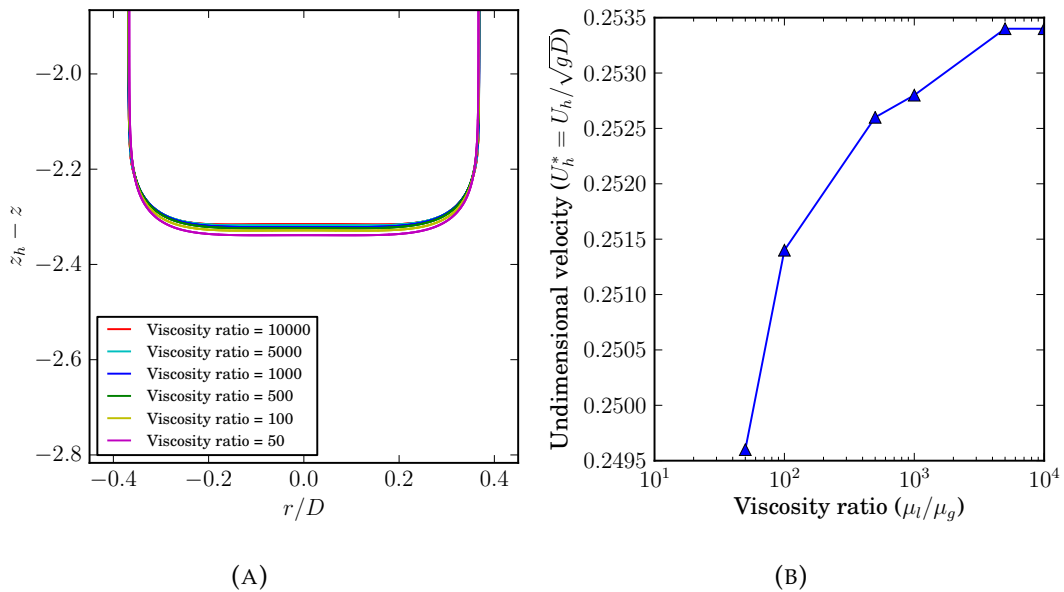


FIGURE 5.6: (A) Effect of viscosity ratios on bubble tail shapes. (B) Effect of viscosity ratios on the bubble terminal velocities.

5.2.5 Effects of Eo number

As written in equation (2.28), the Eötvös number ($Eo = \rho_l g D^2 / \sigma$) is the combination of the buoyancy force and the surface tension force. Increasing the Eo number, the surface tension force will be reduced, and the buoyancy force will be increased. Therefore, the rising velocity of the bubble increase with increasing the Eo number. The simulation conditions remain the same except for the Eo numbers. The Eo numbers for 6 test cases are 20, 40, 60, 80, 100, and 150. The N_f numbers are 100 for all the cases. The terminal shapes of the bubble are shown in Fig. 5.7. The bubble head is almost the same for all the test cases. There are small differences for $Eo = 20$, for which the bubble head has a larger radius. The shape differences can be distinguished at the tail of the bubbles. For a fixed N_f number ($N_f = 100$), the bubble tail changes from the convex shape to the concave shape with increasing the Eo number. The

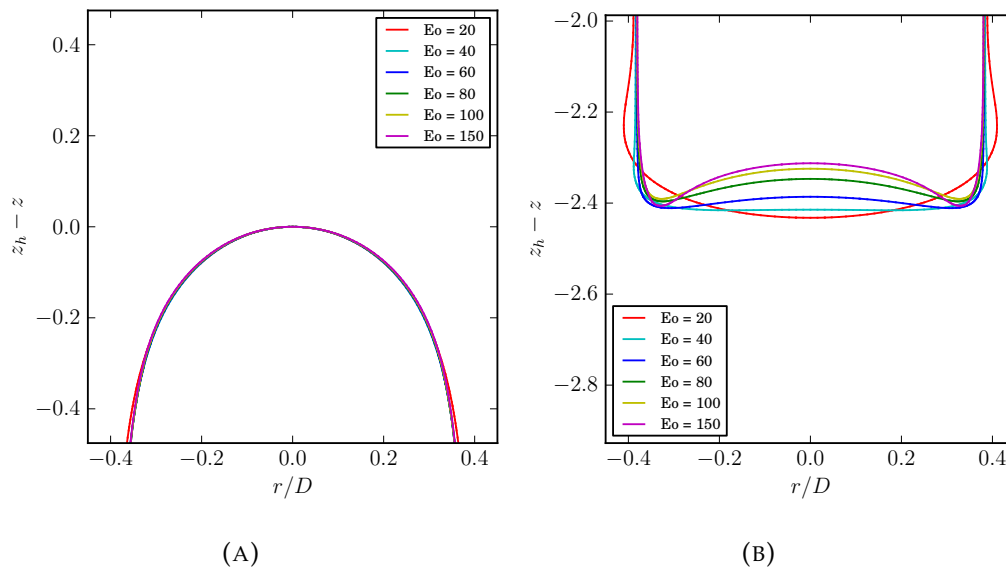


FIGURE 5.7: (A) Effect of viscosity ratios on bubble tail shapes. (B) Effect of viscosity ratios on the bubble terminal velocities.

critical E_o in the present cases with a flat bottom is around 40. Kang, Quan, and Lou [53] tested the E_o number up to 304 and obtained a skirted tail shape.

5.2.6 Summary

A few variables has been tested in sensitivity analysis. The conclusions can be drawn:

- Mesh: Considering the computational load and the accuracy, the mesh M2 is suitable for carrying out the simulation of the Taylor bubble.
- Initial bubble length: It only affects the transient behavior of the bubble. an independent value of the bubble terminal state.
- Density ratio: It has minor effects on the bubble terminal velocity when it is larger than 100. The density ratio is set to $r_\rho = 1000$ in the remainder of this work.
- Viscosity ratio: It has minor effects on the bubble terminal velocity and the bubble shape. Its effect can be ignored. The viscosity ratio is set to $r_\mu = 100$ in the remainder of this work.
- E_o number: It has strong effects on the bubble tail shape.

5.3 Comparison with experiments

5.3.1 Shape comparison

The bubble shape in the straight tube is defined by the liquid properties. Here, we compare the shape of the bubbles with those obtained from the simulations. Figures 5.8 to 5.12 show the terminal shape of the bubbles for different glycerol-water solutions. The properties are presented in terms of the dimensionless numbers (Eo and Mo). The bubble shapes obtained from the experimental tests are shown on the right of each figure, which are the original figures from the high speed camera. The simulation results are shown on the left of each figure. Both numerical and experimental figures are rescaled to the same dimension for comparison. z_0 is the reference point, which is the end of the lower tube.

TABLE 5.2: Dimensionless numbers of the Taylor bubble in the tube with $D_{in} = 16.40$ mm.

Solution	Eo	N_f	Mo	$\log(\text{Mo})$
W-G 95%	49.71	15.14	2.34	0.36
W-G 90%	49.10	27.40	0.21	-0.68
W-G 80%	47.52	81.91	0.0024	-2.62
W-G 70%	41.86	134.93	0.00022	-3.65
W-G 60%	40.55	230.90	0.000023	-4.63

The general side by side shape comparisons of the bubble are shown in Fig. 5.8 to 5.12. The percentage of the W-G solution changes from 95% to 60%. The Eo number changes from 49.7 to 40.55. The bubble has an oblate nose and tail shape (Fig. 5.8 and 5.9). Decreasing the glycerol percentage in the liquid, the bubble tail becomes flat (Fig. 5.10) or concave (Fig. 5.11). The diluted solution leads to decreasing the viscosity, i.e. increasing the N_f number. Whereas, the Eo number does not change too much with the changing of glycerol percentage. Therefore, the viscosity effects mainly leads to the changing of the bubble tail shape.

The bubble lengths are slightly different in each Fig. 5.8 to 5.12. The difference is due to the error of estimating the bubble volumes. In order to verify the simulation could predict the bubble shape, figure 5.13 shows the bubble nose and tail shape in W-G 95% and W-G 60%. The points indicate the experimental data extracted from the raw images. The lines show the simulation results.

The observations on the bubbles lead to two general conclusions:

- The viscous force decreases with diluting the W-G solution. The nose of the bubbles are oblate spheroids shapes. The tail shapes change from oblate to concave, which seems to exhibit a higher sensitivity than the nose to the influence of viscous force. The surface tension force slightly decreases with diluting the W-G solution, which has minor effect on the bubble shape changing.
- The simulations show a good shape comparison with the experimental results. The concave tail can hardly be observed in the experimental images. The simulation results show more clear results of the tail shapes.

5.3.2 Terminal velocity comparison

Terminal velocity of the bubble indicates the steady state of the bubble. In order to verify that the simulation could predict the terminal velocity of the bubble. A few test cases have been carried out based on the experimental results of White and Beardmore [118]. Their experiments include several gas-liquid systems which correspond to a wide range of Morton numbers. Five different groups of the experimental data have been chosen for the simulation. Reducing the Morton numbers, the influence of the viscous forces on the Taylor bubble velocity increase. The curves for the Morton number less than 4.7×10^{-5} would merge into a single line, which is typical for very dilute aqueous solutions. The flow regimes would lead to turbulent flow [10]. However, we choose the bubble in the laminar regime to simulate.

On the other hand, there are many correlations to predict the terminal velocity of the Taylor bubble. A review of these correlations can be found in Section 2.3.1. Three correlations has been chosen to compare with the numerical and experimental results. The first correlation is proposed by Wallis [116]. And, the second one is proposed by Viana et al. [115], which have already taken the data of White and Beardmore [118] into account. The third one is proposed by Hayashi, Kurimoto, and Tomiyama [44].

The results are shown in Fig. 5.14. Each Morton number corresponds to 3 curves which are predicted by different correlations. The experimental data from [118] and corresponding simulation data are added to Fig. 5.14 for comparison purposes.

The results show that the best correlation for the present simulations is that of Viana et al. [115]. The mean relative error (MRE) is -13.03%. The correlation of Wallis [116] deviates from the simulation results more than -19% (MRE). The terminal velocity deviates from all three correlations where Eo number less than 10. The reason is that the low value of the bubble velocities are much more sensitive to small numerical errors. For the bubbles at large Eo number ($Eo > 10$), the simulation results agree very well with the correlation predictions.

We compare our experimental results with the correlations of Viana et al. [115] and Hayashi, Kurimoto, and Tomiyama [44]. In the present experiments, the bubble nose of velocity (U_h^*) close to the outlet of the lower tube is considered as the bubble terminal velocity (V_T). The length for stabilizing the bubble is larger than $70D$. Therefore, it can reasonably believe that the bubble reaches the terminal state. Figure 5.15(A) shows errors between the experimental data and the correlations. The mean relative error of both correlations are less than 5%. The Eo numbers for water-glycerol solutions in the present study is between 40 and 50. In this region, the correlation could predict the terminal velocity very well.

We simulated the bubbles in the present experiments. Figure. 5.15(B) shows the errors of the experimental results compare to the numerical results. The mean relative error is less than 1%.

5.3.3 Liquid film comparison

The wall effects can not be ignored when the bubble rises in the straight tubes. The terminal velocity and the film thickness of the bubbles are affected by the wall. Obviously, the wall effects depends on the bubble volume. We define here the spherical equivalent diameter (D_s)

to represent the size of the bubbles. It can be written as follows:

$$D_s = 2R_s = 2(3/4\pi V)^{1/3} \quad (5.3)$$

where V is the actual bubble volume. R_s is the spherical equivalent radius. The ratio between the spherical equivalent diameter (D_s) and tube diameter (D) indicates the proportion of the tube occupied by the bubble. If $D_s/D > 1$, the bubble can be considered as the long bubble rising in relatively small tubes [41]. The bubble behavior is expected to be somewhat independent of the bubble volume.

In the present study, we normalize the bubble volumes to the spherical equivalent diameters by equation (5.3). The film thickness (λ) is obtained from experimental data. It is simply considered as the minimum distance from the bubble interface to the tube wall. Figure 5.16 shows the film thickness in different water-glycerol solutions. The results have been compared with the correlations presented in Section 2.3.1. The results show that the film thickness increases if D_s/D is less than 1. The reason is that the bubbles in such condition has relatively small volume. The bubble shape is close to a spherical shape. And, the liquid film does not fully develop. Therefore, the film thickness for the Taylor bubble can be obtained only if the D_s/D is larger than 1.

The present experimental data points compared with existing correlations are summarized in Table 5.3. The mean relative errors and the mean absolute errors are shown. The best correlation is the one proposed by Llewellyn et al. [61]. The mean absolute value is 9.3%. The mean relative value is 7.7%. It seems that other correlations over estimate the film thickness. For bubbles in diluted water-glycerol liquids, the correlation proposed by Lel et al. [59] shows a better estimation.

The numerical simulation results are also added in Table 5.3. The simulations are not performed for all the data points in the experimental. We have chose only one data point for each water-glycerol solution. The results show that the simulations accurately predict the liquid film thickness.

TABLE 5.3: Film thickness data points in different water-glycerol solutions compared to correlations from literature.

log(Mo)	Nusselt	Brown	Lel et al.	Kang et al.	Llewellyn et al.	Simulation
0.37						
MRE(%)	12.52	22.13	32.52	16.05	0.79	1.21
MAE(%)	12.52	22.13	32.52	16.05	4.22	5.12
-0.68						
MRE(%)	10.04	11.90	17.46	8.19	1.27	2.34
MAE(%)	10.04	11.90	17.46	8.23	4.26	5.13
-2.62						
MRE(%)	23.00	17.59	17.15	20.90	15.33	18.22
MAE(%)	23.00	17.59	17.15	20.90	15.33	18.22
-3.65						
MRE(%)	17.12	10.92	8.48	18.19	10.03	13.44
MAE(%)	17.12	11.14	9.10	18.19	10.37	15.60
-4.63						
MRE(%)	17.15	11.22	7.68	22.54	11.19	14.51
MAE(%)	17.29	12.34	9.84	22.54	12.32	11.78

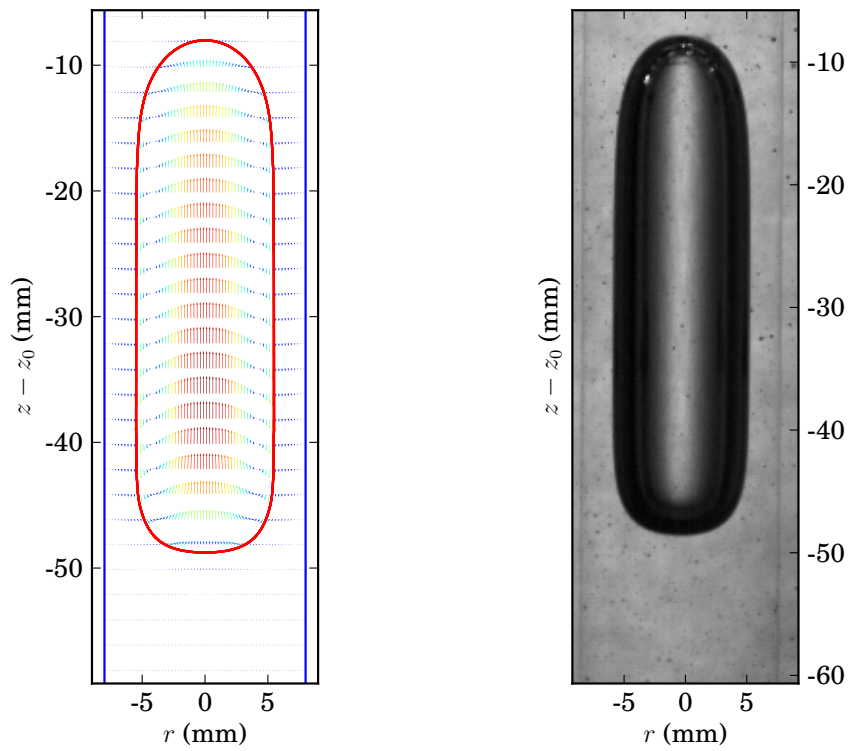


FIGURE 5.8: Comparison of the bubble shape.
(W-G 95%, $Eo = 49.7$, $\log(Mo) = 0.37$)

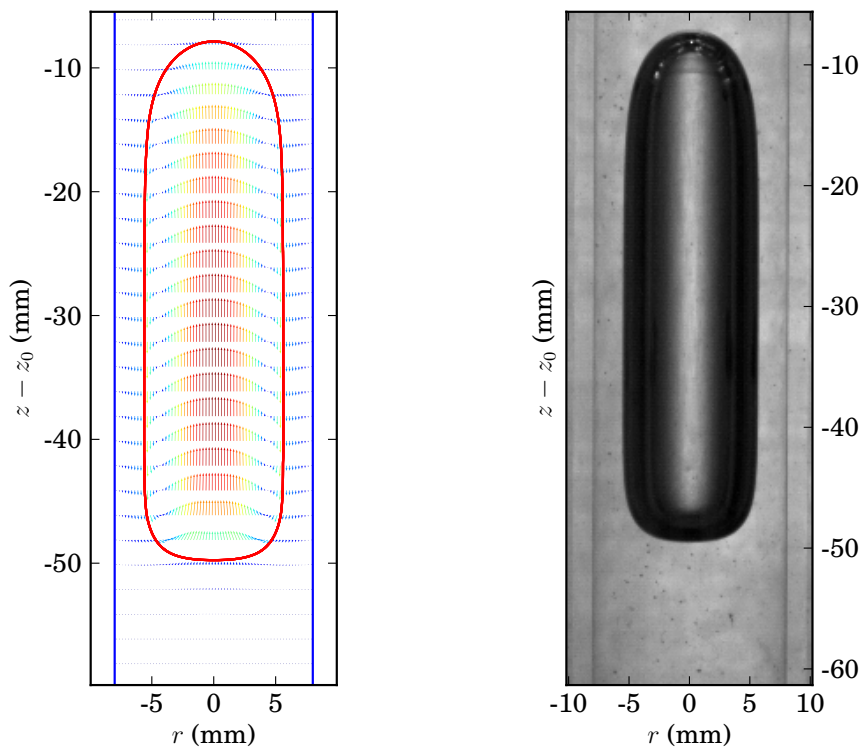


FIGURE 5.9: Comparison of the bubble shape.
(W-G 90%, $Eo = 49.1$, $\log(Mo) = -0.68$)

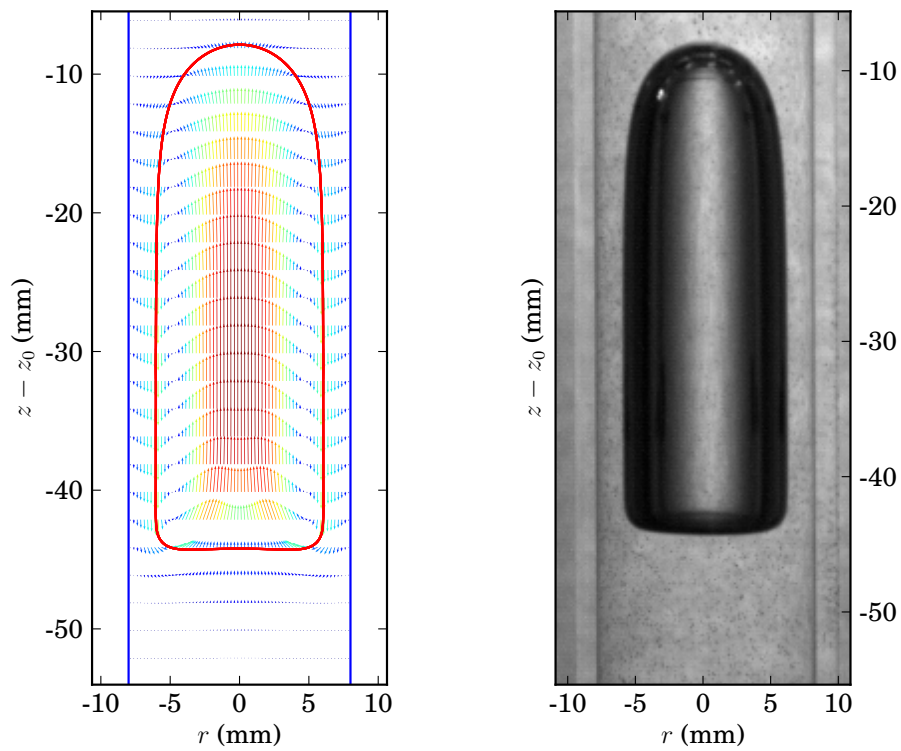


FIGURE 5.10: Comparison of the bubble shape.
(W-G 80%, $Eo = 47.6$, $\log(Mo) = -2.62$)

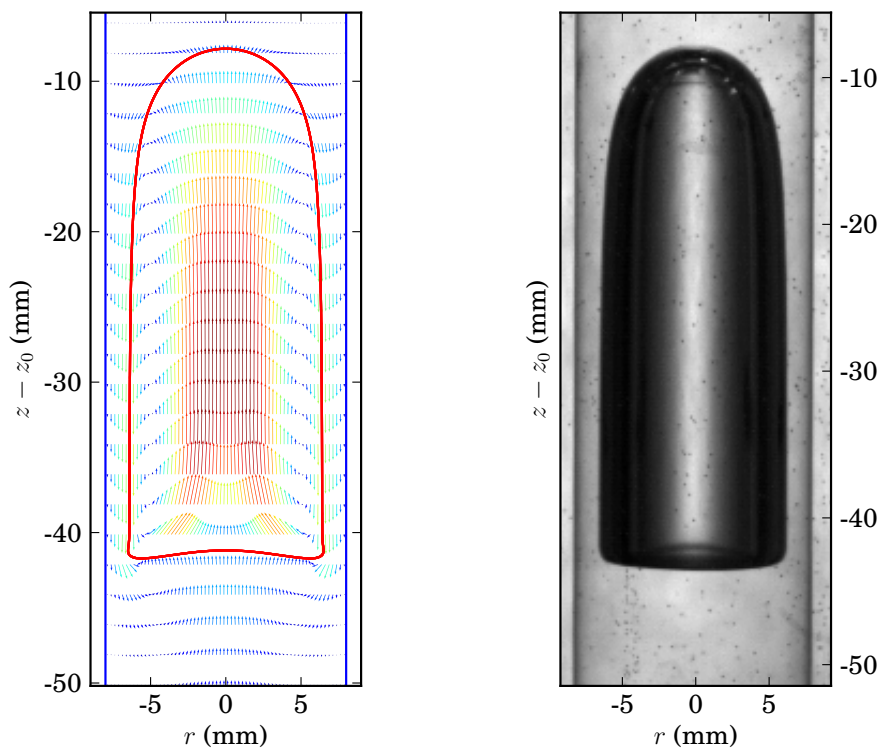


FIGURE 5.11: Comparison of the bubble shape.
(W-G 70%, $Eo = 41.9$, $\log(Mo) = -3.65$)

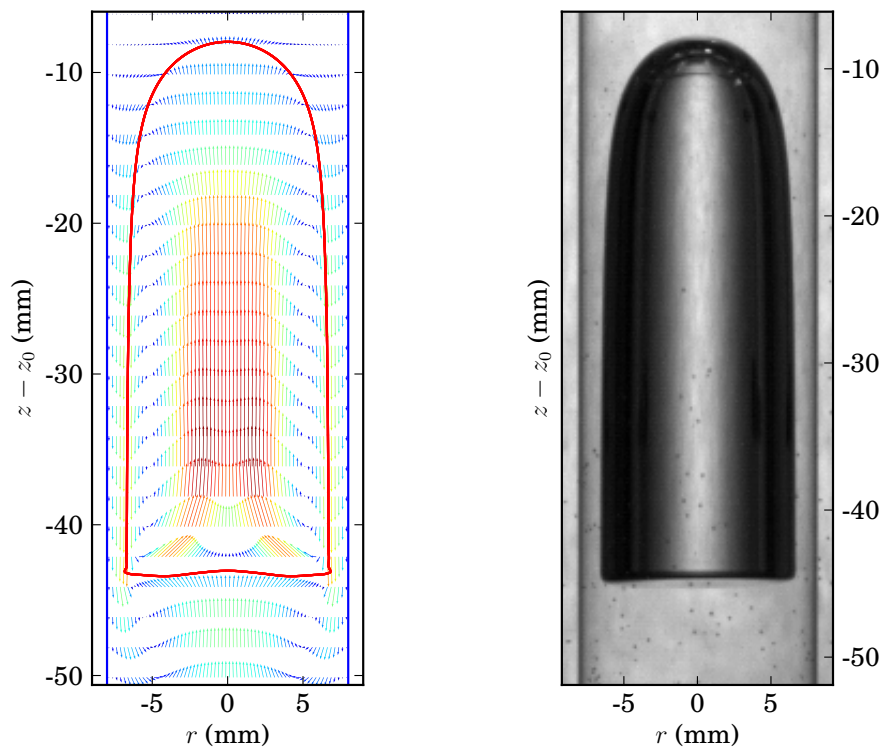


FIGURE 5.12: Comparison of the bubble shape.
((W-G 60%, $Eo = 40.55$, $\log(Mo) = -4.63$)

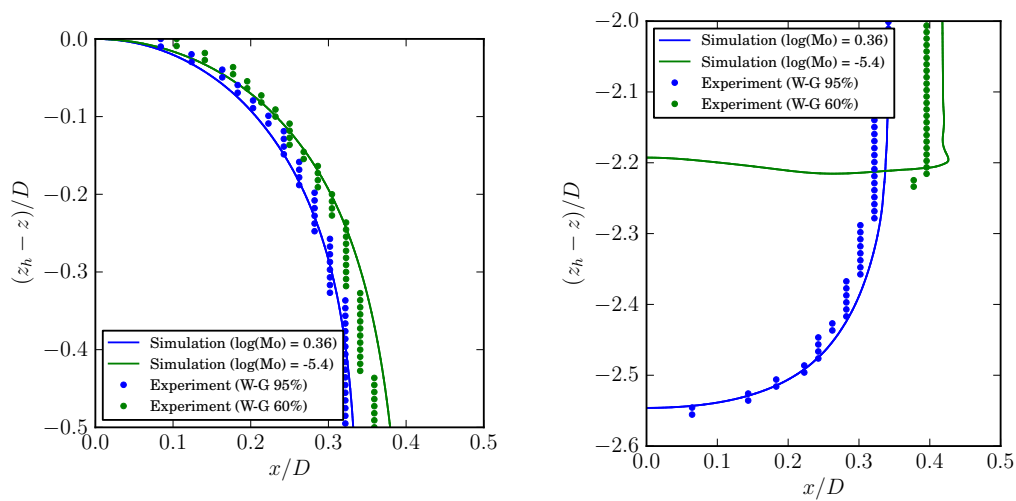


FIGURE 5.13: Comparison of the bubble nose and tail shape.

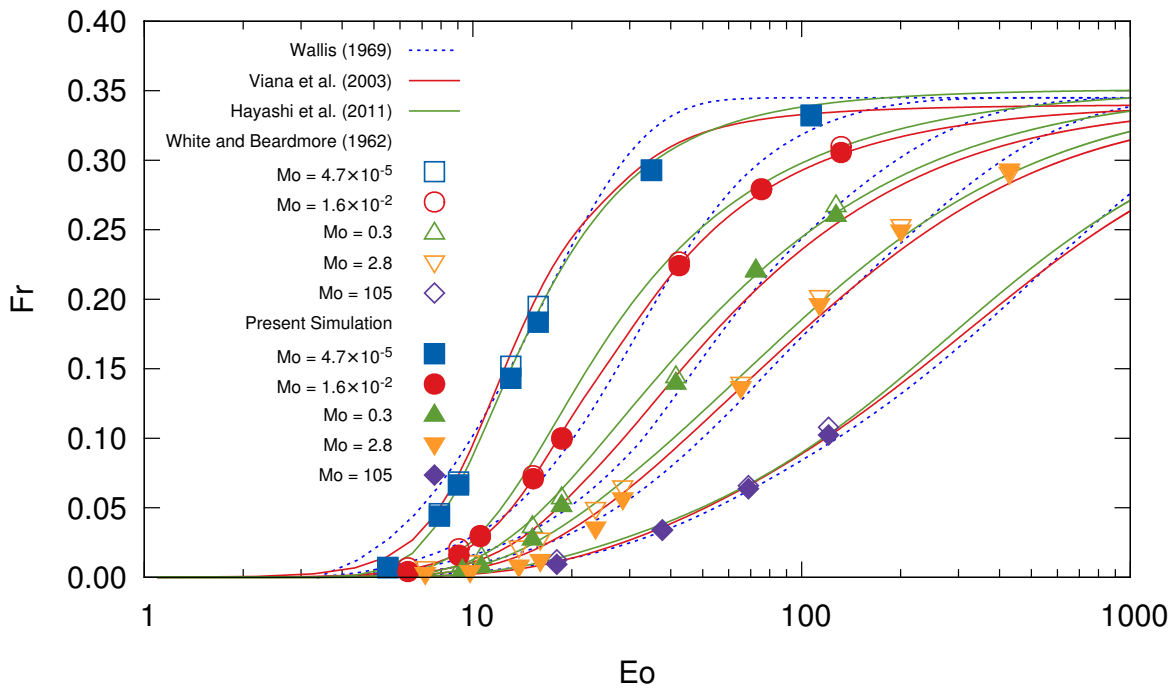


FIGURE 5.14: Numerical results (filled symbols) of the Froude number plotted as a function of the Eötvös number and for different values of the Morton number. The dashed and solid lines correspond to the correlations of Wallis [116], Hayashi, Kurimoto, and Tomiyama [44], and Viana et al. [115]. Experimental data (open symbols) from White and Beardmore [118] are also added for comparison.

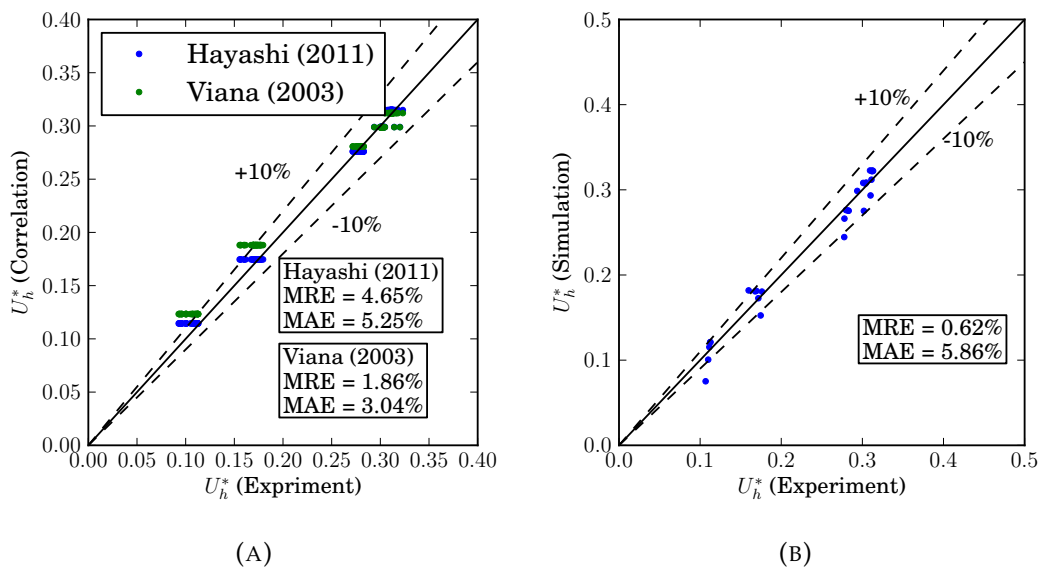


FIGURE 5.15: Comparison of the terminal velocity. (A) Experiments vs. correlations (B) Experiments vs. simulation.

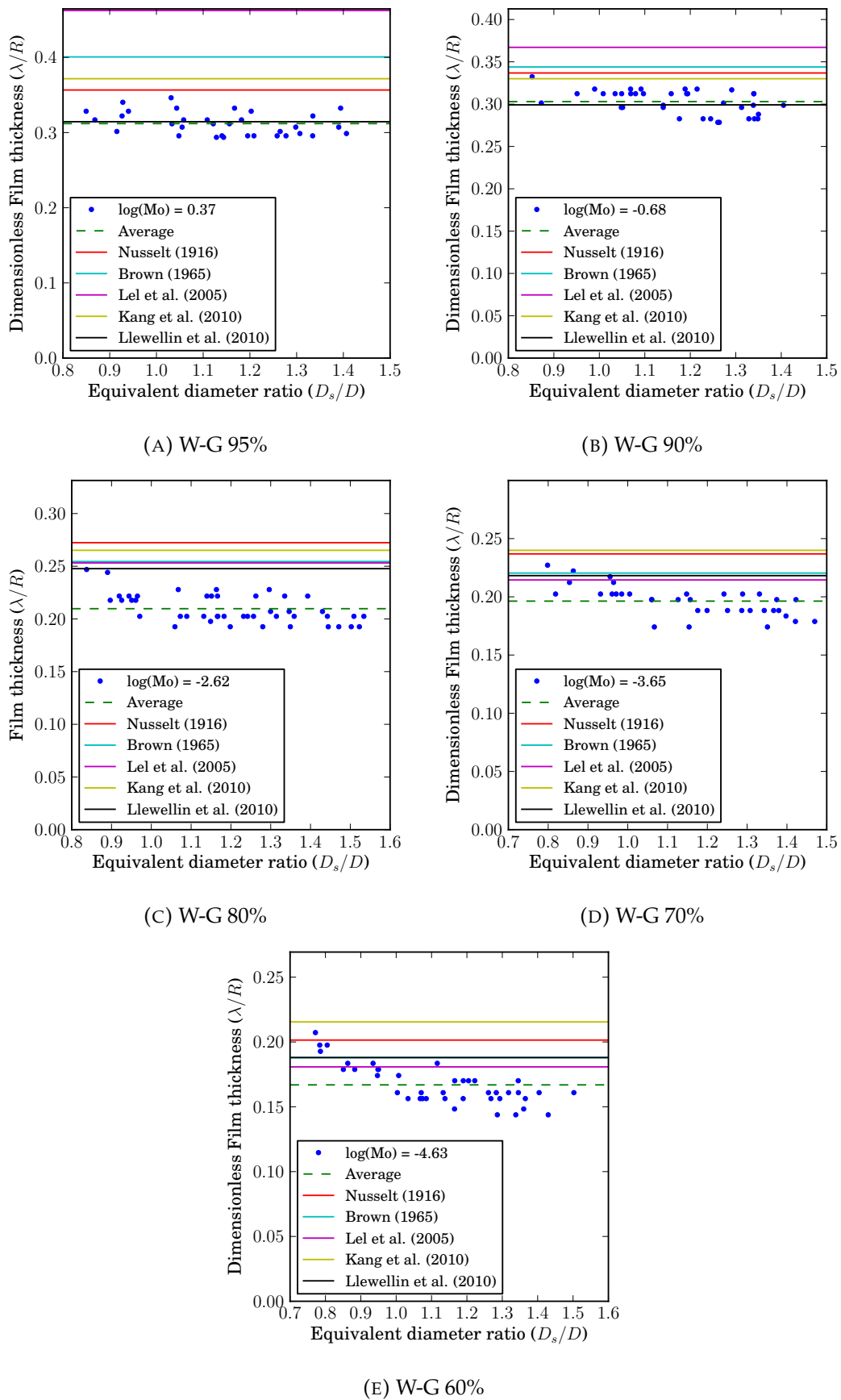


FIGURE 5.16: Comparison of film thickness for different D_s/D and water-glycerol solutions.

5.3.4 Velocity field comparison

We reproduced one of the experimental cases reported in [10], for a system with stagnant liquid, Mo of 4.31×10^{-2} and N_f of 111. In Fig. 5.17, the resulting numerical velocity fields and streamlines are presented. The steady state criteria for the rising bubble is the variation of the velocity of bubble nose. When this velocity changes less than 1% compared to the velocity at the previous time step, we consider the bubble reaches its steady state ($V_T = U^* = U_h^*$). The dimensionless time ($t^* = t\sqrt{g/D}$) of the bubble in Fig. 5.17 equals 10, which already satisfied the steady state criteria. We subtract the terminal velocity of the bubble from the whole flow field. This procedure facilitates to plot the streamlines. Fig. 5.18 and Fig. 5.19 show dimensionless axial velocity profiles above the bubble nose and wake regions. The four locations of the velocity profiles are also shown in Fig. 5.17. Fig. 5.18 and 5.19 shows our simulation data compare well with the experimental data (the points) of [71] and [72]. The numerical results (the dash line) of [10] are also added in Fig. 5.18 and 5.19, which show a close agreement with our simulation data (solid line).

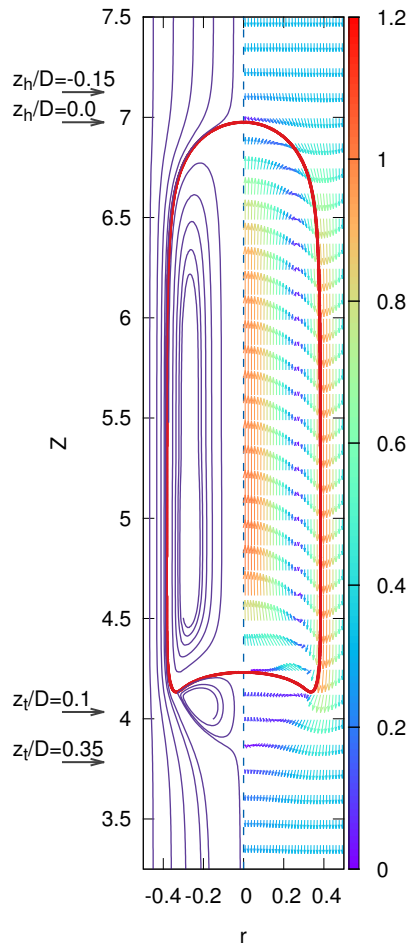


FIGURE 5.17: Numerical velocity fields and streamlines for a case with $Mo = 4.31 \times 10^{-2}$ and $N_f = 111$.

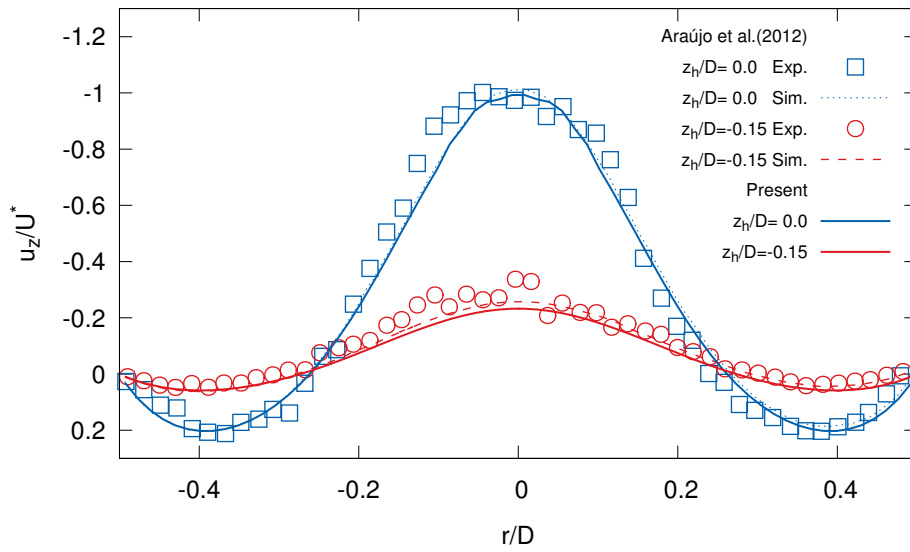


FIGURE 5.18: Comparison of numerical dimensionless velocity profiles (u_z/U^*) at bubble head with numerical and experimental results from [10].

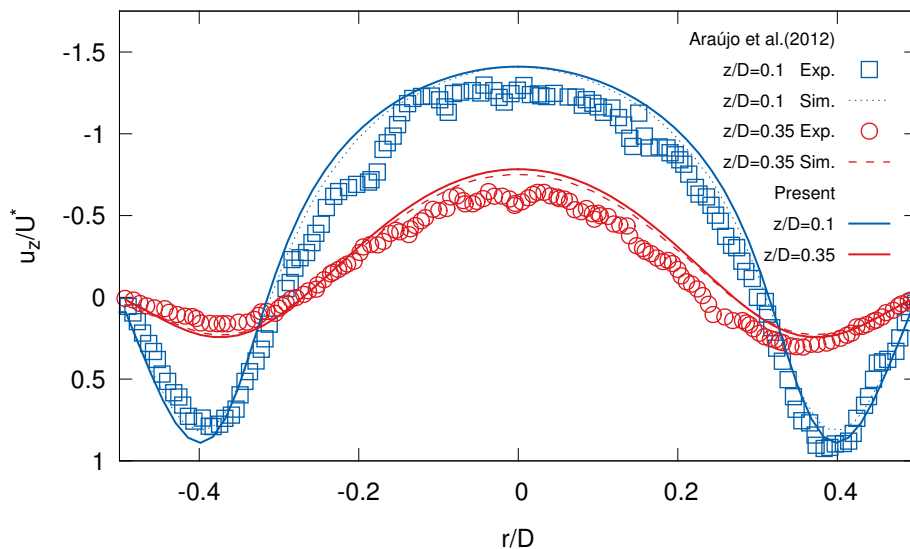


FIGURE 5.19: Comparison of numerical dimensionless velocity profiles (u_z/U^*) at bubble tail with numerical and experimental results from [10].

5.4 Chapter conclusion

The Taylor bubble in straight tubes has been investigated. The sensitive analysis confirmed the parameters used in the simulation. The experimental tests allow to visualize the Taylor bubbles in straight tube ($D = 16.4$ mm). The different bubble shapes can be obtained from different water-glycerol solutions. A few conclusions can be drawn:

- The bubble tail shape are sensitive to the mesh size. The bubble terminal state is independent of the bubble length. Whereas, the bubble transitional state depends on the bubble length.

-
- The density and viscosity ratios have minor effects on the bubble shape. If density ratio is less than 100, it will reduce the rising velocity of the bubble. The viscosity ratio effects on the bubble terminal velocity can be ignored.
 - The simulation can predict the bubble terminal shapes. The comparisons of the bubble shape shows that the simulation predicts the bubble nose and tail shapes in different water-glycerol solutions.
 - The simulation predicts the bubble terminal velocities accurately. The correlation proposed by Viana et al. [115] has the best agreement of the terminal velocities with both numerical and experimental results.
 - If the bubble equivalent diameter is larger than 1, the film thickness becomes to a constant. The correlation of predicting the bubble film thickness which proposed by Llewellyn et al. [61] has the best agreement to the present experimental data. The simulation can also predict the bubble film thickness.
 - The simulation predict the velocity field around the Taylor bubble, which has good agreement with the data present in the literature.

Chapter 6

Bubble rising through the expansion

The objective of this chapter is to obtain a better understanding of the behavior of the Taylor bubbles when they rise through the expansion. The numerical model used in Chapter 5 is extended for simulating the bubble rising through expansions. Experimental results have been obtained for different fluid properties and expansion ratios. The experimental data is used to validate the simulations.

Several bubble characteristics will be discussed in this chapter. First, we analyse the bubble rising through the expansion without breaking up. Then, the bubble break up in the expansion will be investigated.

6.1 Model description

6.1.1 Simulations

The numerical model introduced in Chapter 5 was used to simulate the bubble rising through expansions. The configuration is shown in Fig. 6.1. The bubble initial configuration is the same as that of the model showed in Fig. 5.1. Here, we extend the simulation region to a larger diameter. The diameters of the lower and upper tubes are D_o and D_e , respectively. Thus, the expansion ratio is $\epsilon = D_e/D_o$. The length of the upper tube is $8D_o$, so that the bubble will have sufficient length to stabilize. The connection of the two tubes is the horizontal wall, which makes the connection become a sudden expansion. The boundary conditions for the tube walls are the Dirichlet conditions ($u = 0, v = 0$).

The governing equations are again given by Eq. 5.2. The characteristic length is now the lower tube diameter (D_o). All the lengths are normalized with respect to D_o .

6.1.2 Experiments

The experimental setup was discussed in Chapter 4. The expansion ratios for the experimental tests are listed in Table 6.1. Five different expansion ratios have been tested, which range from 1.12 to 1.72. The inner diameter of the lower tube (D_{in}^{lower}) corresponds to D_o in the simulation. And, the inner diameter of the upper tube (D_{in}^{upper}) corresponds to D_e .

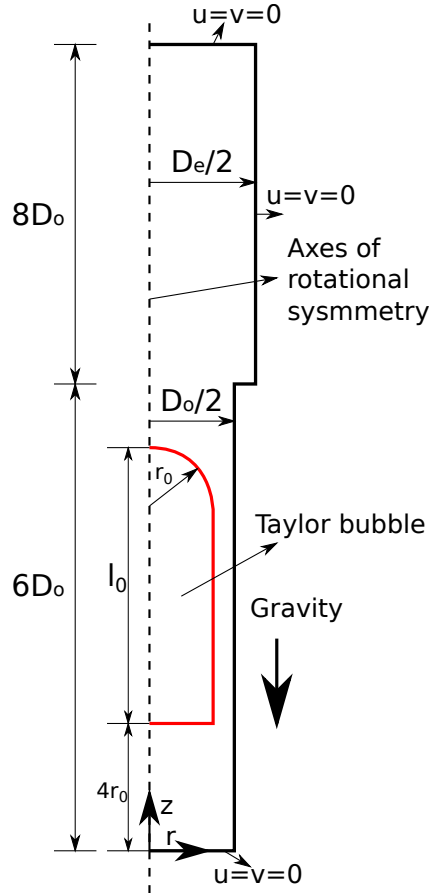


FIGURE 6.1: Initial configuration for the simulation.

TABLE 6.1: Diameters of the tubes.

Index	D_{in} (mm)	D_{out} (mm)	$\epsilon = D_{in}^{upper} / D_{in}^{lower}$
Lower tube			
1	16.40	20.00	
Upper tube			
1	27.80	32.30	1.72
2	23.30	28.00	1.44
3	21.40	26.00	1.33
4	20.00	24.00	1.24
5	18.10	21.90	1.12

6.1.3 Illustration of the bubble features

An overview of the hydrodynamic features described in the present chapter are illustrated in Fig. 6.2. The center of mass is also the geometric center due to the constant density inside the bubble. The figure shows the locations of the bubble tail center and bubble tail in the z direction. For bubbles with non-concave tail shapes, these two locations coincide. The bubble length l_b is defined as the distance from bubble head to bubble tail, Δ_h is the distance from the expansion to the bubble head in the z direction and δ_n is the minimum radius of the bubble body.

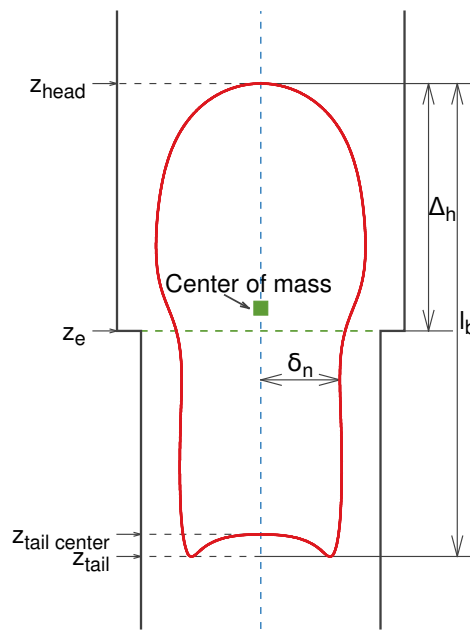


FIGURE 6.2: Illustration of the bubble features described in this study.

6.2 Results

We will first analyze the results for the conditions in which the bubble remains intact when passing through the expansion. Then, we will describe the results for the cases with bubble break-up.

6.2.1 Bubble without break-up in the expansion

Comparison of experiments and simulations

The bubble shape deformations in the expansions is shown in Fig. 6.3 to 6.7. The expansion ratio is the same ($\epsilon = 1.24$). All the bubbles remain intact after passing through the expansion. The experimental images have been compared to the simulation results. The first row in each figure is the experimental results. The second row is the simulation results. When the bubble head reaches the expansion, the time is set to be the starting time ($t = 0.0$ s). Then, the bubble rises through the expansion.

Figure 6.3 and 6.4 show the bubble rising in the W-G 95% and W-G 90% mixtures. The bubbles have a round head and tail shape before entering the expansion. A cone tail shape can be observed when the bubble passes through the expansion ($t = 0.32$ s). Figures 6.5 to 6.7 show the bubble rising in the diluted solutions (W-G 80%, W-G 70%, W-G 60%). The tail shapes are flat before entering the expansion. A concave shape can be observed at the tail of the bubbles ($t = 0.32$ s). In the present tests, two distinctive bubble tail shapes can be observed. When decreasing the viscosity, the bubble tail shape changes from the cone shape to the concave shape.

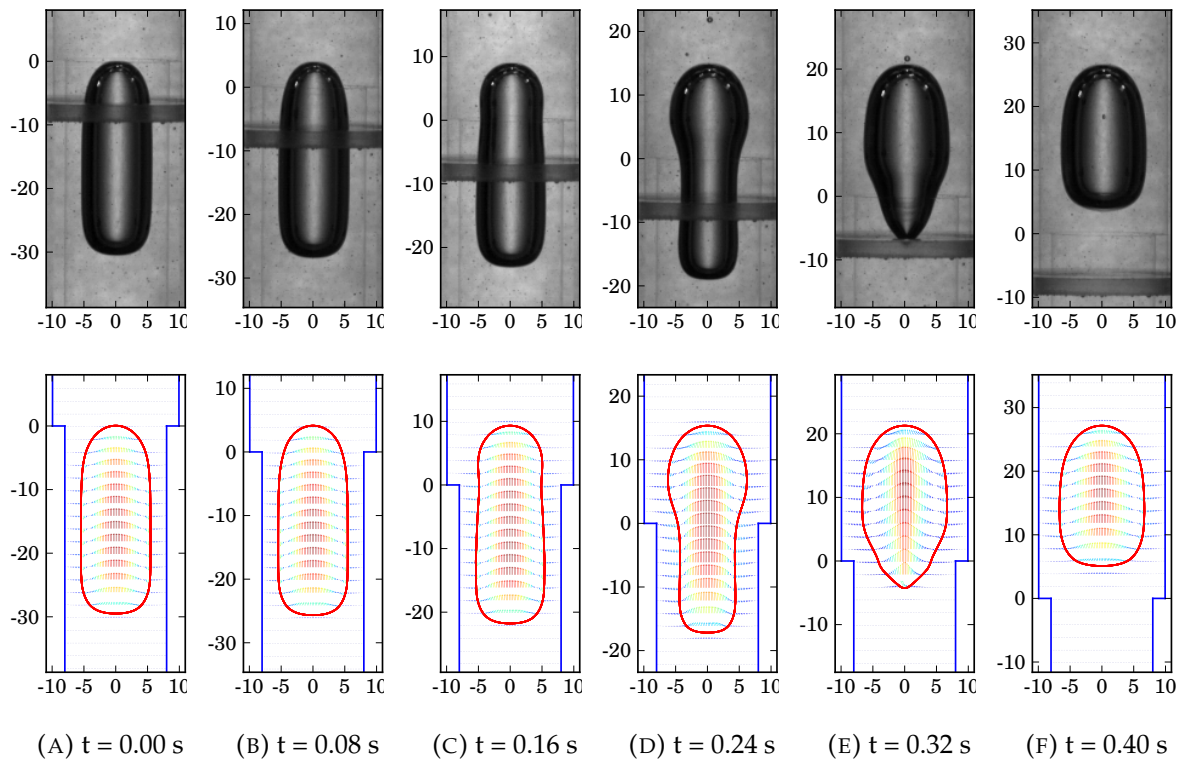


FIGURE 6.3: Experimental and numerical results of the bubble rising through the expansion. ($W-G$ 95%, $Eo = 49.7$, $\log(Mo) = 0.37$, $\epsilon = 1.24$)

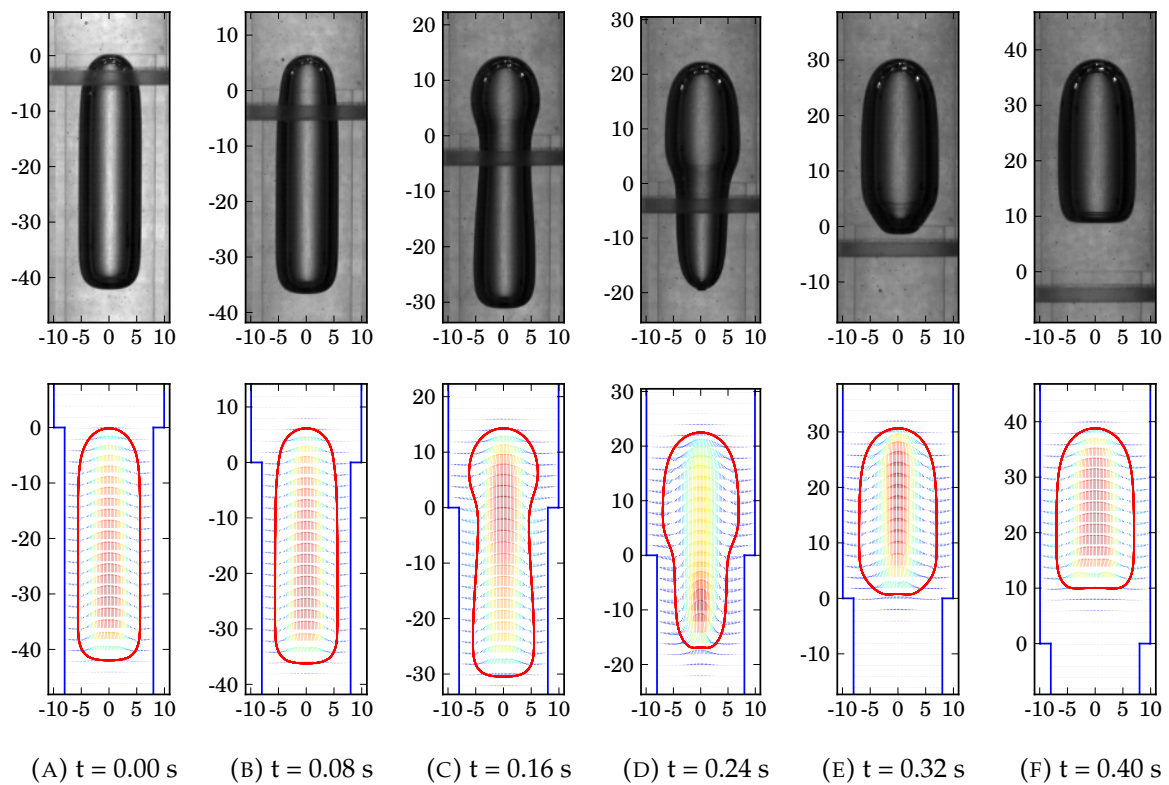


FIGURE 6.4: Experimental and numerical results of the bubble rising through the expansion. ($W-G$ 90%, $Eo = 49.2$, $\log(Mo) = -0.68$, $\epsilon = 1.24$)

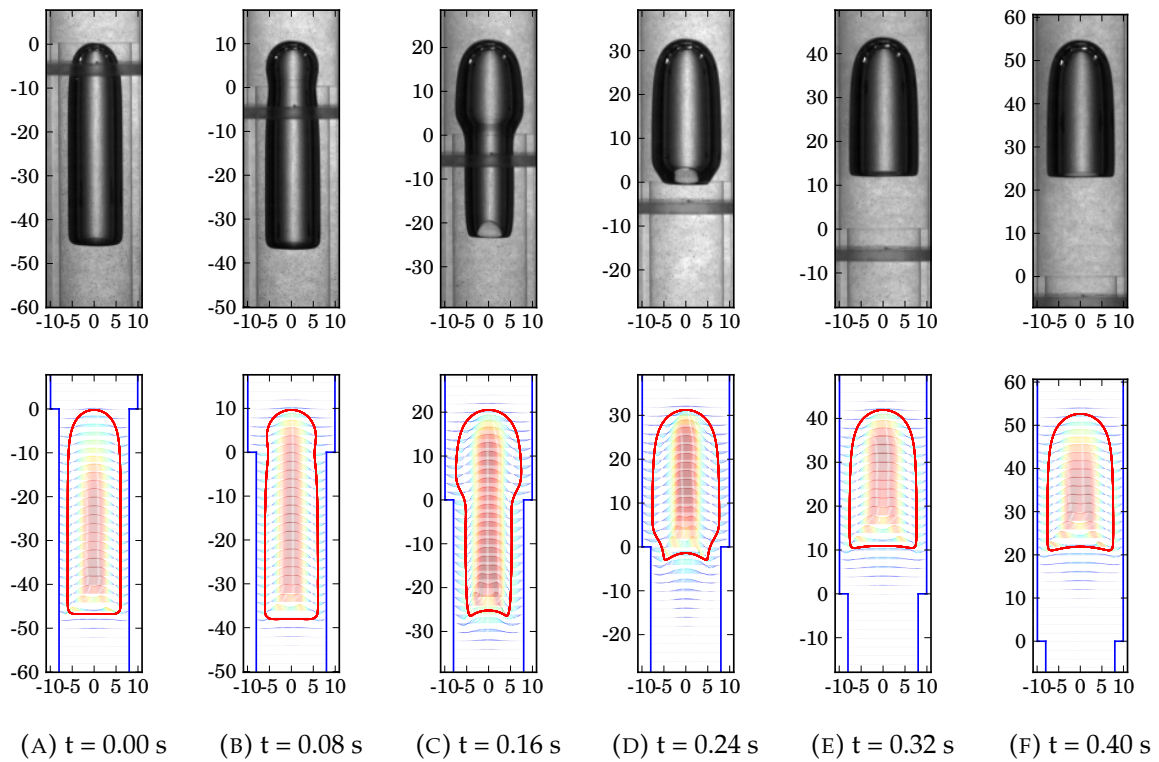


FIGURE 6.5: Experimental and numerical results of the bubble rising through the expansion. (W-G 80%, $Eo = 47.5$, $\log(Mo) = -2.62$, $\epsilon = 1.24$)

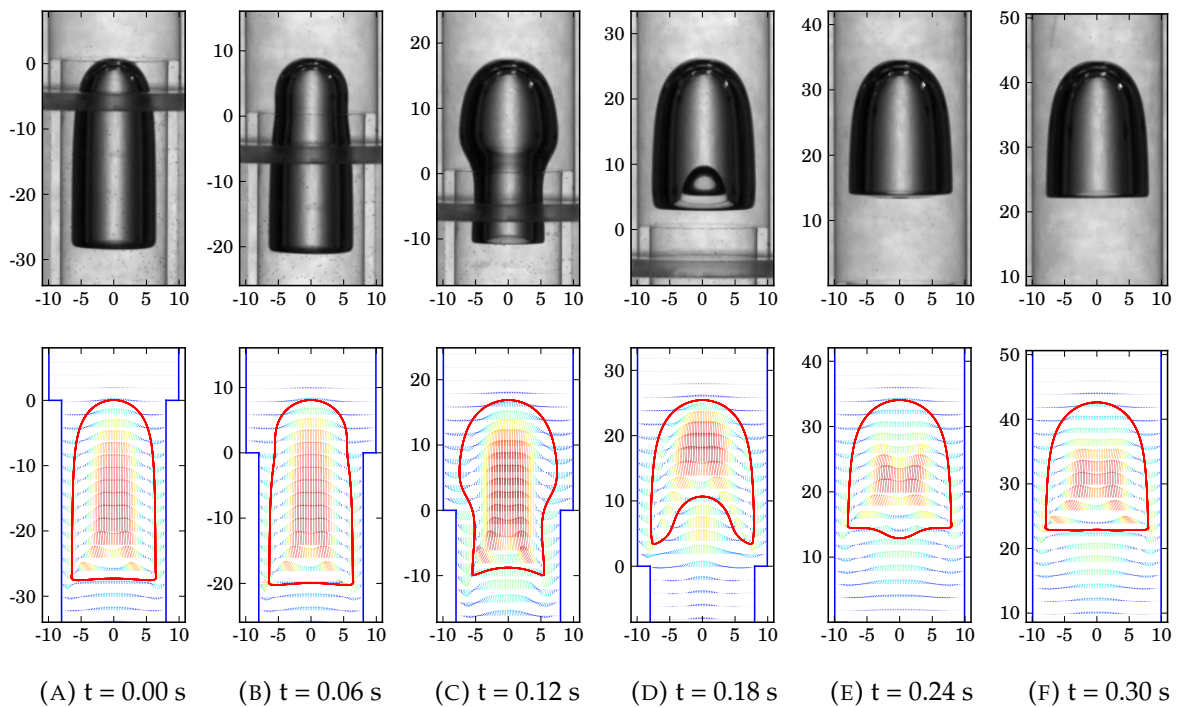


FIGURE 6.6: Experimental and numerical results of the bubble rising through the expansion. (W-G 70%, $Eo = 41.9$, $\log(Mo) = -3.65$, $\epsilon = 1.24$)

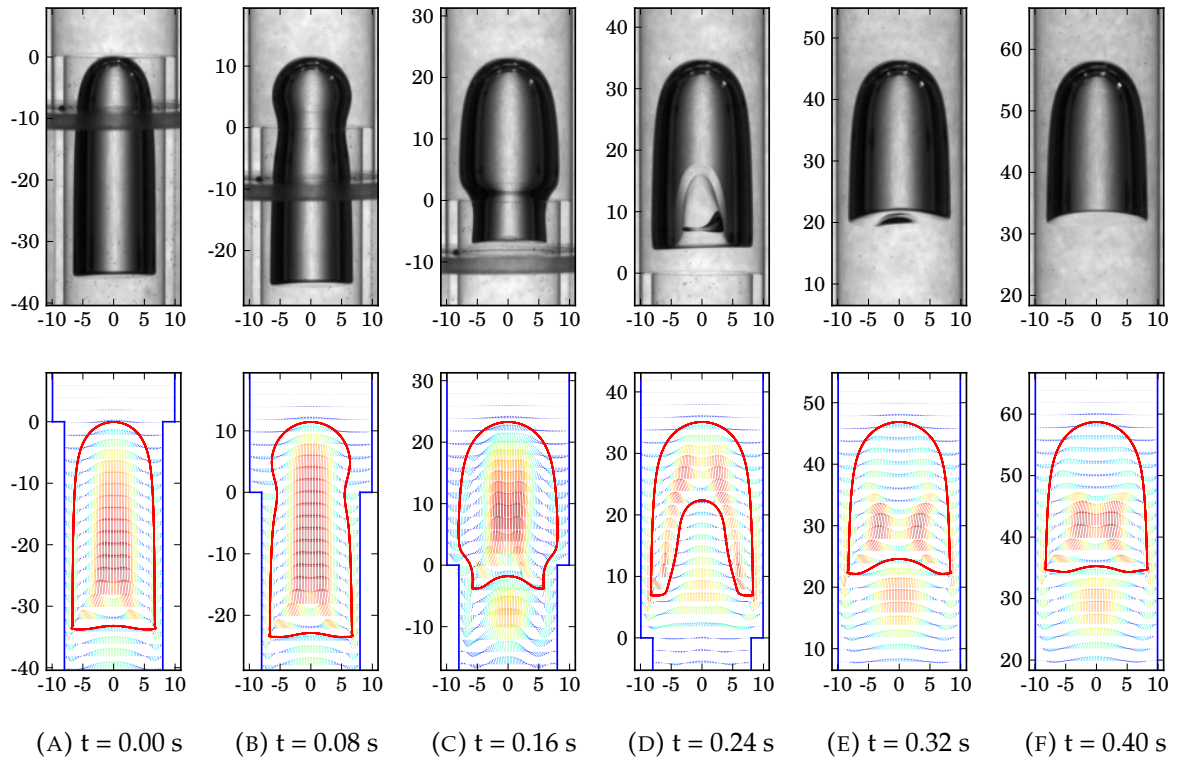


FIGURE 6.7: Experimental and numerical results of the bubble rising through the expansion. ($W-G$ 60%, $Eo = 40.6$, $\log(Mo) = -4.63$, $\epsilon = 1.24$)

Velocity variation

The bubble reaches the steady state before entering the expansion. The bubble velocity will be changed due to the perturbation created by the expansion. The bubble will reach a new steady state in the upper tube. The analysis of the bubble velocity begins with the two terminal velocities.

At this point, we need to adapt the aforementioned dimensionless groups for the straight pipe to the expansion problem due to the change of diameter. The pipe diameter D_o at the lower end of the pipe expands to a new diameter D_e . The local Eo and Fr numbers that include the diameter will change correspondingly. Here, we choose D_o as the reference diameter to calculate the dimensionless numbers before the bubble moves through the expansion, i.e. $Eo_o = \rho_l g D_o^2 / \sigma$ and $Fr_o = V_T / \sqrt{g D_o}$. The Eo_e and Fr_e numbers, characterizing the bubble flow after the expansion, are obtained by substituting D_e into the expressions. In all simulations, the bubble has reached the steady rising velocity before entering the expansion. Some time after the bubble has passed through the expansion, it reaches a new steady state. Figure 6.8 shows the transition of the Eo and Fr numbers between the two steady states for expansion ratios 1.1, 1.2 and 1.3, and for the two cases with Eo_o equal to 50 and 100, respectively. The Morton number remains the same, $Mo = 1 \times 10^{-2}$. As expected, the figure shows a very good agreement between the simulations and the correlation by Viana et al. [115]. Both steady state regimes fall in the conventional scenario of Taylor bubble rising in straight pipes. The remaining of this section will focus on the analysis of the transient state of the Taylor bubble passing through the expansion.

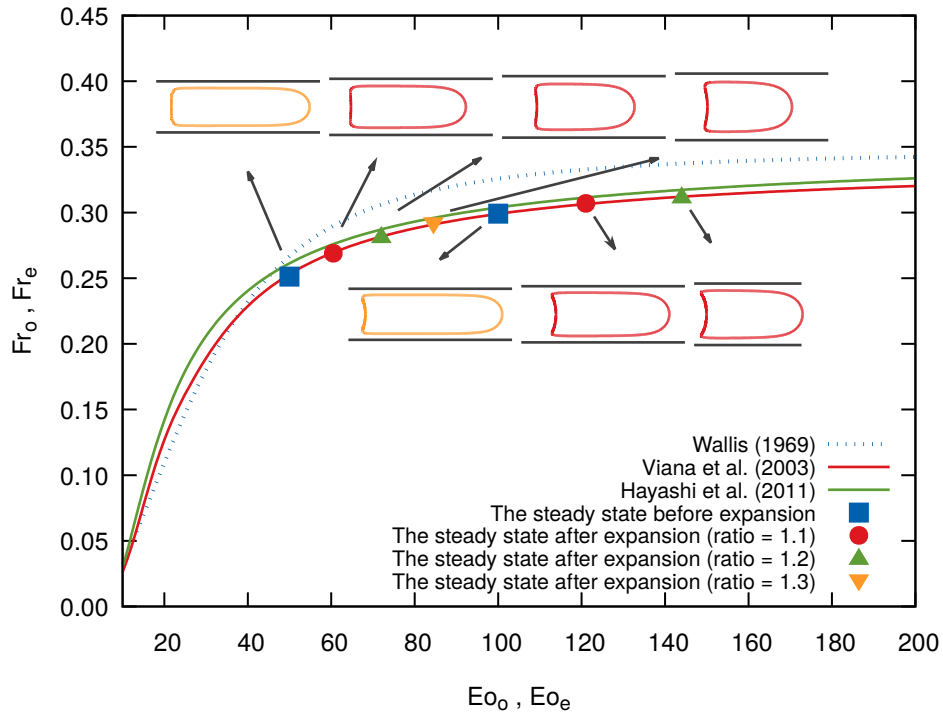


FIGURE 6.8: Numerical results of steady state of bubble ($U = V_T$) before and after the expansion (symbols) and the correlations of Wallis [116] and Viana et al. [115] (line). ($Mo = 1 \times 10^{-2}$)

One important feature reflecting the transient state of the bubble in the expansion is its velocity. We adopt a dimensionless velocity defined as $U^* = U/\sqrt{gD_o}$ with $U = \|\mathbf{u}\|$. In order to show the velocity changes, we choose four typical locations for observation: the tip of the head, the center of the tail, the tip of the tail and the center of mass (Fig. 6.2). The typical evolution of the velocity at these four locations are shown in Fig. 6.9 as a function of the normalized dimensionless time (t^*). The time of the bubble head reaching the expansion is considered as the starting time ($t^* = 0$). The two vertical dashed lines mark the instants of the bubble nose and tail reach the expansion. We see that the head of the bubble accelerates as soon as it passes through the expansion, while the velocity of the tail of the bubble is still unchanged. The bubble head reaches quickly the new terminal velocity (at $t^* \simeq 1.5$) and then remains nearly constant. The tail of the bubble, on the other hand, accelerates with a delay but reaches a peak velocity much higher than the new terminal velocity. As a result, the bubble length decreases when the tail velocity catches up with the head velocity (for $t^* > 8.0$).

A convex tail shape is formed at $t^* \simeq 2.5$. The oscillations are clearly visible on the velocities of the bubble tail, but not so much on the center of mass and the head velocity. It is therefore clear that this phenomenon is related to a perturbation of the tail of the bubble, as also both velocities at this location fluctuate with opposite phases.

The established literature on Taylor bubble rising in straight pipes has shown that the length of the bubble has a minor effect on the terminal velocity [118]. Therefore, in the dimensional analysis concerning straight pipes the dimensionless groups do not include the

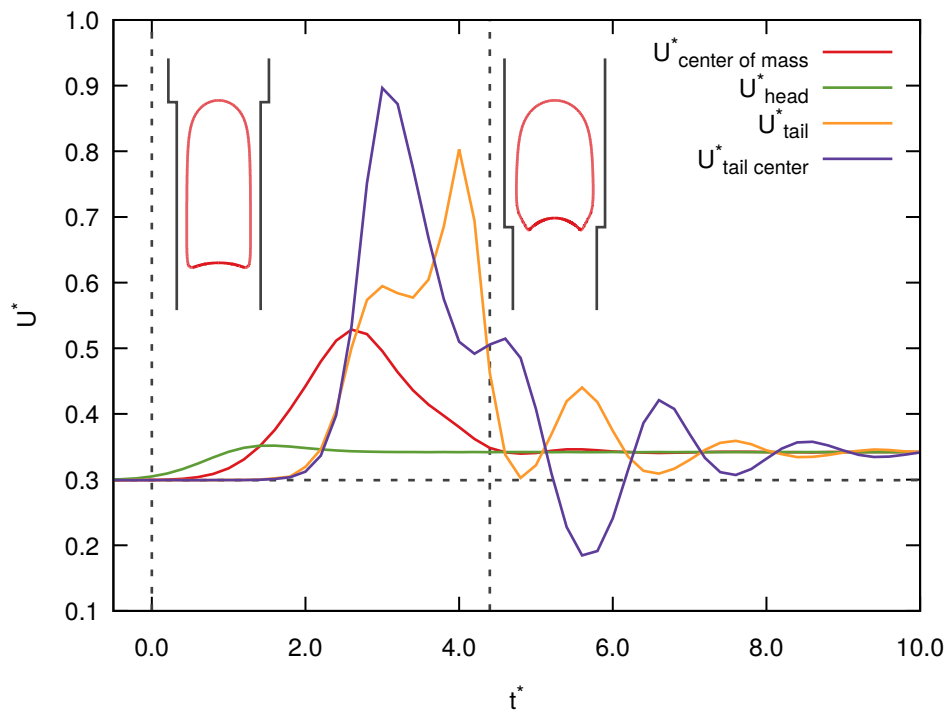


FIGURE 6.9: Evolution of the dimensionless bubble velocity as a function of the bubble head position at four locations of the bubble. The vertical dashed lines mark the location of the bubble entering and leaving the expansion. The horizontal dashed line indicates the bubble terminal velocity before entering the expansion. ($Mo=1 \times 10^{-2}$, $Eo=100$, expansion ratio=1.2)

length of the bubble. However, when the bubble goes through an expansion, the length of bubble is no longer a parameter that can be ignored. A longer bubble will be affected by the expansion over a longer time period. Figure 6.10 shows the bubble velocity of the center of mass for different initial bubble lengths. It is observed that both the peak value of the velocity and the time to obtain a steady state increases with the bubble length.

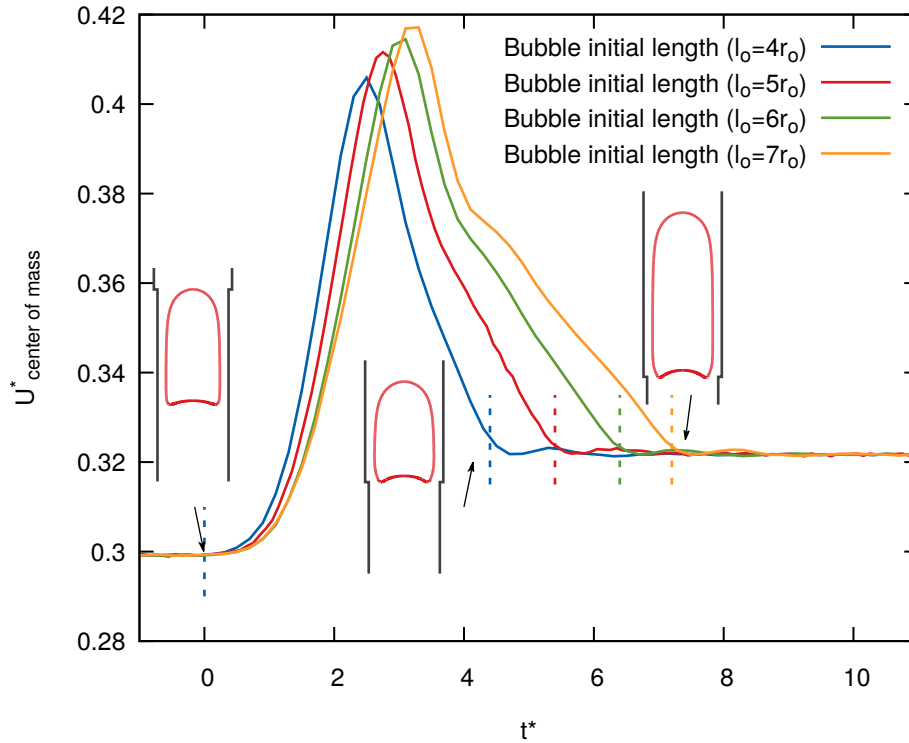


FIGURE 6.10: Evolution of the mass center velocity for different values of the initial bubble length. The dashed lines mark the locations of the bubble entering and leaving the expansion. ($Mo = 1 \times 10^{-2}$, $Eo = 100$, $\epsilon = 1.1$)

Figure 6.11 shows the effect of the expansion ratio and the Eötvös number on the maximum value of the center of mass velocity. As expected, the velocity of the bubbles in larger expansion ratios changes more significantly than in lower expansion ratios. A higher expansion ratio induces a stronger perturbation on the bubble. The maximum velocity increases also for larger values of the Eo number. Bubbles with higher Eo number are less subject to the stabilizing effect of surface tension and are therefore more vulnerable to the perturbation induced by the expansion.

Bubble length variation

Figure 6.12 shows the bubble length variation ($Mo=1 \times 10^{-2}$, $Eo=100$) when it passes through different expansions. The variation can be divided into three stages. The first stage is an elongation in the z direction. The bubble length slightly increases due to the expansion of the head and the shrinking of the body in the radial direction. The concave bubble neck region forms gradually during this stage. In the second stage, we see the bubble shrinking in the z direction. The bubble moves through the expansion in a short period of time as

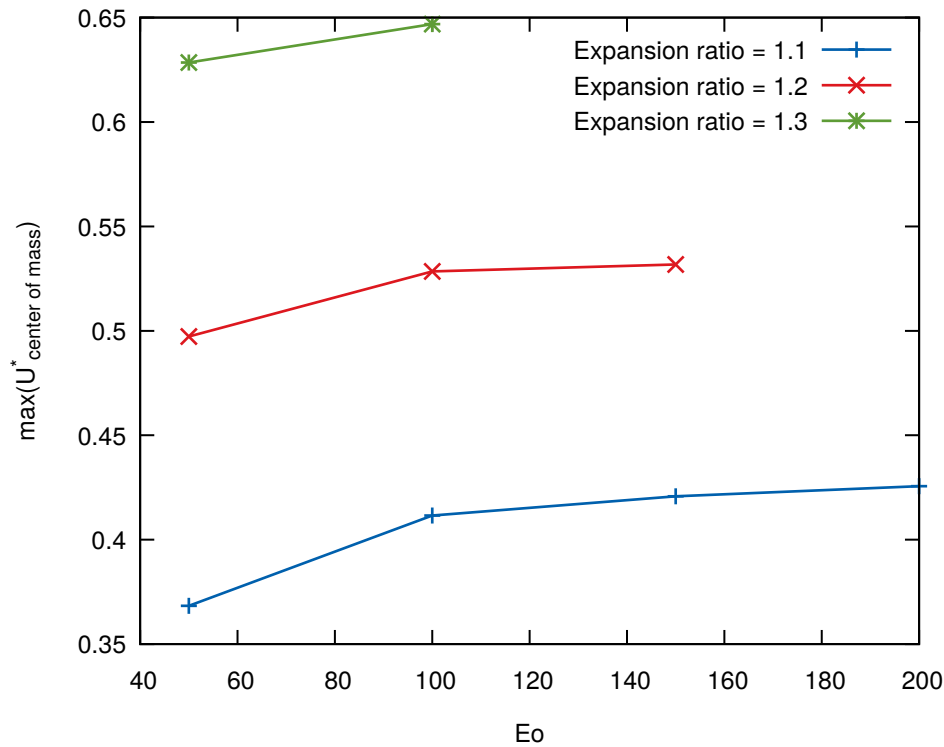


FIGURE 6.11: Maximum value of the bubble mass center velocity as a function of the Eo number for different expansion ratios ($Mo=1 \times 10^{-2}$).

a result of the increased velocity in the middle of the bubble. Since the bubble radius is larger after the expansion and the bubble volume remains unchanged, the bubble length is rapidly decreased. It is noted that the concave shape at the bottom of the bubble is relatively prominent. From a physical point of view, the flow recirculation behind the bubble tail is enhanced due to the increasing velocity in the liquid film. The liquid in the recirculation area pushes the bottom of the bubble inward. When the bubble tail leaves the expansion, the recirculation suddenly decreased due to the enlarged flow area at the back of the bubble. The unstable recirculation flow introduces oscillations at the tail of the bubble. As a result, in the third stage, the oscillation of the bubble length is mainly due to the shape change at the tail of the bubble. When all the velocities at different parts of the bubble become stabilized, the length of the bubble remains constant.

Transition time of the bubble in the expansion

In order to determine the transition time of a stabilized Taylor bubble in a straight pipe, it would be sufficient to know the terminal velocity and the length of the pipe. But when the pipe contains a sudden expansion, we need also to take into account the evolution of the bubble velocity near the expansion. Since the terminal velocities before and after the expansion are perfectly known (and equal to those observed in straight pipes), we only need to take into account the delay introduced by the singularity. This is most easily done by introducing a time shift (Δt_s), defined as the difference of the actual transition time and that obtained without taking into account the singularity. Consider the example in which the

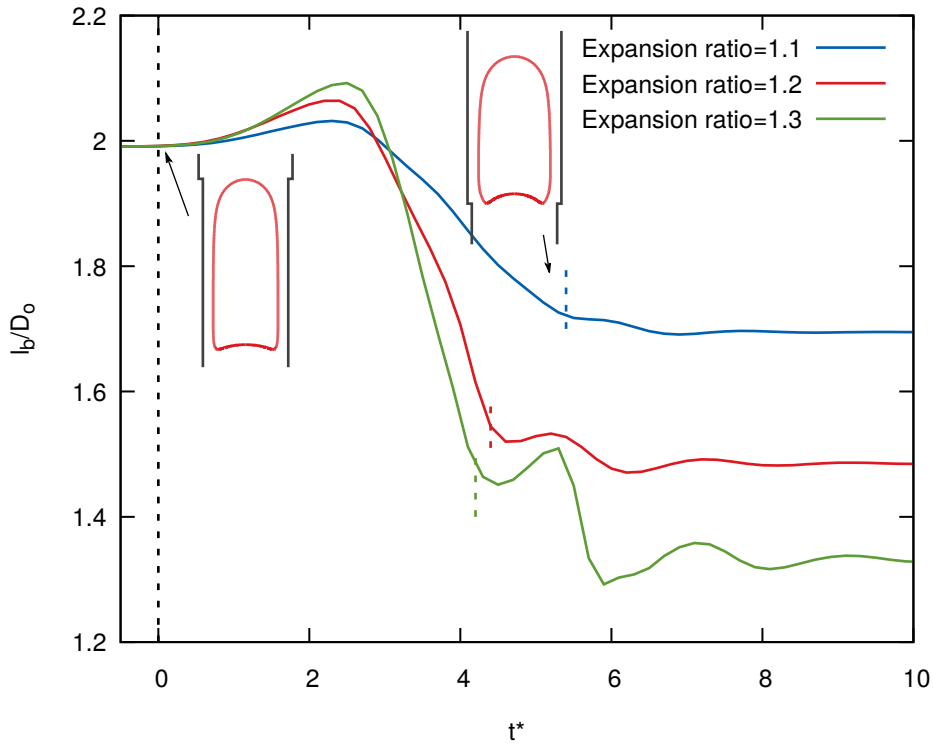


FIGURE 6.12: Evolution of the bubble length for different expansion ratios as a function of the bubble head position. The dash lines mark the locations of the bubble entering and leaving the expansion. ($Mo = 1 \times 10^{-2}$, $Eo = 100$)

length of the pipe below and above the expansion is defined by respectively l_o and l_e (Fig. 6.13). A simple calculation of the regular transition time, not accounting for the singularity, would be given by $l_o/U_o + l_e/U_e$, where U_o and U_e are the initial and final terminal velocities of the bubble. The actual transition time will then be given by:

$$\Delta t = \frac{l_o}{U_o} + \frac{l_e}{U_e} + \Delta t_s$$

where the time shift Δt_s is added to account for the transition in the singularity. From the results in Fig. 6.9, it is easily concluded that the time shift will be positive (a time delay) as the bubble head velocity is initially below the new terminal velocity. For a fixed distance, the bubble spends more time passing through the expansion than the results simply obtained without considering the effect of the expansion.

Figure 6.14 shows the time shift for different expansion ratios and Eo numbers. The bubble spends more time in larger expansions. The increase of the N_f number leads to a higher terminal velocity, but it happens for $N_f < 200$ [53]. In present tests, the N_f numbers are in this range. Therefore, the difference of the two terminal velocities increases in larger expansions. The bubble takes more time to expand in the radial direction to accommodate the larger flow channel. Another trend in Fig. 6.14 shows the shift time decreasing at larger Eo number indicating that the surface tension forces become less significant comparing with the gravitational forces. The deformation of the bubble interface is easier (consumes less energy to deform), thus Δt_s reduces.

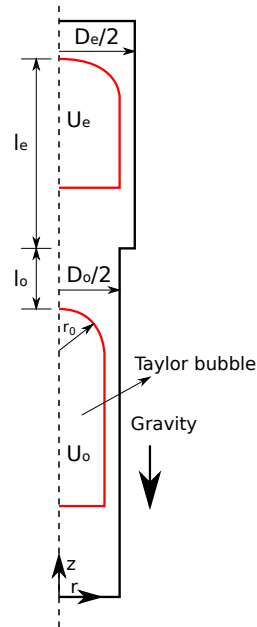


FIGURE 6.13: Illustration of the transition time of the bubble in the expansion.

Necking

When the bubble goes through the expansion, a neck region will appear which is not observed in straight pipes. We define the bubble neck radius δ_n as the minimum cross-sectional radius in the bubble neck region. Figure 6.15 illustrates for different expansion ratios the evolution of the bubble neck radius when the bubble passes through the expansion. Images of the bubble shape when the minimum bubble neck radius is reached are also added. The formation of the bubble neck appears to be the result of the flow pattern in the vicinity of the expansion. When the bubble moves upward and pushes away the liquid above the bubble, a falling liquid film is created that drains the fluid to the region below the bubble. This phenomenon also exists for bubbles in straight pipes, but in the case of an expansion the liquid film encounters a forward facing step forcing the flow towards the bubble. The liquid-gas interface is pushed inwards, thereby creating the concave neck region of the bubble. When the expansion ratio increases, the neck radius is smaller. Because the falling liquid film encounters a larger forward facing step.

6.2.2 Bubble with break-up in the expansion

Break-up patterns

Bubble break-up in the expansion can be observed both in the numerical and experimental tests. Here, we define three patterns of the bubble breaking up in the expansion.

- Necking: the bubble will be pinched off in the radial direction. The necking effect is observed on every bubble passing the expansion, resulting in a reduction of δ_n . If the minimum δ_n is 0, the bubble will be pinched off into two bubbles. A typical necking break-up can be seen in Fig. 6.16.

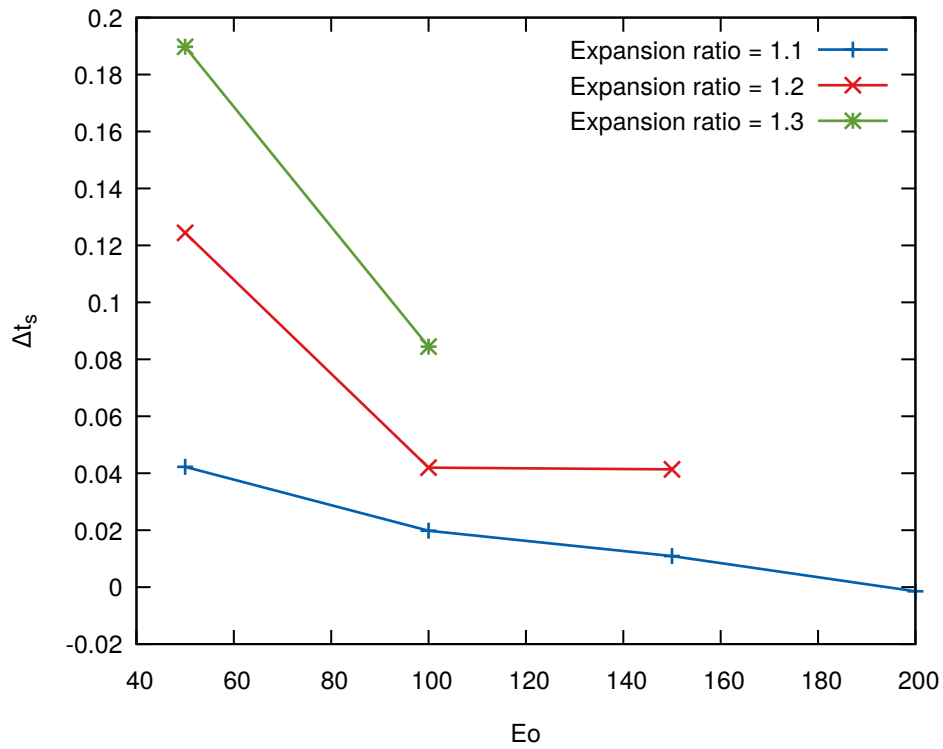


FIGURE 6.14: Time shift of the bubble in different expansion ratios. ($Mo=1 \times 10^{-2}$)

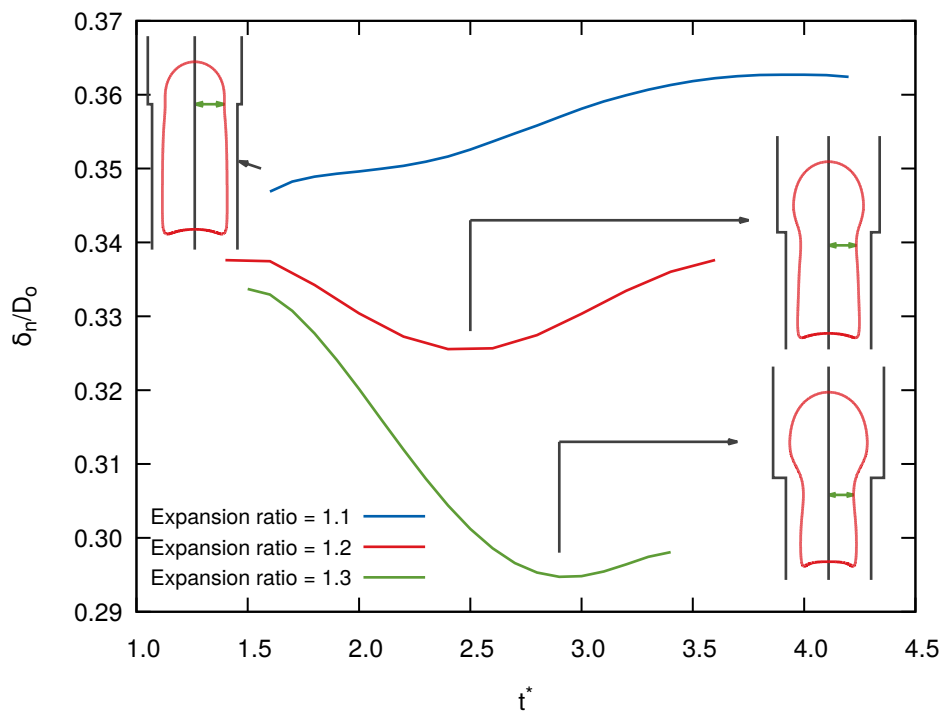


FIGURE 6.15: Evolution of the bubble neck radius for different expansion ratios as a function of the bubble head position. The snapshots show the bubble shape when it reaches the minimum bubble neck radius. ($Mo=1 \times 10^{-2}$, $E_o=100$)

- Penetration: the bubble tail retracts in the bubble body along the tube direction and penetrates the bubble. A typical penetration can be seen in Fig. 6.17.
- Detachment: the downward flow stretches the bubble tail and small bubbles shed off from the tip of the bubble tail. A typical detachment can be seen in Fig. 6.18.

Note that more than one of these break-up patterns can occur during the event of the bubble passing through the expansion. For example, a bubble breaks up due to necking process. It separates into two parts. Then, the leading bubble tail retracts and even penetrates itself. Therefore, two break-up patterns are observed for the same bubble.

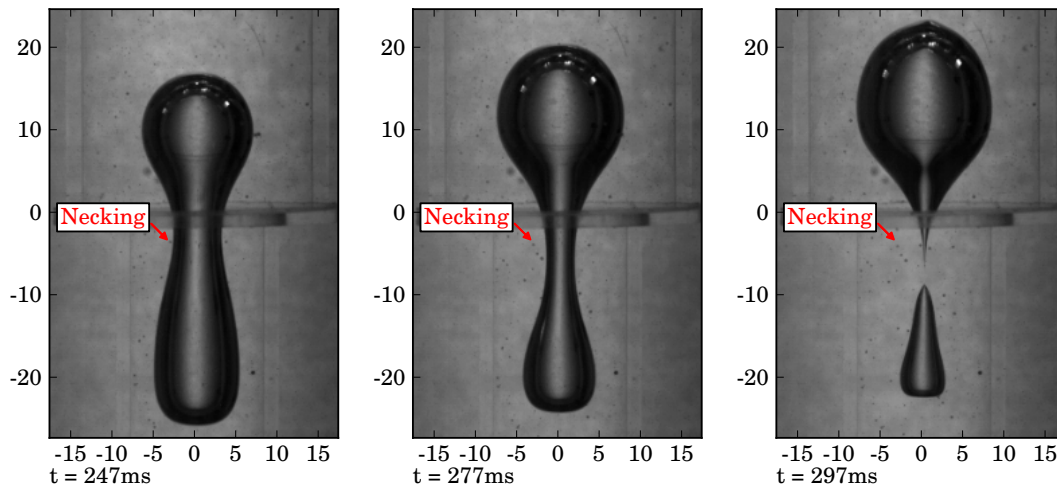


FIGURE 6.16: Bubble break-up in the expansion (W-G 95%, $\epsilon = 1.72$)

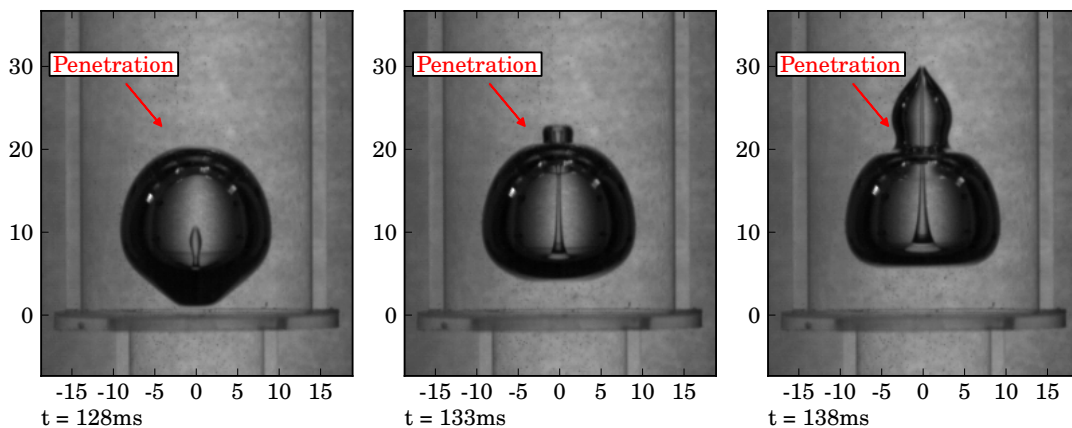


FIGURE 6.17: Bubble break-up in the expansion (W-G 80%, $\epsilon = 1.72$)

Break-up pattern map

A series of simulations are conducted to determine the break-up pattern map for different expansion ratios. The expansion ratios (ϵ) range from 1.2 to 1.7. As explained in Section 6.2.1,

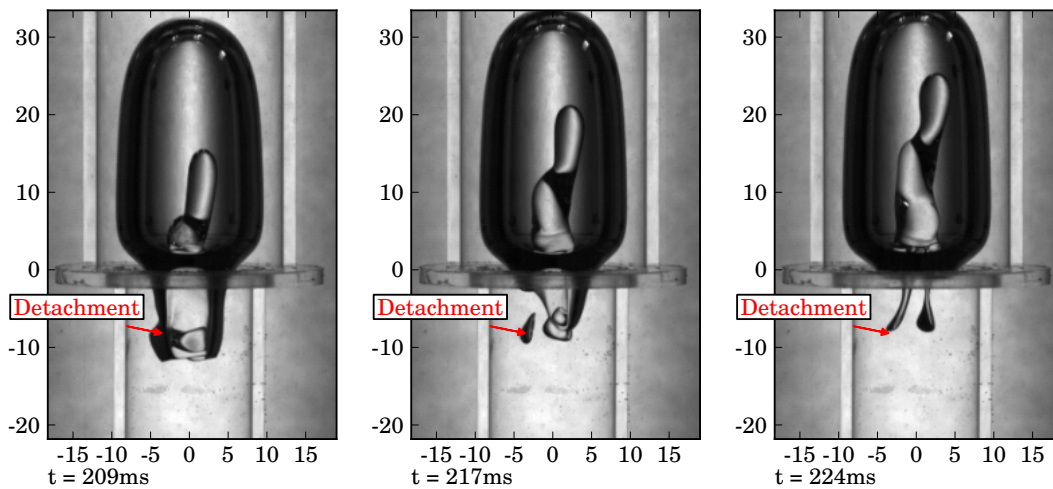


FIGURE 6.18: Bubble break-up in the expansion (W-G 70%, $\epsilon = 1.72$)

the Morton number is a dimensionless number which is independent of the tube diameter. Therefore, two groups of simulations were carried out, each with a fixed value of the Morton number of respectively $\log(\text{Mo}) = -2.62$ and 0.37 . The first group has the same Mo number as the W-G 80% mixture. And the second group is similar to the W-G 95% mixture. In the experimental tests, the bubble length is different for each bubble. But, in the simulations the initial length of the bubble is fixed to $9r_o$.

The results are shown in Fig. 6.19. All three break up patterns are observed in Fig. 6.19(A). There is a small region where the bubble remains intact ($\epsilon < 1.4$, $20 \leq \text{Eo} \leq 40$). For higher values of the Eo number, but expansion ratios less than 1.4, small bubbles will be shed off at the tail of the bubble. The detachment will not affect the bubble main body. When $\epsilon > 1.4$ and $\text{Eo} \leq 60$, the bubble will break up by necking. For increasing Eo number, the recirculation at the rear of the bubble becomes stronger. The bubble tail will penetrate the entire bubble instead of cutting it in the middle.

Figure 6.19(B) shows the bubble break up pattern for $\log(\text{Mo}) = 0.37$. The detachment is not found in the present test region. The viscosity forces are relatively large, thus recirculation at the rear of the bubble is not significant. Bubble penetration can be observed when Eo is equal to 100. Overall, the dominant break-up pattern is necking.

6.3 Chapter conclusion

The Taylor bubble rising through the expansion has been investigated by means of experiments and simulations. The following conclusions can be drawn:

- The bubble velocity increases in the expansion. The bubble head velocity quickly reaches a new steady state. The bubble tail velocity shows strong oscillations, which disappear rapidly.

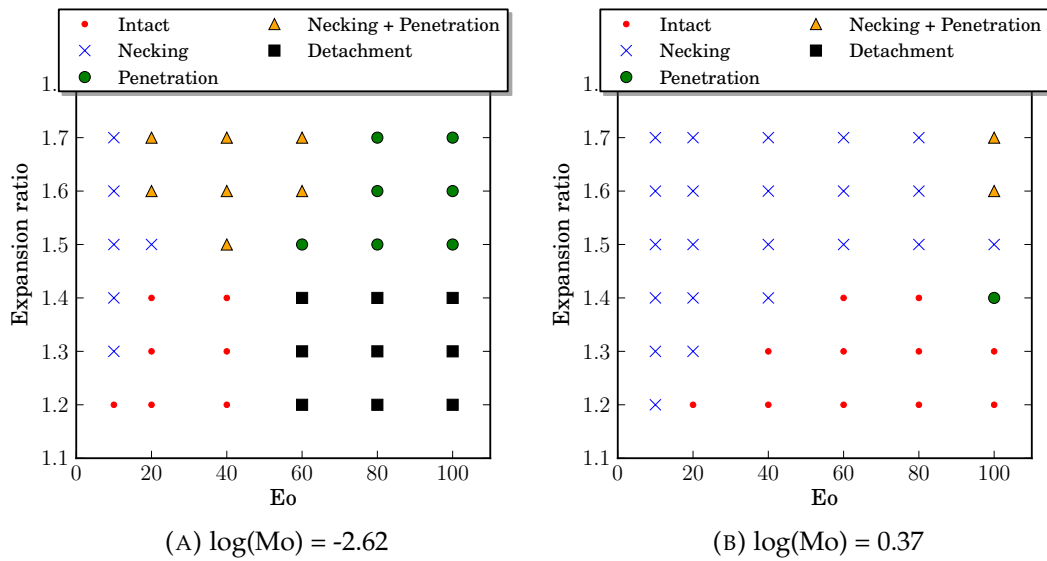


FIGURE 6.19: Bubble break-up regime map obtained by simulations.

- The time shift of the bubble in the expansion is positive. The bubble spends more time passing through the expansion than the results simply obtained without considering the effect of the expansion.
- The concave neck region always exists when the bubble passes the expansion. Increasing the expansion ratio will lead to a reduction of the bubble neck radius.
- Three bubble break-up patterns (necking, penetration, detachment) are observed in the experiments. A bubble break-up pattern map has been obtained from the numerical simulations for $\log(Mo) = -2.62$ and 0.37 .

Chapter 7

Bubble rising through contractions

In this chapter, we will discuss the bubble rising through contractions. The same numerical model is used for this purpose as the model described in Chapter 6. The simulation results are validated by experiments. First, we will discuss the bubble behaviors in the contraction. Then, the bubble blocking phenomena will be analyzed.

7.1 Model description

7.1.1 Simulations

The configuration of the numerical model is shown in Fig. 7.1. The diameter of the lower and upper tubes are D_o and D_c , respectively. Thus, the contraction ratio is given by $\epsilon = D_c/D_o$. The length of the upper tube is $8D_o$. The connection of the two tubes is the horizontal wall, which makes the connection a sudden contraction. The boundary conditions for the tube walls are Dirichlet conditions ($u = 0, v = 0$).

The description of the hydrodynamic features are similar to those defined in Chapter 6. The location of the contraction in the z direction is z_c . Other parameters are expressed in the same form as in Fig. 6.2.

7.1.2 Experiments

The contraction ratios in the experiments are listed in Table 7.1. Three contraction ratios have been tested, ranging from 0.93 to 0.69. The inner diameter of the lower tube (D_{in}^{lower}) corresponds to D_o in the simulation. And, the inner diameter of upper tube (D_{in}^{upper}) corresponds to D_c . The contraction ratio (ϵ) is equal to D_c/D_e .

TABLE 7.1: Diameters of the tubes.

Index	D_{in} (mm)	D_{out} (mm)	$\epsilon = D_{in}^{upper} / D_{in}^{lower}$
Lower tube			
1	16.40	20.00	
Upper tube			
1	15.00	18.90	0.93
2	13.10	17.10	0.81
3	11.10	15.00	0.69

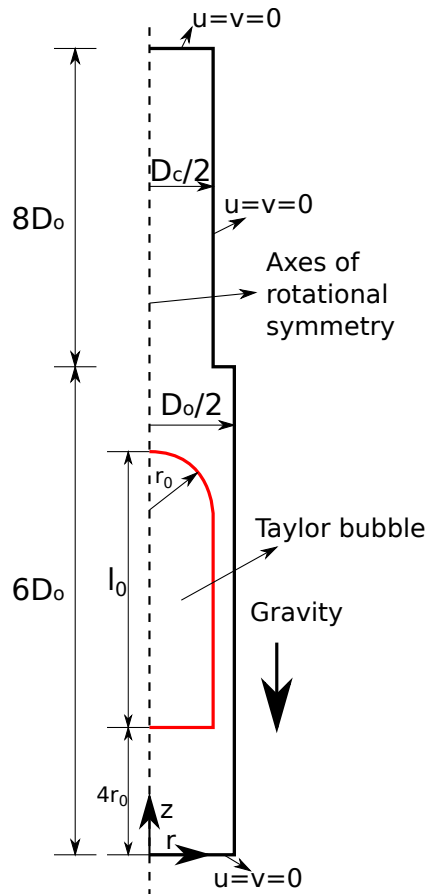


FIGURE 7.1: Initial configuration for the simulation.

7.2 Result analysis

7.2.1 Comparison of experiments and simulations

The bubble shape deformation in the contractions are shown in Fig. 7.2 to 7.6. The first row in each figure is the experimental data. The second row are the simulation results. A good agreement is found between simulations and experiments for all cases. The figures show the dynamic behavior of the bubbles passing through the contractions. When the bubble head reaches the expansion, the time is set to be the starting time ($t = 0.0$ s). Unlike the figures for the bubble passing through the expansion, we show also the bubble shape before encountering the contraction.

Figures 7.2, 7.3 and 7.4 show the bubbles in the W-G 70% mixture rising through the contractions with $\epsilon = 0.93, 0.81$ and 0.69 . The bubble has reached its terminal shape before entering the contraction. When it encounters the contraction, the bubble nose is squeezed into a smaller round shape to accommodate the diameter of the upper tube. The bubbles pass through the contractions for $\epsilon = 0.93$ and 0.81 , but for $\epsilon = 0.69$ the bubble is blocked by the contraction. The conditions in which the bubble is blocked will be discussed in more details in the following section.

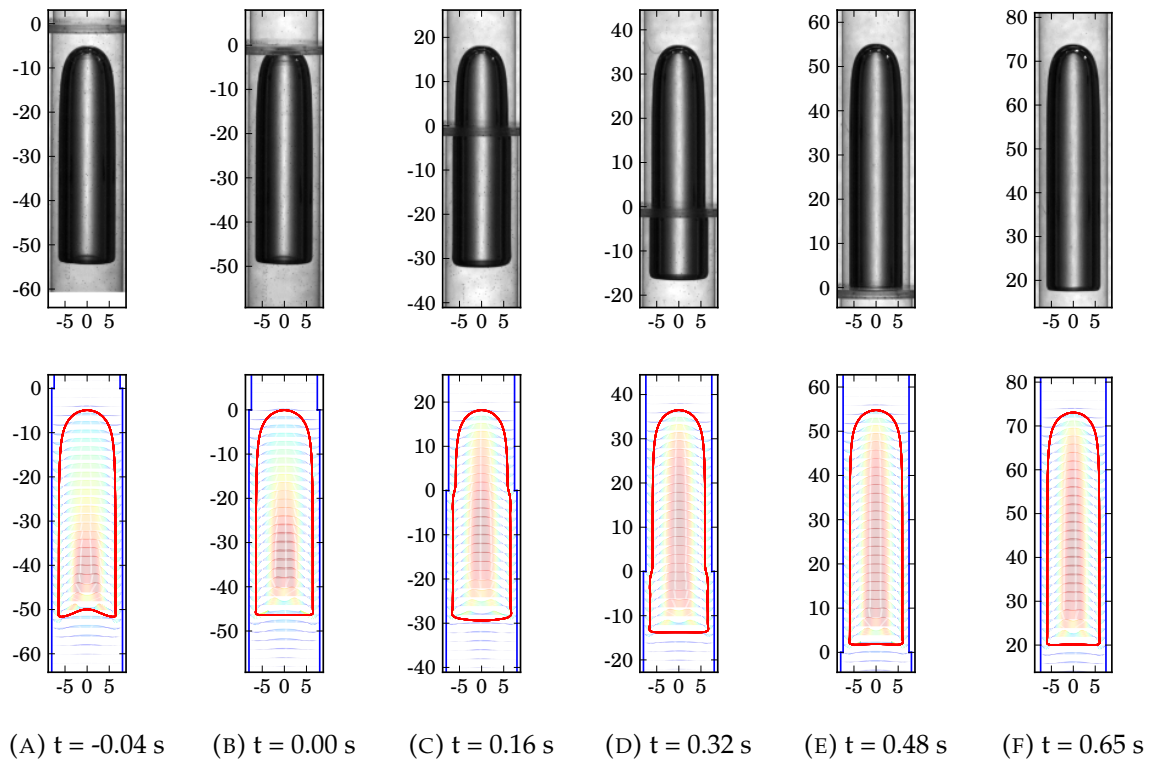


FIGURE 7.2: Experimental and numerical results of the bubble rising through a contraction ($W-G$ 70%, $Eo = 41.9$, $\log(Mo) = -3.65$, $\epsilon = 0.93$)

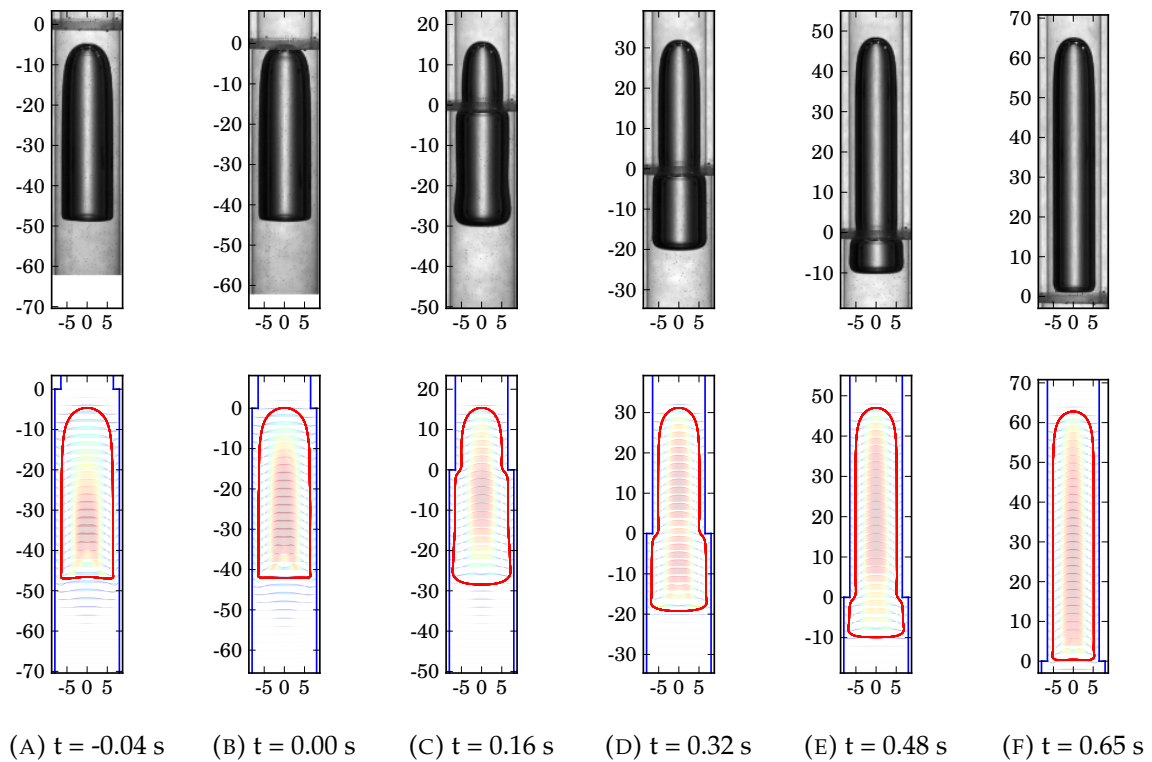


FIGURE 7.3: Experimental and numerical results of the bubble rising through a contraction ($W-G$ 70%, $Eo = 41.9$, $\log(Mo) = -3.65$, $\epsilon = 0.81$)

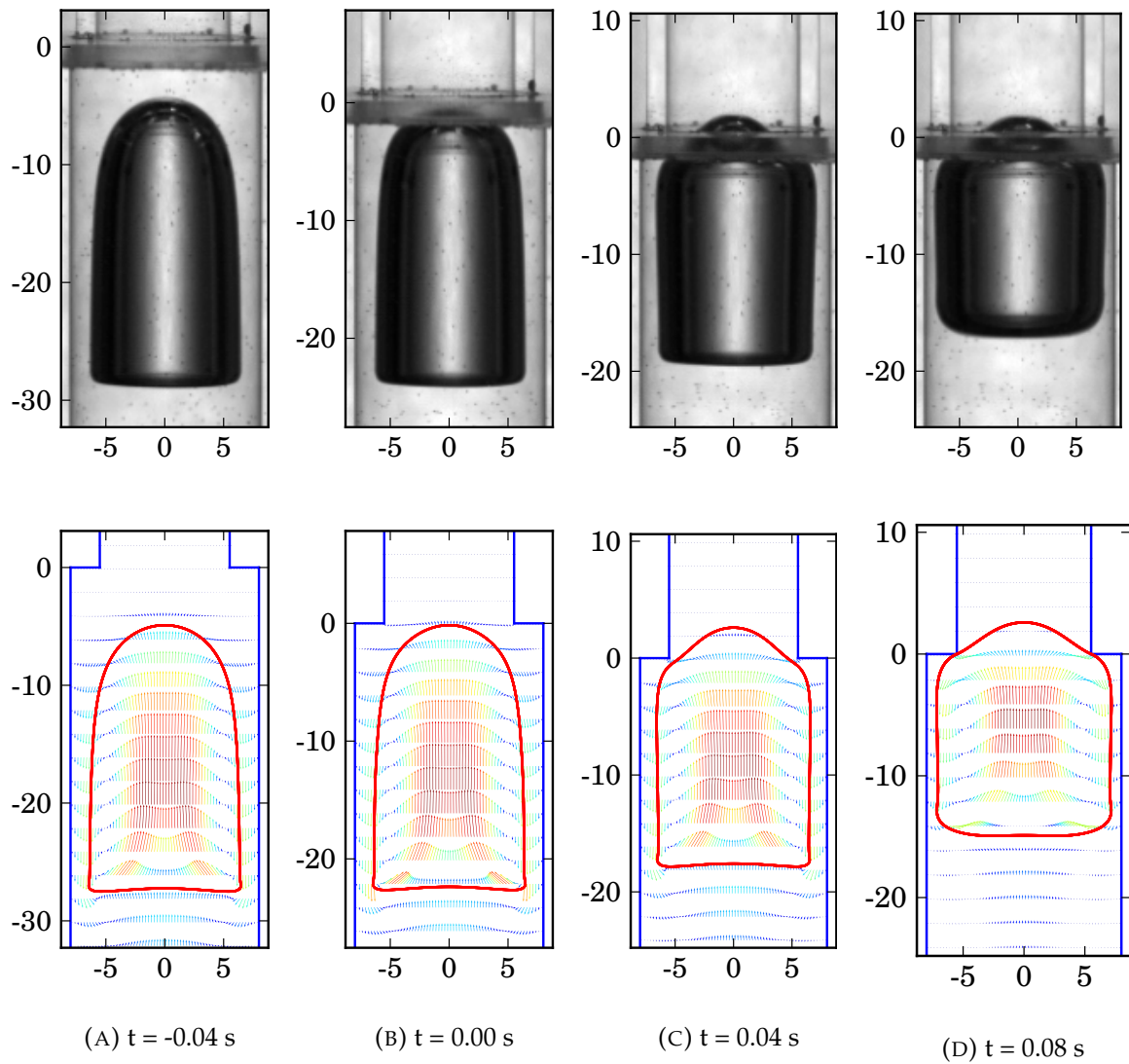


FIGURE 7.4: Experimental and numerical results of the bubble rising through the contraction (W-G 70%, $Eo = 41.9$, $\log(Mo) = -3.65$, $\epsilon = 0.69$)

Figures 7.3, 7.5 and 7.6 show the bubble rising in the W-G 60%, W-G 70% and W-G 80% mixtures. The contraction ratio ϵ is 0.81 for the 3 cases. For these cases, the bubble evolution is very similar. A small difference can be observed for the bubble in the W-G 60% fluid. When the bubble passes the contraction, capillary waves can be observed at the rear of the bubble. For the cases W-G 70% and W-G 80%, an oval tail shape can be observed. In the next section, a detailed discussion on the bubble velocity variation is presented based on the simulation results.

7.2.2 Velocity variation

Similar to the discussion in Section 6.2.1, we can obtain two terminal velocities, in the lower tube and in the upper tube. If the reference diameter is D_o , the dimensionless numbers for bubbles in the lower tube are $Eo_o = \rho_l g D_o^2 / \sigma$ and $Fr_o = V_T / \sqrt{g D_o}$. Similarly, we obtain the

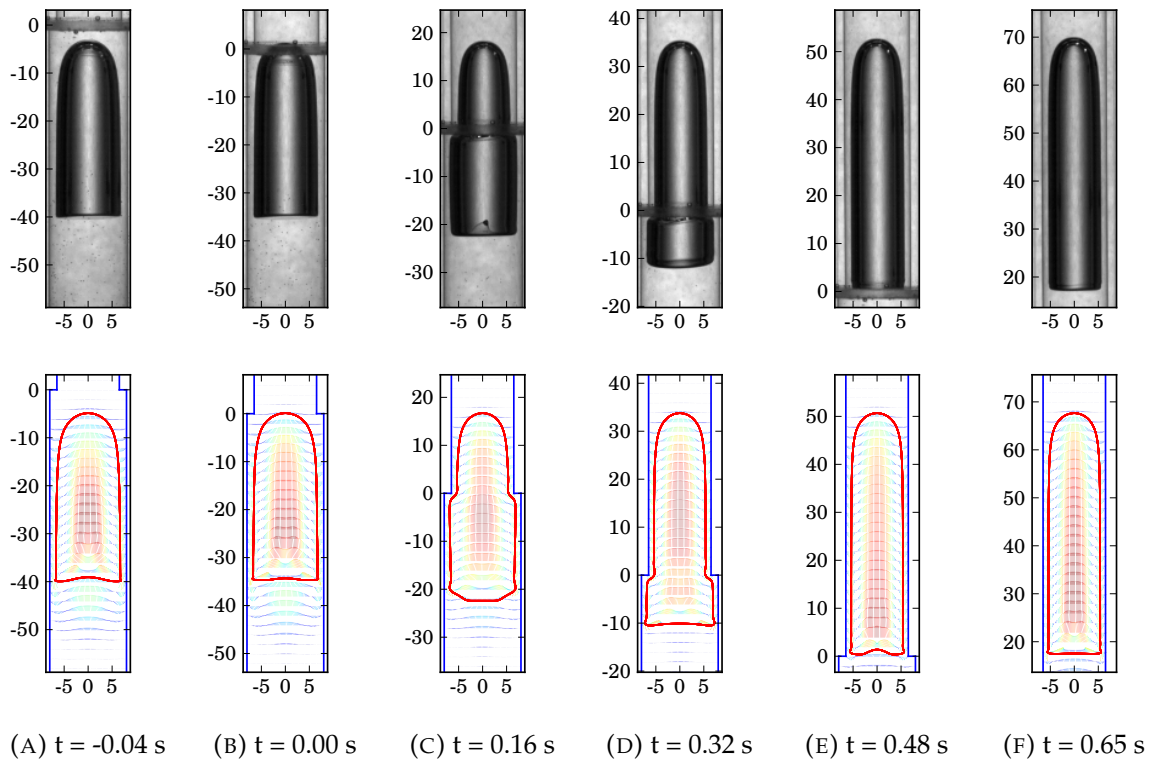


FIGURE 7.5: Experimental and numerical results of the bubble rising through the contraction (W-G 60%, $Eo = 40.6$, $\log(Mo) = -4.63$, $\epsilon = 0.81$)

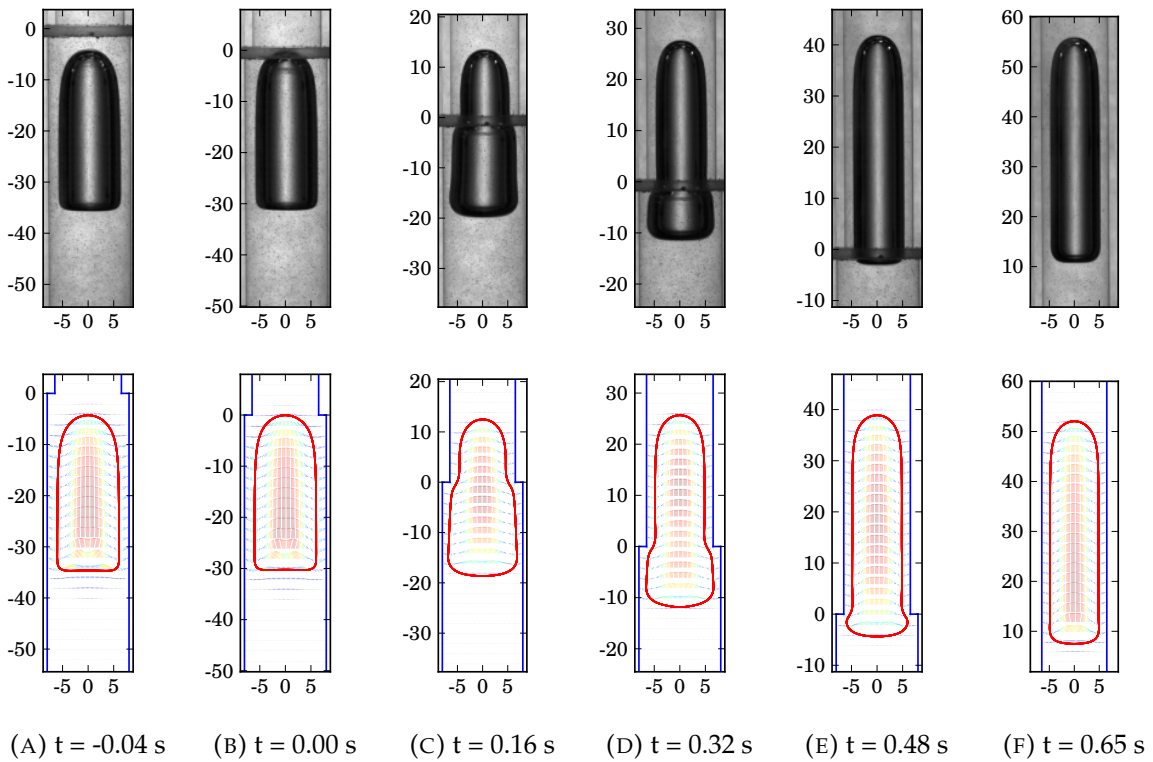


FIGURE 7.6: Experimental and numerical results of the bubble rising through the contraction (W-G 80%, $Eo = 47.5$, $\log(Mo) = -2.62$, $\epsilon = 0.81$)

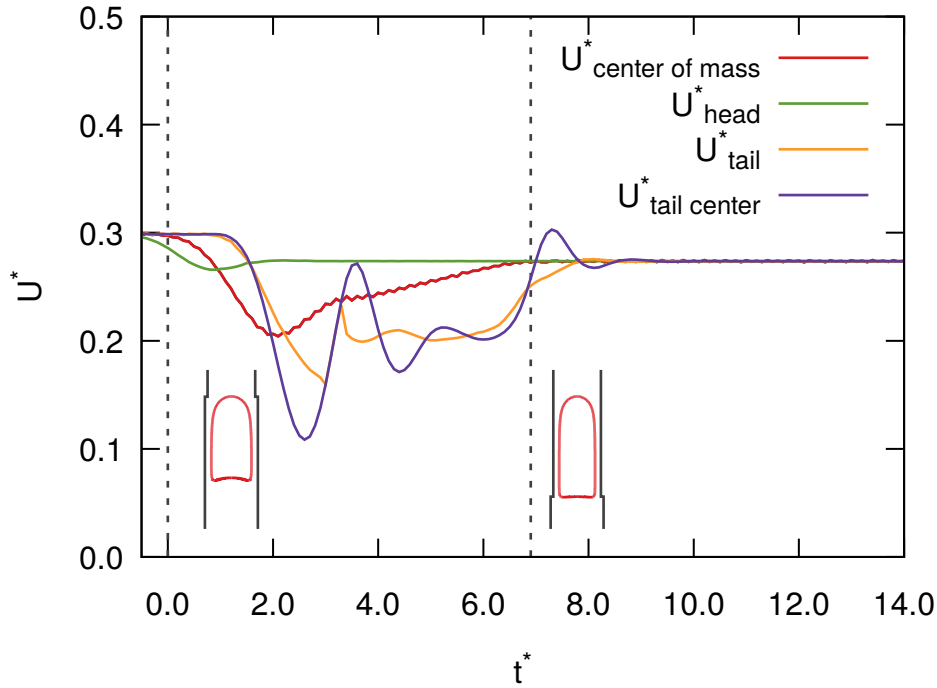


FIGURE 7.7: Evolution of the dimensionless bubble velocity from simulation as a function of the bubble head position at four locations of the bubble. The vertical dash lines mark the location of the bubble entering and leaving the contraction. The horizontal dash line indicates the bubble terminal velocity before entering the contraction. ($Mo = 1 \times 10^{-2}$, $Eo = 100$, contraction ratio = 0.9)

$Eo_c = \rho_l g D_c^2 / \sigma$ and $Fr_c = V_{Tc} / \sqrt{g D_c}$ as the dimensionless numbers for bubbles in the upper tube. Both Fr numbers (Fr_o and Fr_c) can be predicted by correlations such as Viana et al. [115].

The transient state of the bubble in the contraction can be observed from the velocity variations. Similar to the definitions in Section 6.2.1, the dimensionless velocity $U^* = U / \sqrt{g D_o}$ is plotted at four locations of the bubble: the tip of the head, the center of the tail, the tip of the tail and the center of mass. The evolution of the velocity at those four locations is shown in Fig. 7.7 as a function of the normalized time to the contraction (t^*). We consider $t^* = 0$ when the bubble head reaches the contraction. The two vertical dashed lines mark the instants the bubble nose and tail reach the contraction. The bubble head velocity begins to decelerate before reaching the contraction. This is simply due to the liquid ahead of the bubble blocked by the contraction. For the tail velocities, they begin to oscillate at $t^* \approx 0.5$, and decelerate even more than the velocity of the bubble head. These observations on the velocities may lead to the conclusion that the contraction does not induce any oscillation of the bubble surface.

Furthermore, we want to investigate whether the bubble initial length affects the transient velocity of the bubble in the contraction. Figure 7.8 shows the evolution of the bubble head and tail velocities for different values of the initial bubble length. The head velocity is independent of the initial bubble length. The tail velocity follow the same trend, but slightly shifted in time due to the different lengths of the bubbles.

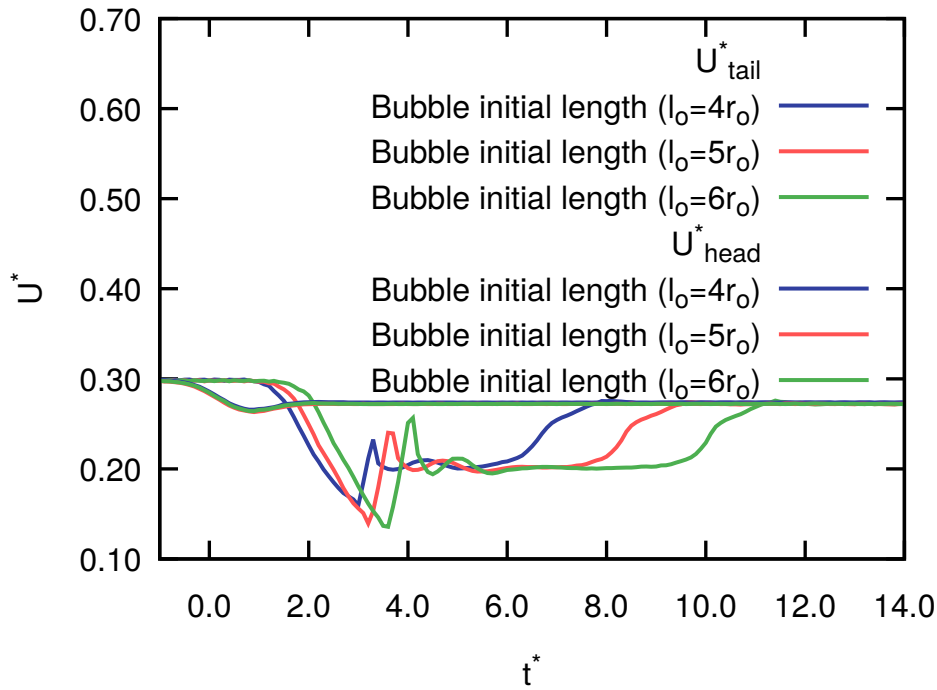


FIGURE 7.8: Evolution of the bubble head and tail velocity for different values of the initial bubble length. ($Mo = 1 \times 10^{-2}$, $Eo = 100$, contraction ratio = 0.9)

7.2.3 Bubble length variation

Figure 7.9 shows the bubble length variation ($Mo = 1$, $Eo = 100$) when it passes through the contraction for different contraction ratios. The initial bubble length for these tests are fixed at $l_o = 4r_o$. The variation can be divided into two stages. The first stage is reducing the length in the z direction. The bubble head takes some time to accommodate to the smaller diameter of the upper tube. The bubble will be squeezed in the z direction. Thus, the length will be reduced. In the second stage, a new bubble head shape formed in the upper tube. The bubble body continuously passes through the contraction. The bubble will be elongated in the smaller tube. Therefore, the bubble length increases.

7.2.4 Transition time of the bubble in the contraction

This section is similar to Section 6.2.1. The purpose is to investigate the time shift due to the effect of the contraction. Here, we define two lengths l_o and l_c which are the distances below and above the contraction (Fig. 7.10(A)). A simple calculation of the transitional time, based on the terminal velocities before and after the contraction, not accounting for the effect of the singularity, would be given by $l_o/U_o + l_c/U_c$, where U_o and U_c are the bubble terminal velocities in the upper and lower tubes respectively. The actual transition time will then be given by:

$$\Delta t = \frac{l_o}{U_o} + \frac{l_c}{U_c} + \Delta t_s$$

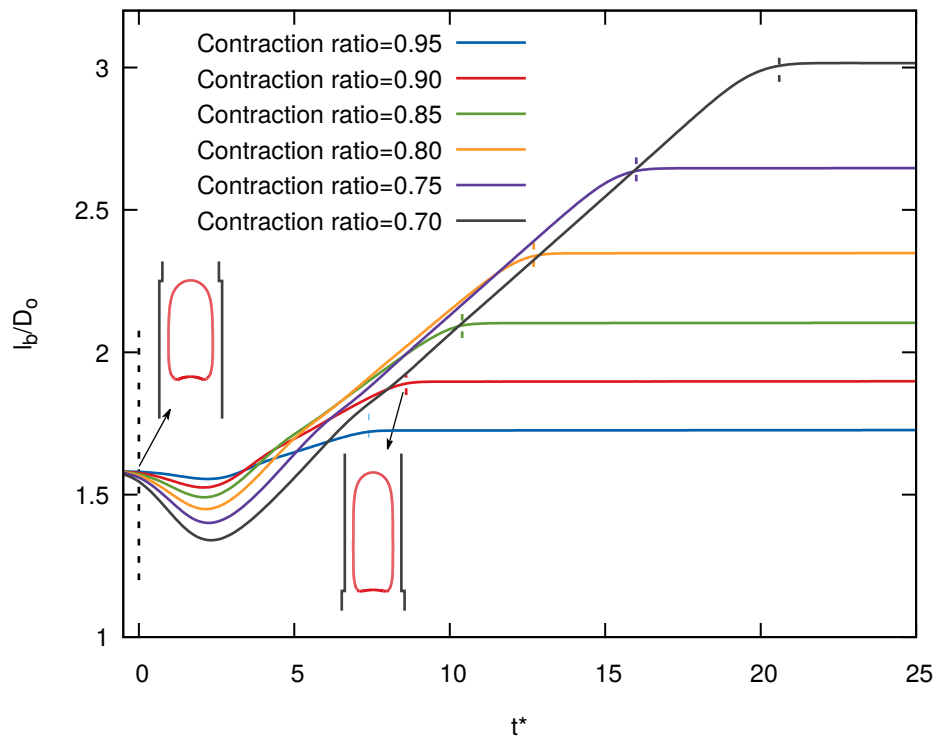


FIGURE 7.9: Evolution of the bubble length in different contraction ratio. ($Mo = 1$, $Eo = 100$)

where the time shift Δt_s is added to account for transition in the contraction. In the following, the time shift Δt_s is calculated for the bubble head velocity.

Figure 7.11 shows the time shift for different contraction ratios and Eo numbers. The values of the time shift are positive, which indicates that the contraction introduces a delay on the time of the bubble passing through the contraction. Increasing the Eo number, the time shifts in different contractions are reducing. The deformation of the bubble interfaces are facilitated when the Eo number is increasing, thereby reducing Δt_s . The contraction ratio has a strong influence on the time shift, in particular for smaller Eo numbers.

7.2.5 Bubble blocking

The bubble blocking phenomenon has been observed both in the experiments and simulations. When the contraction ratio is reduced, the bubble will be blocked by the contraction. We consider that the bubble is blocked by the contraction if the bubble head velocity reduces to zero when the bubble reaches the contraction. The investigation in this section focuses on the blocking phenomenon, but not on the bubble evolving after being blocked. In the experiments, the blocked bubble continuous to evolve. After a few seconds, it may break-up into small bubbles that pass through the contraction. This phenomenon may be due to the contact of the bubble interface with the edges of the upper tube. Nevertheless, the bubble stops at the contraction for at least a few seconds. In the simulation, the event of the bubble interface in contact with the tube edge is not properly taken into account. Simulation of the bubble deformation after blocking is therefore not pursued.

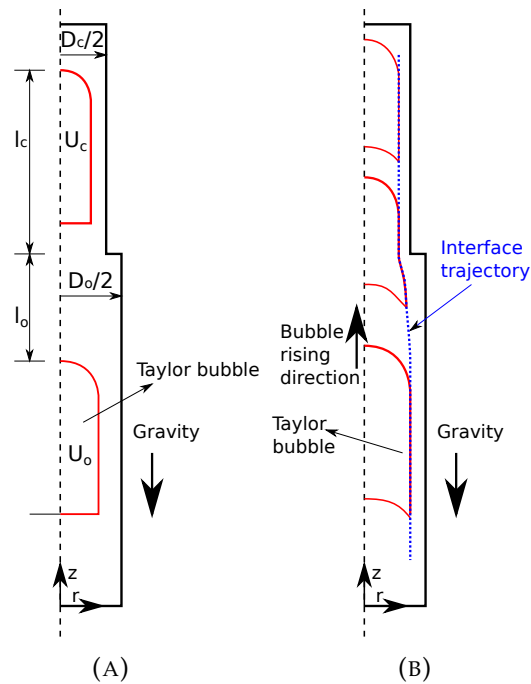


FIGURE 7.10: (A) Illustration of the transition time of the bubble in the contraction. (B) Illustration of the bubble interface trajectory.

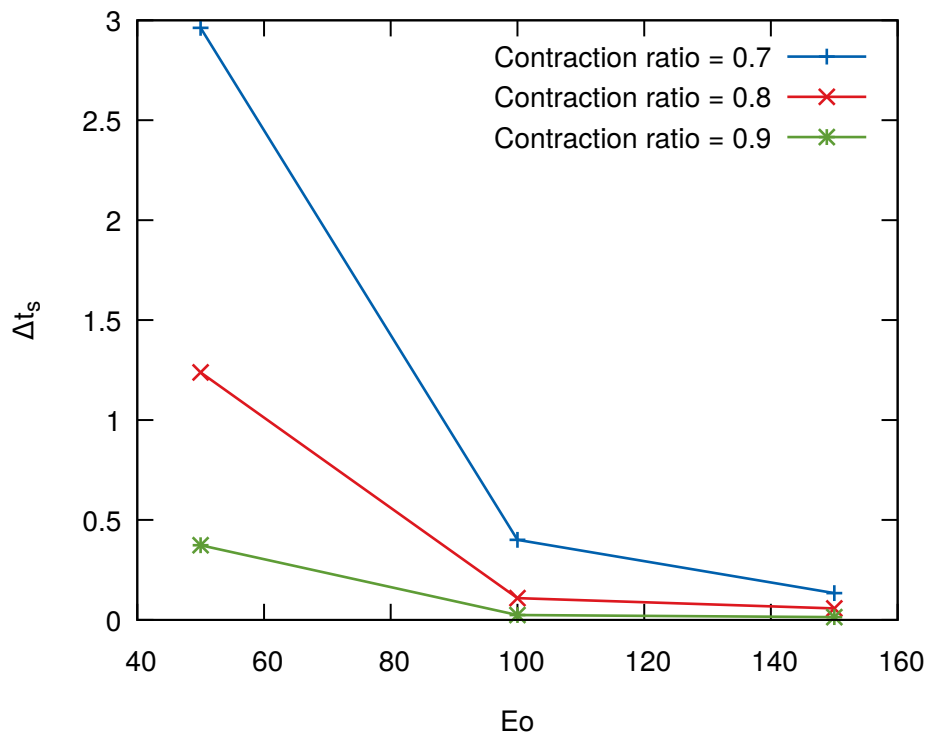


FIGURE 7.11: Time shift due to the effects of the contractions. ($Mo = 1 \times 10^{-2}$)

The direct reason of the bubble being blocked is that the bubble interface touches the tube edges and prevents the liquids flow from ahead of the bubble to its rear. When the bubble rises, there is always a passage way for liquid flow between the bubbles and the tube

wall. The illustration of the passage way is shown in Fig. 7.10(B). Figure 7.12 and 7.13 show this liquid passage way. At each moment, we can obtain one point which is the location of minimal distance from the bubble interface to the side tube wall. The trajectory of this point is the line in Fig. 7.12 and 7.13.

Figure 7.12 shows the bubble interface trajectory passing through the contraction ($\epsilon = 0.7$). The interface trajectories for different Eo numbers are close to each other. The Eo number has minor effect on this trajectory for $Eo > 100$. When $Eo = 100$, the trajectory is slightly close to the tube wall. If the trajectory touches the tube wall, the bubble will be blocked. The trend of the trajectory is shown in Figure 7.12 with different the Eo numbers. The reason that increasing the surface tension effects make the bubble difficult to deform when it encounters the contraction. The new bubble head shape can not accommodate to the diameter of the upper tube. The bubble head may reach the tube wall, then lead to blocking.

Figure 7.13 shows the bubble interface trajectory passing through different contractions ($\epsilon = 0.7, 7.5, 0.8$). In this test, $Eo = 50$, the bubble is blocked in the contraction where $\epsilon = 0.7$. When the contraction ratio increases, the bubble is able to pass through the contraction. A small changing of the contraction ratio $\Delta\epsilon = 0.05$ leads to large discrepancy on the bubble interface trajectory. Therefore, the tube geometry changing has major effects on the bubble blocking.

Two groups of tests have been carried out in order to find the critical contraction ratio of blocking. The contraction ratio ranges from 0.6 to 0.9. The values of the Eo number are less than 100. The Mo number for first group is close to the fluid with W-G 95%. The second group is close to the W-G 80% mixture. The initial bubble lengths are fixed to $4r_o$. The results are shown in Fig. 7.14. The two blocking regime maps are very similar. The variation of the Mo number has minor effect here on the bubble blocking. The tube diameter has a greater effect on the blocking of the bubble. If the contraction ratio and Mo number are fixed, the bubbles with smaller Eo number trend to be blocked. In the present tests, if the contraction ratio is less than 0.7, the bubble will be blocked.

7.3 Chapter conclusion

In this chapter, the Taylor bubble rising in contractions has been investigated. Three different contraction ratios have been tested in the experiments. The simulations showed similar results. A few conclusions can be drawn:

- The bubble velocity will be reduced in the contraction. The contraction will not introduce any bubble interface oscillations.
- The time shift of the bubble in the contraction is positive. The effect of the contraction on the bubble's transitional state is a delay of the bubble rising.
- The bubble blocking phenomenon is obtained in experiments and reproduced in our simulations. Extensive simulations in different conditions show that for a contraction ratios less than 0.7, the bubble will be blocked.

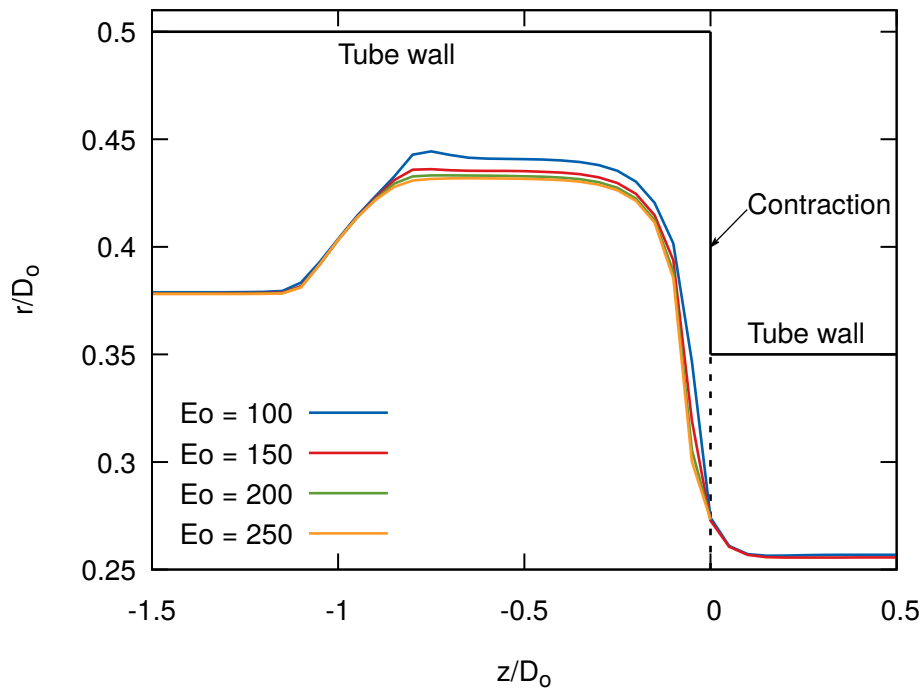


FIGURE 7.12: Bubble interface trajectory passing through the contraction. ($Mo = 1 \times 10^{-3}$, Contraction ratio = 0.7)

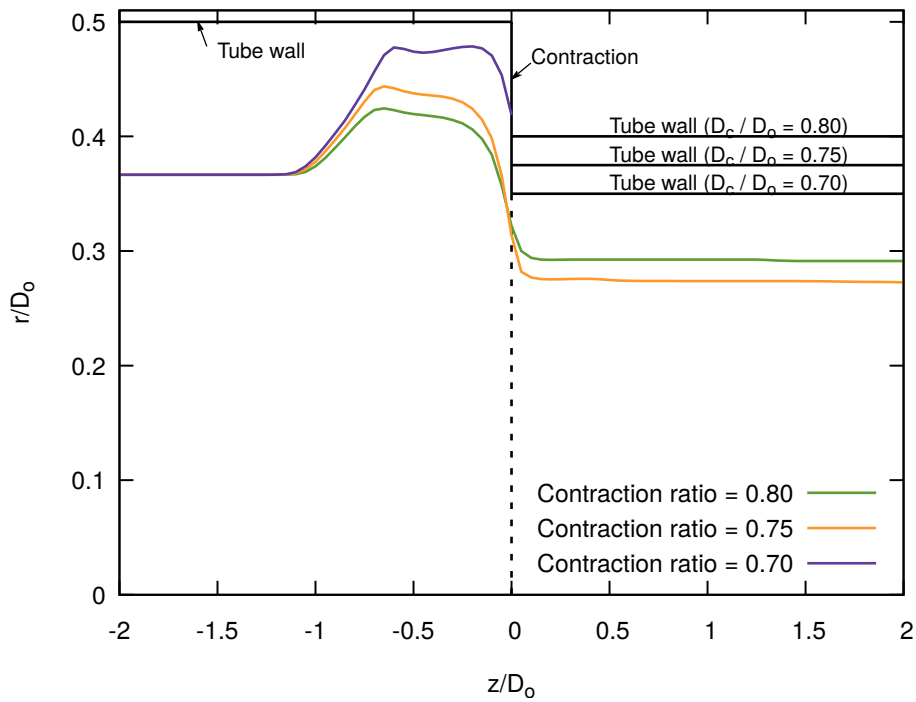


FIGURE 7.13: Bubble interface trajectory passing through the contraction. ($Mo = 1 \times 10^{-3}$, $Eo = 50$)

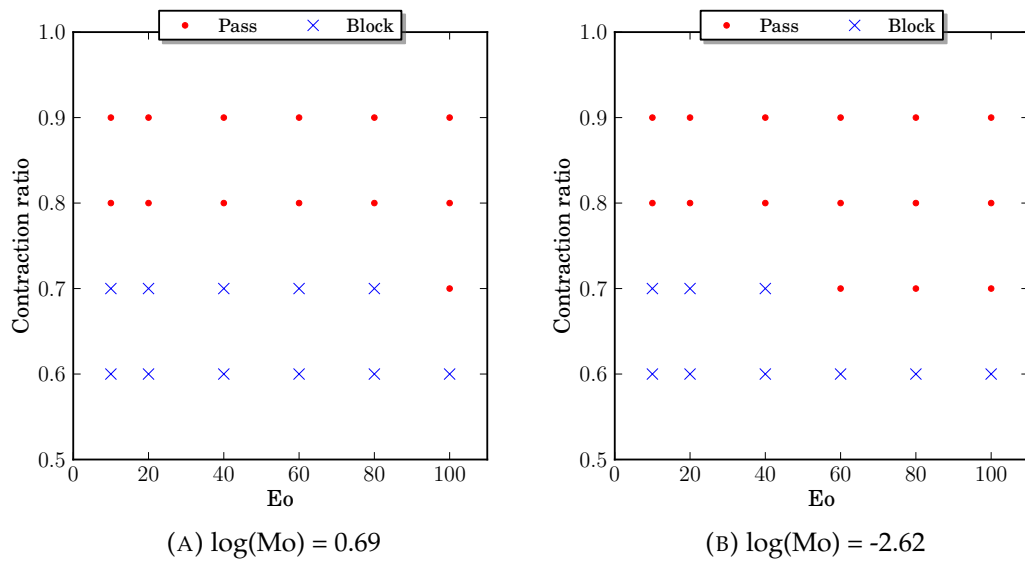


FIGURE 7.14: Bubble blocking regime map.

Chapter 8

Conclusions and perspectives

This chapter summarizes the conclusions drawn from this study together with the perspective for future work in this field.

8.1 Synthesis

The review presented in Chapter 2 showed the background literature on two-phase flow. In particular, we focused on the rise of Taylor bubbles. We clarify the flow patterns observed in two-phase flow in vertical channels. The slug flow is one of the four typical flow patterns, namely bubble flow, slug flow, churn flow and annular flow. An extensive review on the Taylor bubble has been carried out. The investigation about the Taylor bubble rising in the straight tube has been studied. Both the numerical and experimental studies have been devoted to this subject. But, the investigation about Taylor bubbles rising through expansions and contractions is very limited. The main objective of this study is to investigate the bubble transitional behaviors in the expansion and contraction.

In order to reach the main objective of this work, experimental and numerical tests have been carried out. Chapter 3 described the numerical model. The classical projection method is used for solving the governing equations. The Volume-of-fluid (VOF) method is adopted to present the interface of the bubble. A few test cases have been carried out to test the solver. The lid-driven cavity flow test shows that the convergence rates are close to second-order both for velocities and pressure. The single bubble rising test case showed that the solver can predict the bubble shape in a wide range of the Re and Bo number. Other test cases about the adaptive mesh refinement and parallelization are carried out to improve the efficiency of the calculation.

An experimental test bench has been established at the CETHIL laboratory. The details of the configuration are described in Chapter 4. The experimental apparatus proved to be effective for the present study. Images of the bubble rising through the expansions and contractions could be obtained with the high speed camera. A self designed algorithm is used for detecting the interface of the bubble in the images.

The Taylor bubble in straight tubes has been investigated in Chapter 5. A sensitivity analysis confirmed the parameters used in the simulations. We chose the experimental data of [118] and carried out a series of simulations. The results of the bubble terminal velocities are in good agreement with the experimental data and the correlations. A comparison of the simulations against the present experimental data have been carried out. The shape comparison

shows that the simulation could successfully predict the bubble shapes. We also find that the correlation of Llewellyn et al. [61] which predicts the bubble film thickness has the best agreement to the present experimental data.

The Taylor bubble rising through the expansion and contraction have been investigated in Chapter 6 and 7, respectively. The investigations are performed by the experiment and simulation. A detailed analysis is then performed is based on the numerical data.

8.2 Concluding remarks

The conclusions present here is about the bubble rising through the expansion and contraction, which are the main objective of the present study. These conclusions are as follows:

- The visual comparison shows good agreement between the experimental and numerical data. The concave shape at the tail of the bubble could be successfully captured by the simulations. The recirculation at the tail of the bubble pushes the bottom into the bubble and forms the concave shape. The interface moving inward can be observed on the experimental images, but it is difficult to detect the interface. However, the simulation could show the interface of the bubble tail very clear.
- The bubble velocity increases in the expansion. On contrary, the bubble velocity decreases in the contraction. The bubble head velocity reaches a new steady state very quickly. The bubble tail shows oscillations.
- The time shift of the bubble in both expansion and contraction are positive. The bubble spends more time passing through the singularity than the results simply obtained without considering the effect of the expansion/contraction.
- Three bubble break-up patterns (necking, penetration, detachment) are observed when the bubble passes through the expansion. A bubble break-up pattern map has been obtained from the numerical simulation.
- The bubble blocking phenomenon is observed in the experiment. The simulation could reproduce the same phenomenon. Extensive simulations in different conditions show that the bubble will be blocked if the contraction ratio is less than 0.7. The surface tension also has effect on this phenomenon. The bubble tends to be blocked when increasing the surface tension force.

8.3 Perspectives

The experiments carried out in this study have been successfully predicted by the present numerical data. However, further research definitely needs to be carried out. Specific areas that should be given priority for future works are suggested below:

- There are other geometry parameters of the singularities that need to be investigated. For example, the gradual expansion or contraction. In order to further study the effect

of these parameters on the bubble, more experimental or numerical simulations need to be carried out.

- Specific numerical methods are needed to calculate the bubble interface contact with the tube wall. In our simulation, when the bubble is blocked by the contraction and the interface touches the tube wall, the solver could lead to divergent results. A new algorithm is needed to consider the situation that the bubble interface contacts with the tube wall.
- PIV experiments could be performed to compare with the velocity fields obtained by simulation. Extension of this work towards pressure driven flow can be also an interesting perspective. Actually, such flow is closer to the heat-to-power or power-to-heat applications.

Appendix A

Comparison of the bubble rising test cases

In order to compare the benchmark results obtained by Gerris with that of in the literature, we list the results in the same way as in the [3] and [48].

A.1 Results

The relative error norms for the circularity, center of mass, and rise velocity together with the estimated ROC are shown in Table A.1. The reference solution is the one from the computation on the finest grid ($h = 1/256$). Similar results of the test case 2 are shown in Table A.2.

Furthermore, we list the minimum circularity and maximum rise velocity, with corresponding incidence times and final position of the center of mass, see Table A.3 and A.4. In order to compare with the results in [3], we restricted the comparison within the time interval from 0 to 2 for case 2.

TABLE A.1: Relative error norms and convergence orders for test case 1

1/h	$\ e\ _1$	ROC ₁	$\ e\ _2$	ROC ₂	$\ e\ _\infty$	ROC _∞
Circularity						
16	2.91E-02		4.43E-02		1.47E-01	
32	4.09E-03	2.83	5.55E-03	3.00	3.05E-02	2.27
64	1.20E-03	1.77	1.60E-03	1.79	7.35E-03	2.05
128	3.18E-04	1.91	4.50E-04	1.83	2.95E-03	1.32
Center of mass						
16	4.01E-03		5.11E-03		9.91E-03	
32	6.32E-04	2.66	7.33E-04	2.80	1.07E-03	3.21
64	1.36E-04	2.21	1.66E-04	2.14	2.51E-04	2.09
128	1.50E-04	-0.14	1.98E-04	-0.25	2.86E-04	-0.19
Rising velocity						
16	2.10E-02		2.20E-02		3.02E-02	
32	3.08E-03	2.77	4.02E-03	2.45	1.33E-02	1.18
64	1.59E-03	0.95	2.41E-03	0.74	1.40E-02	-0.06
128	9.25E-04	0.78	2.12E-03	0.19	1.28E-02	0.12

TABLE A.2: Relative error norms and convergence orders for Test Case 2

1/h	$\ e\ _1$	ROC ₁	$\ e\ _2$	ROC ₂	$\ e\ _\infty$	ROC _∞
Circularity						
16	1.76E-02		2.24E-02		6.13E-02	
32	1.05E-02	0.75	1.54E-02	0.54	3.54E-02	0.79
64	7.01E-03	0.58	1.39E-02	0.15	4.39E-02	-0.31
128	3.84E-03	0.87	7.19E-03	0.95	2.35E-02	0.90
Center of mass						
16	1.49E-02		2.01E-02		3.43E-02	
32	8.61E-03	0.79	1.26E-02	0.68	2.21E-02	0.63
64	4.12E-03	1.07	6.24E-03	1.01	1.18E-02	0.90
128	1.68E-03	1.29	2.32E-03	1.43	3.73E-03	1.66
Rising velocity						
16	9.05E-02		1.08E-01		1.81E-01	
32	4.87E-02	0.89	6.09E-02	0.82	9.86E-02	0.88
64	2.42E-02	1.01	3.26E-02	0.90	6.45E-02	0.61
128	7.60E-03	1.67	9.75E-03	1.74	2.06E-02	1.65

TABLE A.3: Minimum circularity and maximum rise velocity, with corresponding incidence times and final position of the center of mass for test case 1

1/h	C_{min}	$t _{C=C_{min}}$	V_{max}	$t _{V=V_{max}}$	$y_c(t=3)$
16	0.2404	0.88	0.7691	2.51	1.0933
32	0.2418	0.94	0.8880	1.69	1.0835
64	0.2422	0.92	0.8968	1.94	1.0826
128	0.2423	0.92	0.8995	1.85	1.0829
256	0.2425	0.92	0.9003	1.92	1.0826

TABLE A.4: Minimum circularity and maximum rise velocity, with corresponding incidence times and final position of the center of mass for test case 2

1/h	C_{min}	$t _{C=C_{min}}$	V_{max}	$t _{V=V_{max}}$	$y_c(t=2)$
16	0.6532	2.00	0.2524	0.92	1.0964
32	0.6617	2.00	0.2485	0.68	1.1102
64	0.6854	2.00	0.2505	0.71	1.1219
128	0.6899	2.00	0.2505	0.74	1.1310
256	0.6929	2.00	0.2508	0.73	1.1353

A.2 Comparison

We plot the three quantities in Table A.3, A.4 and compare them with the results in [3] and [48] in Fig. A.1, A.2 and A.3.

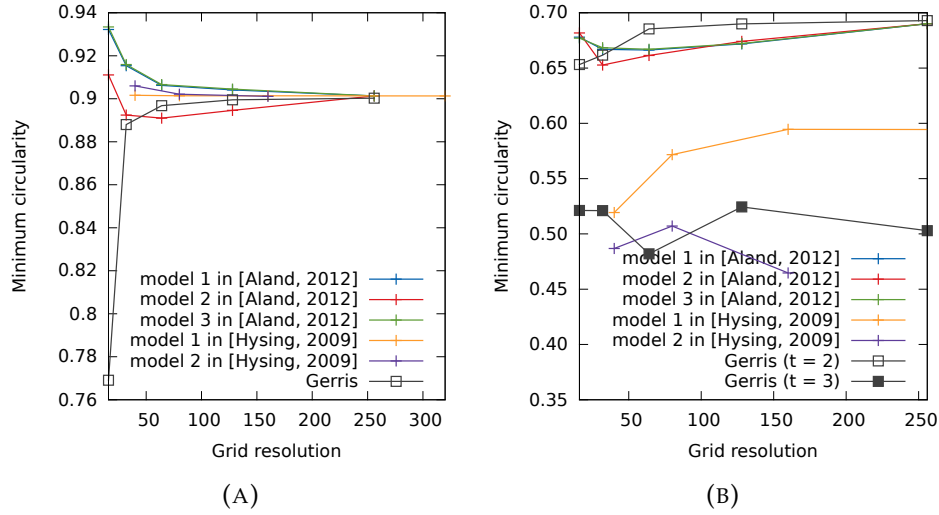


FIGURE A.1: Comparison of the minimum circularity. (A) case 1. (B) case 2.

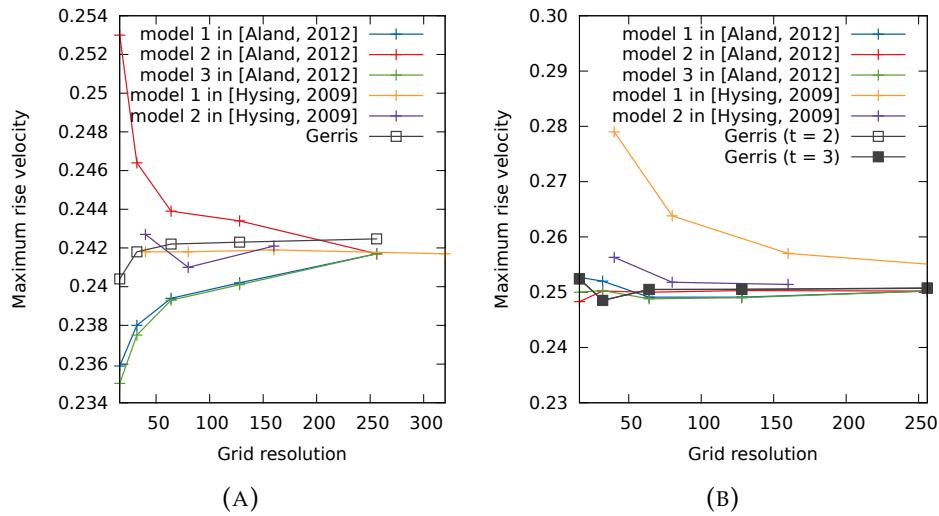


FIGURE A.2: Comparison of the maximum rise velocity. (A) case 1. (B) case 2.

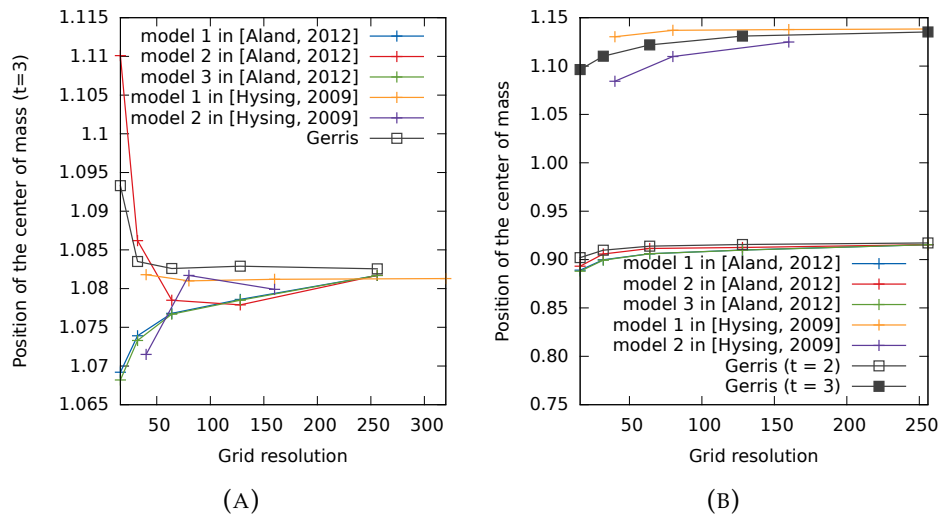


FIGURE A.3: Comparison of the final center of mass. (A) case 1. (B) case 2.

Appendix B

Nomenclature

A	cross-section area	m^2
c	Volume of fluid function (color function)	
D	tube diameter	m
e	error	
F	force	N
g	gravity acceleration	$\text{m} \cdot \text{s}^{-2}$
l	length	m
J	superficial velocities	$\text{m} \cdot \text{s}^{-1}$
p	pressure	Pa
R	radius	m
\dot{Q}	volumetric flow rates	$\text{m}^3 \cdot \text{s}^{-1}$
V_T	terminal velocity	$\text{m} \cdot \text{s}^{-1}$
U	bubble rise velocity	$\text{m} \cdot \text{s}^{-1}$

Abbreviations

AMR	Adaptive mesh refinement
ROC	rates of convergence
MAE	mean absolute error
MRE	mean relative error
VOF	Volume of fluid
W-G	water-glycerol

Dimensionless numbers

Bo	Bond number
Eo	Eötvös number
Fr	Froude number
Mo	Morton number
N_f	inverse viscosity number
Re	Reynolds number

Greeks

ϵ	Diameter ratio	
ϕ	level set function	
μ	dynamic viscosity	$\text{Pa} \cdot \text{s}$
ρ	density	$\text{kg} \cdot \text{m}^{-3}$

κ	curvature of the interface	m^{-1}
λ	film thickness	m
σ	surface tension	$\text{N} \cdot \text{m}^{-1}$
θ	inclination angle	rad

Sub and superscripts

<i>c</i>	contraction
<i>C</i>	continuous phase
<i>b</i>	bubble
<i>D</i>	disperse phase
<i>e</i>	expansion
<i>l</i>	liquid
<i>g</i>	gas
<i>h</i>	head or nose
<i>o</i>	original or initial
<i>r</i>	radial direction
<i>t</i>	tail
<i>out</i>	outside
<i>in</i>	inside
<i>upper</i>	upper
<i>lower</i>	lower
<i>z</i>	coordinate direction

Bibliography

- [1] F.F. Abdelall et al. "Pressure drop caused by abrupt flow area changes in small channels". In: *Experimental Thermal and Fluid Science* 29.4 (2005), pp. 425–434. ISSN: 0894-1777 (cit. on p. 27).
- [2] Gilou Agbaglah et al. "Parallel simulation of multiphase flows using octree adaptivity and the volume-of-fluid method". In: *High Performance Computing Le Calcul Intensif* 339.2 (2011), pp. 194–207. ISSN: 1631-0721 (cit. on pp. 39, 52).
- [3] S. Aland and A. Voigt. "Benchmark computations of diffuse interface models for two-dimensional bubble dynamics". In: *International Journal for Numerical Methods in Fluids* 69.3 (2012), pp. 747–761. ISSN: 1097-0363 (cit. on pp. 40, 43–45, 121, 123).
- [4] Ann S. Almgren, John B. Bell, and William G. Szymczak. "A numerical method for the incompressible Navier-Stokes equations based on an approximate projection". In: *SIAM Journal on Scientific Computing* 17.2 (1996), pp. 358–369 (cit. on p. 35).
- [5] Stephen Ambrose et al. "Numerical modelling of the rise of Taylor bubbles through a change in pipe diameter". In: *Computers & Fluids* 148 (2017), pp. 10–25 (cit. on p. 27).
- [6] P. Angeli and A. Gavriilidis. "Hydrodynamics of Taylor flow in small channels: a review". In: *Proceedings of the Institution of Mechanical Engineers, Part C: Journal of Mechanical Engineering Science* 222.5 (2008), pp. 737–751 (cit. on p. 16).
- [7] S. Aoyama et al. "Shapes of ellipsoidal bubbles in infinite stagnant liquids". In: *International Journal of Multiphase Flow* 79 (Mar. 2016), pp. 23–30. ISSN: 0301-9322 (cit. on p. 8).
- [8] J.D.P. Araujo, J.M. Miranda, and J.B.L.M. Campos. "Flow of two consecutive Taylor bubbles through a vertical column of stagnant liquid - A CFD study about the influence of the leading bubble on the hydrodynamics of the trailing one". In: *Chemical Engineering Science* 97.0 (2013), pp. 16–33. ISSN: 0009-2509 (cit. on p. 25).
- [9] J.D.P. Araujo, J.M. Miranda, and J.B.L.M. Campos. "Simulation of slug flow systems under laminar regime: Hydrodynamics with individual and a pair of consecutive Taylor bubbles". In: *Journal of Petroleum Science and Engineering* 111.0 (Nov. 2013), pp. 1–14. ISSN: 0920-4105 (cit. on p. 25).
- [10] J.D.P. Araujo et al. "Wide-ranging survey on the laminar flow of individual Taylor bubbles rising through stagnant Newtonian liquids". In: *International Journal of Multiphase Flow* 43.0 (2012), pp. 131–148. ISSN: 0301-9322 (cit. on pp. 17, 23, 25, 77, 85, 86).
- [11] Glycerine Producers' Association and others. *Physical properties of glycerine and its solutions*. Glycerine Producers' Association, 1963 (cit. on p. 61).

- [12] E. Aulisa et al. "Interface reconstruction with least-squares fit and split advection in three-dimensional Cartesian geometry". In: *Journal of Computational Physics* 225.2 (2007), pp. 2301–2319. ISSN: 0021-9991 (cit. on p. 37).
- [13] T. Balakhrisna et al. "Oil-water flows through sudden contraction and expansion in a horizontal pipe - Phase distribution and pressure drop". In: *International Journal of Multiphase Flow* 36.1 (Jan. 2010), pp. 13–24. ISSN: 0301-9322 (cit. on p. 28).
- [14] Guy Barr. "XXXI. The air-bubble viscometer". In: *The London, Edinburgh, and Dublin Philosophical Magazine and Journal of Science* 1.2 (1926), pp. 395–405 (cit. on p. 21).
- [15] John B Bell, Phillip Colella, and Harland M Glaz. "A second-order projection method for the incompressible navier-stokes equations". In: *Journal of Computational Physics* 85.2 (1989), pp. 257–283. ISSN: 0021-9991 (cit. on p. 35).
- [16] John B Bell and Daniel L Marcus. "A second-order projection method for variable-density flows". In: *Journal of Computational Physics* 101.2 (1992), pp. 334–348. ISSN: 0021-9991 (cit. on p. 35).
- [17] Kjell H. Bendiksen. "On the motion of long bubbles in vertical tubes". In: *International Journal of Multiphase Flow* 11.6 (Nov. 1985), pp. 797–812. ISSN: 0301-9322 (cit. on pp. 19, 21).
- [18] Dahya Bhaga and M. E. Weber. "Bubbles in viscous liquids: shapes, wakes and velocities". In: *Journal of Fluid Mechanics* 105 (1981), pp. 61–85 (cit. on pp. 5–7).
- [19] Q.C. Bi and T.S. Zhao. "Taylor bubbles in miniaturized circular and noncircular channels". In: *International Journal of Multiphase Flow* 27.3 (Mar. 2001), pp. 561–570. ISSN: 0301-9322 (cit. on p. 21).
- [20] O. Botella and R. Peyret. "Benchmark spectral results on the lid-driven cavity flow". In: *Computers & Fluids* 27.4 (1998), pp. 421–433. ISSN: 0045-7930 (cit. on p. 40).
- [21] E. Bouche et al. "The role of large bubbles detected from acoustic measurements on the dynamics of Erta 'Ale lava lake (Ethiopia)". In: *Earth and Planetary Science Letters* 295.1 (2010), pp. 37–48. ISSN: 0012-821X (cit. on pp. 29, 30).
- [22] J.U Brackbill, D.B Kothe, and C Zemach. "A continuum method for modeling surface tension". In: *Journal of Computational Physics* 100.2 (1992), pp. 335–354. ISSN: 0021-9991 (cit. on pp. 8, 37).
- [23] F. P. Bretherton. "The motion of long bubbles in tubes". In: *Journal of Fluid Mechanics* 10.2 (1961), pp. 166–188 (cit. on p. 21).
- [24] David L. Brown, Ricardo Cortez, and Michael L. Minion. "Accurate Projection Methods for the Incompressible Navier-Stokes Equations". In: *Journal of Computational Physics* 168.2 (2001), pp. 464–499. ISSN: 0021-9991 (cit. on p. 35).
- [25] R. A. S. Brown. "The mechanics of large gas bubbles in tubes: I. Bubble velocities in stagnant liquids". In: *The Canadian Journal of Chemical Engineering* 43.5 (1965), pp. 217–223 (cit. on pp. 22, 23).

- [26] J.D. Bugg, K. Mack, and K.S. Rezkallah. "A numerical model of Taylor bubbles rising through stagnant liquids in vertical tubes". In: *International Journal of Multiphase Flow* 24.2 (Mar. 1998), pp. 271–281. ISSN: 0301-9322 (cit. on pp. 24, 25, 69).
- [27] J.D. Bugg and G.A. Saad. "The velocity field around a Taylor bubble rising in a stagnant viscous fluid: numerical and experimental results". In: *International Journal of Multiphase Flow* 28.5 (2002), pp. 791–803. ISSN: 0301-9322 (cit. on pp. 23, 26).
- [28] JBLM Campos and J. R. F. Carvalho. "An experimental study of the wake of gas slugs rising in liquids". In: *Journal of Fluid Mechanics* 196 (1988), pp. 27–37 (cit. on pp. 23, 31).
- [29] Ing Youn Chen et al. "Two-phase flow pressure change subject to sudden contraction in small rectangular channels". In: *International Journal of Multiphase Flow* 35.3 (Mar. 2009), pp. 297–306. ISSN: 0301-9322 (cit. on p. 27).
- [30] Alexandre Joel Chorin. "Numerical solution of the Navier-Stokes equations". In: *Mathematics of computation* 22.104 (1968), pp. 745–762 (cit. on p. 34).
- [31] Alexandre Joel Chorin. "On the convergence of discrete approximations to the Navier-Stokes equations". In: *Mathematics of Computation* 23.106 (1969), pp. 341–353 (cit. on p. 34).
- [32] Sharen J. Cummins, Marianne M. Francois, and Douglas B. Kothe. "Estimating curvature from volume fractions". In: *Frontier of Multi-Phase Flow Analysis and Fluid-Structure* *Frontier of Multi-Phase Flow Analysis and Fluid-Structure* 83.6 (2005), pp. 425–434. ISSN: 0045-7949 (cit. on p. 38).
- [33] R. M. Davies and Geoffrey Taylor. "The mechanics of large bubbles rising through extended liquids and through liquids in tubes". In: *Proceedings of the Royal Society of London. Series A. Mathematical and Physical Sciences* 200.1062 (1950), pp. 375–390 (cit. on pp. 16, 18).
- [34] R Delfos, C.J Wisse, and R.V.A Oliemans. "Measurement of air-entrainment from a stationary Taylor bubble in a vertical tube". In: *International Journal of Multiphase Flow* 27.10 (Oct. 2001), pp. 1769–1787. ISSN: 0301-9322 (cit. on p. 31).
- [35] R. Delfos et al. "Measurement of the re-coalescence flux into the rear of a Taylor bubble". In: *Physics of Fluids* 13.5 (2001), pp. 1141–1150 (cit. on p. 31).
- [36] Ernest O Doebelin and Dhanesh N Manik. "Measurement systems: application and design". In: (2007) (cit. on p. 59).
- [37] A. E. Dukler and Olaf P. Bergelin. "Characteristics of flow-in falling liquid films". In: *Chemical Engineering Progress* 48.11 (1952), pp. 557–563 (cit. on p. 22).
- [38] Dumitru Theodor Dumitrescu. "Strömung an einer Luftblase im senkrechten Rohr". In: *ZAMM-Journal of Applied Mathematics and Mechanics/Zeitschrift für Angewandte Mathematik und Mechanik* 23.3 (1943), pp. 139–149 (cit. on pp. 16, 18, 23).
- [39] J. Fabre and A. Liné. "Modeling of two-phase slug flow". In: *Annual review of fluid mechanics* 24.1 (1992), pp. 21–46 (cit. on p. 17).

- [40] Stanley Osher Ronald Fedkiw. "Level set methods and dynamic implicit surfaces". In: (2003) (cit. on p. 9).
- [41] James Q Feng. "Buoyancy-driven motion of a gas bubble through viscous liquid in a round tube". In: *Journal of Fluid Mechanics* 609 (2008), pp. 377–410 (cit. on pp. 25, 78).
- [42] T. Funada et al. "Ellipsoidal model of the rise of a Taylor bubble in a round tube". In: *International Journal of Multiphase Flow* 31.4 (2005), pp. 473–491. ISSN: 0301-9322 (cit. on p. 21).
- [43] UKNG Ghia, Kirti N. Ghia, and C. T. Shin. "High-Re solutions for incompressible flow using the Navier-Stokes equations and a multigrid method". In: *Journal of computational physics* 48.3 (1982), pp. 387–411 (cit. on pp. 39–41).
- [44] K. Hayashi, R. Kurimoto, and A. Tomiyama. "Terminal velocity of a Taylor drop in a vertical pipe". In: *International Journal of Multiphase Flow* 37.3 (2011), pp. 241–251. ISSN: 0301-9322 (cit. on pp. 17, 21, 32, 77, 83).
- [45] Kosuke Hayashi, Ryo Kurimoto, and Akio Tomiyama. "Dimensional analysis of terminal velocity of a Taylor bubble in a vertical pipe". In: *Multiphase Science and Technology* 22.3 (2010) (cit. on p. 18).
- [46] C.W Hirt and B.D Nichols. "Volume of fluid (VOF) method for the dynamics of free boundaries". In: *Journal of Computational Physics* 39.1 (Jan. 1, 1981), pp. 201–225. ISSN: 0021-9991 (cit. on pp. 12, 13).
- [47] Jinsong Hua and Jing Lou. "Numerical simulation of bubble rising in viscous liquid". In: *Journal of Computational Physics* 222.2 (Mar. 20, 2007), pp. 769–795. ISSN: 0021-9991 (cit. on pp. 49–51).
- [48] S. Hysing et al. "Quantitative benchmark computations of two-dimensional bubble dynamics". In: *International Journal for Numerical Methods in Fluids* 60.11 (2009), pp. 1259–1288. ISSN: 1097-0363 (cit. on pp. 40, 43, 44, 121, 123).
- [49] M. R. James, Steve J. Lane, and B. A. Chouet. "Gas slug ascent through changes in conduit diameter: Laboratory insights into a volcano-seismic source process in low-viscosity magmas". In: *Journal of Geophysical Research: Solid Earth* (1978-2012) 111 (B5 2006) (cit. on pp. 26–29).
- [50] Mike R. James, Steve J. Lane, and S. B. Corder. "Modelling the rapid near-surface expansion of gas slugs in low-viscosity magmas". In: *Geological Society, London, Special Publications* 307.1 (2008), pp. 147–167 (cit. on p. 32).
- [51] M.R James et al. "Pressure changes associated with the ascent and bursting of gas slugs in liquid-filled vertical and inclined conduits". In: *The role of laboratory experiments in volcanology* 129.1 (Jan. 15, 2004), pp. 61–82. ISSN: 0377-0273 (cit. on p. 29).
- [52] Marcel Janssen et al. "Enclosed outdoor photobioreactors: Light regime, photosynthetic efficiency, scale-up, and future prospects". In: *Biotechnology and bioengineering* 81.2 (2003), pp. 193–210 (cit. on p. 28).

- [53] Chang-Wei Kang, Shaoping Quan, and Jing Lou. "Numerical study of a Taylor bubble rising in stagnant liquids". In: *Physical Review E* 81.6 (2010), p. 066308 (cit. on pp. 22, 25, 73–75, 99).
- [54] T. D. Karapantsios and A. J. Karabelas. "Longitudinal characteristics of wavy falling films". In: *International Journal of Multiphase Flow* 21.1 (1995), pp. 119–127 (cit. on p. 22).
- [55] V.V.R. Kaushik et al. "CFD simulation of core annular flow through sudden contraction and expansion". In: *Journal of Petroleum Science and Engineering* 86-87.0 (2012), pp. 153–164. ISSN: 0920-4105 (cit. on p. 27).
- [56] J Kim and P Moin. "Application of a fractional-step method to incompressible Navier-Stokes equations". In: *Journal of Computational Physics* 59.2 (1985), pp. 308–323. ISSN: 0021-9991 (cit. on p. 35).
- [57] J.P. Kockx et al. "Gas entrainment by a liquid film falling around a stationary Taylor bubble in a vertical tube". In: *International Journal of Multiphase Flow* 31.1 (Jan. 2005), pp. 1–24. ISSN: 0301-9322 (cit. on p. 31).
- [58] Koichi Kondo et al. "Flow patterns of gas-liquid two-phase flow in round tube with sudden expansion". In: *10th International Conference on Nuclear Engineering*. American Society of Mechanical Engineers, 2002, pp. 179–186 (cit. on p. 27).
- [59] V. V. Lel et al. "Local thickness and wave velocity measurement of wavy films with a chromatic confocal imaging method and a fluorescence intensity technique". In: *Experiments in fluids* 39.5 (2005), pp. 856–864 (cit. on pp. 22, 78).
- [60] Dan Liberzon, Lev Shemer, and Dvora Barnea. "Upward-propagating capillary waves on the surface of short Taylor bubbles". In: *Physics of Fluids (1994-present)* 18.4 (2006), p. 048103 (cit. on p. 32).
- [61] E. W. Llewellyn et al. "The thickness of the falling film of liquid around a Taylor bubble". In: *Proceedings of the Royal Society A: Mathematical, Physical and Engineering Science* (2011), rspa20110476 (cit. on pp. 22, 78, 87, 118).
- [62] Qi Lu, Deqi Chen, and Qinghua Wang. "Visual investigation on the interface morphology of Taylor bubble and the characteristics of two-phase flow in mini-channel". In: *Chemical Engineering Science* 134 (Sept. 29, 2015), pp. 96–107. ISSN: 0009-2509 (cit. on p. 32).
- [63] Xiaozhen Lu and Andrea Prosperetti. "A numerical study of Taylor bubbles". In: *Industrial & Engineering Chemistry Research* 48.1 (2008), pp. 242–252 (cit. on pp. 24, 25, 74).
- [64] T. K. Mandal, G. Das, and P. K. Das. "Liquid Taylor bubbles rising in a vertical column of a heavier liquid: An approximate analysis". In: *Journal of Fluids Engineering* 131.1 (2009), p. 011303 (cit. on pp. 20, 26).
- [65] Zai-Sha Mao and A. E. Dukler. "An experimental study of gas-liquid slug flow". In: *Experiments in Fluids* 8.3 (1989), pp. 169–182 (cit. on p. 31).

- [66] Zai-Sha Mao and A.E. Dukler. "The motion of Taylor bubbles in vertical tubes—II. Experimental data and simulations for laminar and turbulent flow". In: *Chemical Engineering Science* 46.8 (1991), pp. 2055–2064. ISSN: 0009-2509 (cit. on p. 25).
- [67] Zai-Sha Mao and A.E. Dukler. "The motion of Taylor bubbles in vertical tubes. I. A numerical simulation for the shape and rise velocity of Taylor bubbles in stagnant and flowing liquid". In: *Journal of Computational Physics* 91.1 (Nov. 1990), pp. 132–160. ISSN: 0021-9991 (cit. on pp. 24, 25).
- [68] G.H. Miller and P. Colella. "A Conservative Three-Dimensional Eulerian Method for Coupled Solid-Fluid Shock Capturing". In: *Journal of Computational Physics* 183.1 (Nov. 20, 2002), pp. 26–82. ISSN: 0021-9991 (cit. on p. 14).
- [69] N.V. Ndinisa, D.E. Wiley, and D.F. Fletcher. "Computational Fluid Dynamics Simulations of Taylor Bubbles in Tubular Membranes: Model Validation and Application to Laminar Flow Systems". In: *Chemical Engineering Research and Design* 83.1 (Jan. 2005), pp. 40–49. ISSN: 0263-8762 (cit. on p. 24).
- [70] D.J. Nicklin. "Two-phase bubble flow". In: *Chemical Engineering Science* 17.9 (Sept. 1, 1962), pp. 693–702. ISSN: 0009-2509 (cit. on p. 16).
- [71] S. Nogueira et al. "Flow in the nose region and annular film around a Taylor bubble rising through vertical columns of stagnant and flowing Newtonian liquids". In: *Chemical Engineering Science* 61.2 (Jan. 2006), pp. 845–857. ISSN: 0009-2509 (cit. on pp. 23, 32, 85).
- [72] S. Nogueira et al. "Flow patterns in the wake of a Taylor bubble rising through vertical columns of stagnant and flowing Newtonian liquids: An experimental study". In: *Chemical Engineering Science* 61.22 (Nov. 20, 2006), pp. 7199–7212. ISSN: 0009-2509 (cit. on pp. 32, 85).
- [73] S. Nogueira et al. "Simultaneous PIV and pulsed shadow technique in slug flow: a solution for optical problems". In: *Experiments in Fluids* 35.6 (2003), pp. 598–609 (cit. on p. 32).
- [74] William F. Noh and Paul Woodward. "SLIC (simple line interface calculation)". In: *Proceedings of the Fifth International Conference on Numerical Methods in Fluid Dynamics June 28-July 2, 1976 Twente University, Enschede*. Springer, 1976, pp. 330–340 (cit. on p. 13).
- [75] Wilhelm Nusselt. "Die Oberflächenkondensation des Wasserdampfes". In: *Zetschr. Ver. Deutch. Ing.* 60 (1916), pp. 541–546 (cit. on pp. 21, 22).
- [76] Mitsuhiro Ohta et al. "A computational study of the effect of initial bubble conditions on the motion of a gas bubble rising in viscous liquids". In: *International Journal of Multiphase Flow* 31.2 (2005), pp. 223–237. ISSN: 0301-9322 (cit. on pp. 6, 7).
- [77] Elin Olsson and Gunilla Kreiss. "A conservative level set method for two phase flow". In: *Journal of Computational Physics* 210.1 (Nov. 20, 2005), pp. 225–246. ISSN: 0021-9991 (cit. on p. 6).

- [78] Miguel Padilla, Rémi Revellin, and Jocelyn Bonjour. “Two-phase flow of HFO-1234yf, R-134a and R-410A in sudden contractions: Visualization, pressure drop measurements and new prediction method”. In: *Experimental Thermal and Fluid Science* 47.0 (2013), pp. 186–205. ISSN: 0894-1777 (cit. on p. 27).
- [79] James Edward Pilliod Jr. and Elbridge Gerry Puckett. “Second-order accurate volume-of-fluid algorithms for tracking material interfaces”. In: *Journal of Computational Physics* 199.2 (Sept. 20, 2004), pp. 465–502. ISSN: 0021-9991 (cit. on p. 14).
- [80] S. Polonsky, D. Barnea, and L. Shemer. “Averaged and time-dependent characteristics of the motion of an elongated bubble in a vertical pipe”. In: *International Journal of Multiphase Flow* 25.5 (1999), pp. 795–812. ISSN: 0301-9322 (cit. on pp. 23, 25, 31).
- [81] S Polonsky, L Shemer, and D Barnea. “The relation between the Taylor bubble motion and the velocity field ahead of it”. In: *International Journal of Multiphase Flow* 25.6 (Sept. 1999), pp. 957–975. ISSN: 0301-9322 (cit. on pp. 25, 31).
- [82] Stéphane Popinet. “An accurate adaptive solver for surface-tension-driven interfacial flows”. In: *Journal of Computational Physics* 228.16 (Sept. 1, 2009), pp. 5838–5866. ISSN: 0021-9991 (cit. on pp. 36–38).
- [83] Stéphane Popinet. “Gerris: a tree-based adaptive solver for the incompressible Euler equations in complex geometries”. In: *Journal of Computational Physics* 190.2 (2003), pp. 572–600 (cit. on pp. 35, 36).
- [84] Swapna S. Rabha and Vivek V. Buwa. “Volume-of-fluid (VOF) simulations of rise of single/multiple bubbles in sheared liquids”. In: *20th International Symposium in Chemical Reaction Engineering-Green Chemical Reaction Engineering for a Sustainable Future* 65.1 (Jan. 1, 2010), pp. 527–537. ISSN: 0009-2509 (cit. on p. 8).
- [85] Alexander S Rattner and Srinivas Garimella. “Vertical upward intermediate scale Taylor flow: Experiments and kinematic closure”. In: *International Journal of Multiphase Flow* 75 (2015), pp. 107–123 (cit. on p. 16).
- [86] A. Rinne and R. Loth. “Development of local two-phase flow parameters for vertical bubbly flow in a pipe with sudden expansion”. In: *Experimental Thermal and Fluid Science* 13.2 (1996), pp. 152–166. ISSN: 0894-1777 (cit. on p. 27).
- [87] Véronique Roig et al. “Dynamics of a high-Reynolds-number bubble rising within a thin gap”. In: *Journal of Fluid Mechanics* 707 (2012), pp. 444–466 (cit. on p. 15).
- [88] K. Sankaranarayanan et al. “Bubble flow simulations with the lattice Boltzmann method”. In: *Chemical Engineering Science* 54.21 (Nov. 1999), pp. 4817–4823. ISSN: 0009-2509 (cit. on p. 6).
- [89] L.M.T. Santos and M.N. Coelho Pinheiro. “Flow around individual Taylor bubbles rising in a vertical column with water: Effect of gas expansion”. In: *International Journal of Multiphase Flow* 63.0 (2014), pp. 39–51. ISSN: 0301-9322 (cit. on p. 26).

- [90] Alex Scammell and Jungho Kim. "Heat transfer and flow characteristics of rising Taylor bubbles". In: *International Journal of Heat and Mass Transfer* 89 (2015), pp. 379–389 (cit. on p. 32).
- [91] Ruben Scardovelli and Stephane Zaleski. "Analytical Relations Connecting Linear Interfaces and Volume Fractions in Rectangular Grids". In: *Journal of Computational Physics* 164.1 (Oct. 10, 2000), pp. 228–237. ISSN: 0021-9991 (cit. on p. 13).
- [92] Ruben Scardovelli and Stephane Zaleski. "Interface reconstruction with least-square fit and split Eulerian-Lagrangian advection". In: *International Journal for Numerical Methods in Fluids* 41.3 (2003), pp. 251–274. ISSN: 1097-0363 (cit. on p. 14).
- [93] R Schreiber and HB Keller. "Driven cavity flows by efficient numerical techniques". In: *Journal of Computational Physics* 49.2 (1983), pp. 310–333. ISSN: 0021-9991 (cit. on p. 39).
- [94] John Bartlett Segur and Helen E Oberstar. "Viscosity of glycerol and its aqueous solutions". In: *Ind. Eng. Chem* 43.9 (1951), pp. 2117–2120 (cit. on p. 65).
- [95] Ralf Seyfried and Armin Freundt. "Experiments on conduit flow and eruption behavior of basaltic volcanic eruptions". In: *Journal of Geophysical Research: Solid Earth (1978-2012)* 105 (B10 2000), pp. 23727–23740 (cit. on p. 31).
- [96] RN Singh and Shaishav Sharma. "Development of suitable photobioreactor for algae production-A review". In: *Renewable and Sustainable Energy Reviews* 16.4 (2012), pp. 2347–2353 (cit. on pp. 28, 29).
- [97] Gihun Son. "A numerical method for incompressible two-phase flows with open or periodic boundaries". In: *Numerical Heat Transfer: Part B: Fundamentals* 39.1 (2001), pp. 45–60 (cit. on p. 25).
- [98] R.G. Sousa et al. "Flow around individual Taylor bubbles rising in stagnant CMC solutions: PIV measurements". In: *Chemical Engineering Science* 60.7 (2005), pp. 1859–1873. ISSN: 0009-2509 (cit. on p. 32).
- [99] R.G. Sousa et al. "Flow around individual Taylor bubbles rising in stagnant polyacrylamide (PAA) solutions". In: *Journal of Non-Newtonian Fluid Mechanics* 135.1 (Apr. 3, 2006), pp. 16–31. ISSN: 0377-0257 (cit. on p. 32).
- [100] Mark Sussman. "A second order coupled level set and volume-of-fluid method for computing growth and collapse of vapor bubbles". In: *Journal of Computational Physics* 187.1 (2003), pp. 110–136. ISSN: 0021-9991 (cit. on p. 6).
- [101] Mark Sussman and Mitsuhiro Ohta. "Improvements for calculating two-phase bubble and drop motion using an adaptive sharp interface method". In: (2007) (cit. on p. 38).
- [102] Mark Sussman, Peter Smereka, and Stanley Osher. "A Level Set Approach for Computing Solutions to Incompressible Two-Phase Flow". In: *Journal of Computational Physics* 114.1 (Sept. 1994), pp. 146–159. ISSN: 0021-9991 (cit. on pp. 10, 11).

- [103] Mark Sussman et al. "An improved level set method for incompressible two-phase flows". In: *Computers & Fluids* 27.5 (1998), pp. 663–680. ISSN: 0045-7930 (cit. on pp. 9, 10).
- [104] T. Taha and Z.F. Cui. "Hydrodynamic analysis of upward slug flow in tubular membranes". In: *Desalination* 145.1 (Sept. 10, 2002), pp. 179–182. ISSN: 0011-9164 (cit. on p. 24).
- [105] Taha Taha and Z.F. Cui. "CFD modelling of slug flow in vertical tubes". In: *Chemical Engineering Science* 61.2 (Jan. 2006), pp. 676–687. ISSN: 0009-2509 (cit. on pp. 24, 25).
- [106] Taha Taha and Z.F. Cui. "CFD modelling of slug flow inside square capillaries". In: *Chemical Engineering Science* 61.2 (Jan. 2006), pp. 665–675. ISSN: 0009-2509 (cit. on p. 15).
- [107] Akio Tomiyama et al. "Numerical analysis of bubble motion with the VOF method". In: *Nuclear Engineering and Design* 141.1 (1993), pp. 69–82. ISSN: 0029-5493 (cit. on pp. 6, 24, 25).
- [108] Akio Tomiyama et al. "Transverse migration of single bubbles in simple shear flows". In: *Chemical Engineering Science* 57.11 (2002), pp. 1849–1858. ISSN: 0009-2509 (cit. on p. 8).
- [109] Grétar Tryggvason et al. "A front-tracking method for the computations of multiphase flow". In: *Journal of Computational Physics* 169.2 (2001), pp. 708–759 (cit. on p. 12).
- [110] LN Tsoglin et al. "Closed photobioreactors for microalgal cultivation". In: *Russian Journal of Plant Physiology* 43.1 (1996), pp. 131–136 (cit. on p. 28).
- [111] Kie Wei Tung and Jean-Yves Parlange. "Note on the motion of long bubbles in closed tubes-influence of surface tension". In: *Acta Mechanica* 24.3 (1976), pp. 313–317 (cit. on p. 19).
- [112] Y. Ueda et al. "Numerical Simulation of Gas-Liquid Two-Phase Flow in a Horizontally Placed Hydrophobic Rectangular Channel (Part 1, Influence of Abrupt Expansion)". In: (2012) (cit. on p. 27).
- [113] Salih Ozen Unverdi and Grétar Tryggvason. "A front-tracking method for viscous, incompressible, multi-fluid flows". In: *Journal of Computational Physics* 100.1 (1992), pp. 25–37. ISSN: 0021-9991 (cit. on p. 11).
- [114] R Van Hout et al. "Experimental investigation of the velocity field induced by a Taylor bubble rising in stagnant water". In: *International Journal of Multiphase Flow* 28.4 (2002), pp. 579–596 (cit. on pp. 23, 26, 32).
- [115] Flavia Viana et al. "Universal correlation for the rise velocity of long gas bubbles in round pipes". In: *Journal of Fluid Mechanics* 494 (2003), pp. 379–398 (cit. on pp. 19, 77, 83, 87, 94, 95, 110).
- [116] G. B. Wallis. *One-dimensional two-phase flow*. McGraw-Hill, 1969 (cit. on pp. 17, 19, 21, 77, 83, 95).
- [117] Han Wang et al. "Viscosity effects on the behavior of a rising bubble". In: *Journal of Hydrodynamics, Ser. B* 22.1 (2010), pp. 81–89. ISSN: 1001-6058 (cit. on p. 7).

- [118] E.T. White and R.H. Beardmore. "The velocity of rise of single cylindrical air bubbles through liquids contained in vertical tubes". In: *Chemical Engineering Science* 17.5 (1962), pp. 351–361. ISSN: 0009-2509 (cit. on pp. [17](#), [18](#), [21](#), [25](#), [31](#), [71](#), [77](#), [83](#), [95](#), [117](#)).
- [119] Jong Hyun Yoon, Shin Sik Choi, and Tai Hyun Park. "The cultivation of *Anabaena variabilis* in a bubble column operating under bubbly and slug flows". In: *Bioresource technology* 110 (2012), pp. 430–436 (cit. on p. [28](#)).
- [120] David L. Youngs. "Time-dependent multi-material flow with large fluid distortion". In: *Numerical methods for fluid dynamics* 24.2 (1982), pp. 273–285 (cit. on p. [13](#)).
- [121] G. Zabarar, A. E. Dukler, and D. Moalem-Maron. "Vertical upward cocurrent gas-liquid annular flow". In: *AIChE journal* 32.5 (1986), pp. 829–843 (cit. on p. [31](#)).
- [122] Donghong Zheng, Xiao He, and Defu Che. "CFD simulations of hydrodynamic characteristics in a gas-liquid vertical upward slug flow". In: *International Journal of Heat and Mass Transfer* 50.21 (Oct. 2007), pp. 4151–4165. ISSN: 0017-9310 (cit. on p. [25](#)).
- [123] E. E. Zukoski. "Influence of viscosity, surface tension, and inclination angle on motion of long bubbles in closed tubes". In: *Journal of Fluid Mechanics* 25.4 (1966), pp. 821–837 (cit. on p. [17](#)).
- [124] Iztok Zun et al. "Mixing of thermally stratified water layer by a free rising wobbling air bubble". In: *Chemical Engineering Science* 72.0 (2012), pp. 155–171. ISSN: 0009-2509 (cit. on p. [8](#)).



FOLIO ADMINISTRATIF

THESE DE L'UNIVERSITE DE LYON OPEREE AU SEIN DE L'INSA LYON

NOM : ZHOU

DATE de SOUTENANCE : 12/07/2017

Prénom : Chengsi

TITRE : Numerical simulation and experimental investigations of two-phase flow in singularities

NATURE : Doctorat

Numéro d'ordre : 2017LYSEI065

Ecole doctorale : Mécanique, Energétique, Génie Civil, Acoustique

Spécialité : Thermique et Energétique

RESUME : Numerical simulations and experimental investigations of a rising individual Taylor bubble through a vertical sudden expansion and contraction in stagnant Newtonian liquid are presented. The CFD procedure is based on the open source package Gerris which adopts the volume-of-fluid (VOF) method to represent the gas/liquid interface. The numerical method is verified using the existing results of single Taylor bubbles rising in straight columns. The experiments investigate a nitrogen bubble rising in a water-glycerol mixture for different concentrations. The pipe diameter ratio ranges from 0.69 to 1.72. The images of the bubble rising through the singularities are captured by a high-speed camera. Our investigations focus on the transient process of the bubbles passing the singularity. The variations of the bubble velocity and the liquid film thickness are investigated. The results show that the greater expansion ratios yield more perturbations on the bubbles and have strong effects on the tail of the bubble. The unstable bubble tails are cut off into smaller bubbles in some of the test cases and a bubble break-up regime map obtained by simulations has been proposed. The bubble shape variations depend also on the length of the bubbles. For a bubble passing through a contraction, the blocking phenomenon has been observed and a map has been proposed. Finally, this study, based on a large range of Eötvös numbers and expansion/contraction ratios, provides new insights to better understand the effect of singularities on rising Taylor bubbles.

MOTS-CLÉS :

Two-phase flow, Taylor bubble, contraction, expansion, VOF, experiment

Laboratoire (s) de recherche : CETHIL

Directeur de thèse: Rémi REVELLIN

Président de jury :

JOSSERAND, Christophe Directeur de Recherche Ecole Polytechnique Président

Composition du jury :

MAURO, William Associate	Professor	University of Naples Federico II	Rapporteur
ROIG, Véronique	Professeur des Universités	IMFT	Rapporteur
NASO, Aurore	Chargé de Recherche	École Centrale de Lyon	Examineur
REVELLIN, Rémi	Professeur des Universités	INSA-LYON	Directeur de thèse
KNIKKER, Ronnie	Maître de conférences	INSA-LYON	Co Directeur de thèse